PREPARATION AND CHARACTERIZATION OF POLYMER/PARTICLE ELECTROSPUN FIBER ELECTRODES FOR HYDROGEN/AIR FUEL CELLS

By

Krysta Waldrop

Dissertation

Submitted to the Faculty of the

Graduate School of Vanderbilt University

in partial fulfillment of the requirements

for the degree of

DOCTOR OF PHILOSOPHY

in

Chemical Engineering

August 31, 2021

Nashville Tennessee

Approved:

Peter Pintauro, Ph.D.

Kelsey Hatzell, Ph.D.

Piran Kidambi, Ph.D.

Paul Laibinis, Ph.D.

A. DEDICATION

Dedicated to my family and friends for supporting me during this endeavor.

B. ACKNOWLEDGEMENTS

I thank all my friends, family, and mentors who have provided me with support and guidance during my time at Vanderbilt University. I greatly appreciate the valuable feedback and support provided by my thesis advisor, Professor Peter Pintauro, as well as my thesis committee members, Professors Kelsey Hatzell, Paul Laibinis, and Piran Kidambi.

I am very grateful for the support provided by my fellow lab mates. Dr. Matthew Brodt provided my initial lab training and was both kind and patient while I learned how to thrive in the new laboratory environment. Professor Ryszard Wycisk is deserving of much gratitude as his knowledge in polymers was invaluable, and he was able to bring a sense of levity to the lab during times of high stress. I would also like to thank the post docs with whom I overlapped: Drs. Leslie Dos Santos, Narae Kang, and Abhishek Mondal, for both their friendship and guidance. Dr. Devon Powers was an exceptional friend, and the fervor with which he approached his work was unmatched and inspiring. Dr. John Slack was also a dear friend whose ingenuity never failed to impress me. I would also like to thank John Waugh and Autumn Taylor for their friendship and for serving as a sounding board. I know they will both accomplish great things during their graduate studies and beyond.

I would also like to thank the employees of the Vanderbilt Institute of Nanoscale Science and Engineering, namely Drs. Anthony Hmelo and James McBride for training and assisting me on the scanning and transmission electron microscopes. Other members of the Vanderbilt community I wish to thank include Felisha Baquera, Angie Pernell, and the late Mary Gilleran for their help in all things administrative and for their friendship. I thank the many friends I

made at the university, such as Amy Zhang and Mathew Miletich for being great friends and providing me with many delicious dinners. Lastly, I want to thank my husband, Dr. Michael Crocker, who shared in the adventure of graduate school with me, and who gruelingly read through all of my documents.

Beyond the scope of the university, I wish to express my gratitude to the many accomplished collaborators with whom I had the opportunity to work. Drs. Nilesh Dale, Cenk Gumeci, and Amod Kumar at the Nissan Technical Center of North America provided valuable feedback on our projects as well as expanded our testing capabilities through the use of their facilities. Dr. Karren More, Dr. David Cullen, and Sean Reeves from Oak Ridge National Laboratory kindly offered their time and expertise to train me on new equipment, provided feedback on results, and aided in the preparation of materials. Drs. Rangachary Mukundan and Rodney Borup of Los Alamos National Lab utilized the equipment at their disposal to help our laboratory better understand the results we observed.

This work was funded by the National Science Foundation ("SusChem: Sustainable Chemicals Production Using Solid Polymer Electrolyte Reactors," award number 1437384) and by the United States Department of Energy Fuel Cell Consortium for Performance and Durability (DOE-EERE FC-PAD Project DE-EE0007653).

C. TABLE OF CONTENTS

Chapter Page

D. LIST OF TABLES

E. LIST OF FIGURES

CHAPTER 1 INTRODUCTION

The growing need for sustainable and clean energy solutions has brought hydrogen/air fuel cells to the forefront of research and development. Moderate operating temperatures (50-100 °C), high efficiency (up to 83%), and the promise of zero-emission operation make this type of proton exchange membrane fuel cell (PEMFC) an attractive candidate for stationary and automotive applications.[1] Unlike the internal combustion engine (ICE) used in most motor vehicles, PEMFC engines are solid state, simplifying engine design, and produce only water and electricity, eliminating the emissions of harmful NO_x and CO_x gases produced by an ICE. Although Li-ion battery electric vehicles have gained a respectable share of the automotive market, there remain limitations in terms of charge time and distance per charge. To increase distance per charge in a battery electric vehicle, a larger battery is needed, or new electrode chemistries must be found that produce a high volumetric energy density. Such issues do not arise in a fuel cell electric vehicle (FCEV) where re-fuel time is about 5 minutes and distance per fueling is dictated by fuel tank size.

While several automotive companies have released FCEVs, including Toyota, Hyundai, and Honda, several obstacles stand in the way of large-scale use of these vehicles. These include (i) the high cost of the platinum catalyst, (ii) the durability of the fuel cell's membrane-electrode-assembly (MEA), and (iii) power output while operating at variable relative humidity (RH) conditions. The work of this dissertation seeks to overcome these obstacles using electrospun fiber electrode architectures using different catalyst and binder types.

1.1 Cost and loading of platinum catalyst

Hydrogen/air fuel cell operation is dictated by two reactions, the hydrogen oxidation reaction (HOR) at the anode and the oxygen reduction reaction (ORR) at the cathode. Traditionally, these reactions have been catalyzed using platinum on a carbon support. Ideally a FCEV would have the same mass of platinum as what is currently used in catalytic converters for the ICE (~ 3-7 g), but as it stands, the Toyota Mirai uses

26 g Pt.[2] The high platinum content is needed to facilitate the ORR where the kinetics are sluggish relative to the HOR. To realize wide-spread use of fuel cell passenger vehicles, platinum content must be further reduced, and alternative cathode catalysts have been investigated including Pt-alloys[3–5] and shape-controlled catalyst.[6–10]

Platinum binds strongly with O and OH groups, and the slow desorption of these groups hinders the ORR.[11] Through alloying platinum with a transition metal or controlling the surface facets (i.e. the exposed crystallographic planes), this bond weakens allowing for improved catalytic activity.[12–14] For example, Mukerjee et al. showed oxygen reduction mass activity doubled from 0.074 A/mg_{PGM} using Pt/C to ~0.155 A/mg_{PGM} using PtNi/C or PtCo/C and power at 0.6 V increased by 20%.[3] Controlling catalyst shape resulted in further improvement in catalytic activity. Stamenkovic showed that Pt_3Ni (111) (octahedral) was much more active than Pt_3Ni (100) (cubic) or Pt_3Ni (110) (tetragonal).[6] Choi et al. developed octahedral $Pt_{2.5}Ni$ (111) and found that the ORR mass activity was 8 and 16 times greater than the activity of polycrystalline PtNi and Pt catalyst, respectively.[9] However, mass activity of shape controlled catalysts was determined using a rotating disk electrode (RDE) which often results in much higher activities than what is observed for an MEA.[15] Nevertheless, the use of shape-controlled catalyst can significantly improve MEA performance, as seen by Xia who reported a 20% increase in maximum power when going from a polycrystalline PtCo to a truncated octahedron PtCo.[10]

1.2 Durability of MEA catalyst layer

During vehicle operation, the MEA catalyst layer may experience rapid voltage changes, voltage spikes, and starvation of feed gases, all of which cause irreversible damage to the device. System mitigation strategies have been proven to alleviate some of these sources of degradation but incur additional costs to the system design and limit the range of operating voltage. Consequently, researchers are seeking to improve durability by modifying the MEA catalyst layer. Alloyed[16,17] and shape-controlled catalysts,[10] non-

carbon[18–20] or graphitic carbon supports,[21,22] and the inclusion of hydrophobic additives[23–25] have all been studied as a means of minimizing the deleterious effects of corrosion. The work in this dissertation will focus on two major degradation mechanisms, being metal dissolution and corrosion of the catalyst support.

1.2.1 Metal Dissolution

Rapid changes in operating voltage, associated with going from idling to accelerating in a FCEV, lead to severe loss of active metal sites for electrochemical reaction. Loss of platinum catalyst can occur through three different mechanisms. These are 1) dissolution of the metal followed by precipitation in the ionomer or removal through the effluent, 2) dissolution of the metal followed by redeposition on larger metal sites (Ostwald ripening),[26,27] and 3) coalescence of metal particles through particle migration on the support surface.[28,29]

The U.S. DOE has provided an accelerated-stress-test (AST) to mimic electrocatalyst degradation. This is square-wave voltage cycling from 0.6 V to 0.95 V for 3 s at each voltage under fully humidified hydrogen/nitrogen at ambient pressure and 80 °C. Based on the DOE 2020 targets, after 30,000 square-wave cycles, mass activity and ECSA should decrease by no more than 40% while the voltage loss at 0.8 A/cm^2 should be less than 30 mV.[30]

Alloying has proven a promising approach towards improved electrocatalyst durability. Popov and coworkers reported that metal particle growth after a durability test was negligible when using a PtNi/C catalyst, whereas the average diameter of particles increased by 30% using Pt/C.[17] The authors attributed this to an anchor effect, where the presence of Ni strengthens the Pt-C bond which hinders sintering of platinum atoms. Similar results were reported by Plasse and coworkers who found a PtCo/C catalyst to retain more power than a commercial Pt/C catalyst after AST.[16] Additionally, images of the MEA cross-

sections revealed that a thick band of platinum deposited in the membrane of the Pt/C MEA after cycling. No such band was observed in the PtCo/C MEA. However, due to leaching of the transition metals an appreciable loss was observed in mass activity for these alloyed catalysts.

1.2.3 Catalyst Support Corrosion

Amorphous carbon is the most commonly used support for metal catalyst particles due to high surface area and electrical conductivity. Although carbon is susceptible to oxidation at voltages as low as 0.207 V, appreciable degradation occurs at voltages above the typical operating range (>1.2 V).[31] However, voltage spikes up to 1.5 V can occur during vehicle start-up/shut-down resulting in severe oxidation of catalyst support.[32] Loss of support causes thinning of the catalyst layer which leads to mass transport limitation and loss of catalyst.[33]

The standard AST protocol laid out by the DOE to replicate catalyst support corrosion is a triangular wave from 1.0 to 1.5 V at a sweep rate of 500 mV/s under fully humidified hydrogen/nitrogen at ambient pressure and 80 °C. The 2020 targets are less than a 40% loss in both mass activity and ECSA and less than 30 mV lost at 1.5 A/cm^2 after 5,000 cycles.[30]

A common approach to minimizing the loss of catalyst support is the use of non-carbon support.[18–20] Although research in the field has shown non-carbon supports to be resistant to oxidation and highly durable, the low surface area and poor electrical conductivity result in MEAs which produce low power both initially and after durability testing. Rather than modifying catalyst, other research has shown changing the electrode binder composition may minimize the effects of carbon oxidation. Including a hydrophobic material, such as poly(vinylidene fluoride)[24,25] or polydimethylsiloxane,[23] aids in water removal and, consequently, suppresses oxidation of carbon supports.

1.3 Power output at variable humidity

A fuel cell engine which generates high power at both high and low humidification is highly desirable as it would eliminate the need for onboard humidifiers and simplify vehicle design. At saturated or high humidity operation, fuel cell performance can be hindered by flooding. Under flooding conditions water is not removed quickly enough from the system, preventing oxygen from accessing catalyst sites. Conversely, at low humidity fuel cell performance may suffer due to drying of the membrane and catalyst layer ionomer which hinders the transport of protons from the anode to the cathode. Flow field design, diffusion media,[34] membrane,[35] and catalyst layer composition[36–40] have all been investigated with the goal of mitigating both flooding and drying. A common approach to improve performance during low humidity operation is the use of low equivalent weight ionomers in the membrane and/or the catalyst layers; the increased number of sulfonic acid sites prevents drying.[37,38] Similarly, another tactic is to increase the amount of ionomer relative to catalyst in the electrodes.[36,39] While both of these methods indeed improved power at low humidity, the increased hydrophilicity results in flooding at higher humidity.

The next chapter will discuss MEA analysis, the background of electrospinning in fuel cell applications, and the objectives of this dissertation.

1.4 References

1. F. Barbir, *PEM Fuel Cells - Theory and Practice*, 2nd ed., p. 130–132, Elsevier, Boston, (2012).
2. R. Borup, in *Presentation to USCAR*, (2019).
3. S. Mukerjee and S. Srinivasan, *J. Electroanal. Chem.*, **357**, 201–224 (1993).
4. T. Toda, *J. Electrochem. Soc.*, **146**, 3750 (1999).
5. C. Wang, N. M. Markovic, and V. R. Stamenkovic, *ACS Catal.*, **2**, 891–898 (2012).
6. V. R. Stamenkovic et al., *Science (80-.).*, **315**, 493–497 (2007).
7. Y. X. Sang-Il Choi, Shuifen Xie, Minhua Shao, Jonathan H. Odell, Ning Lu, Hsin-Chieh Peng, Lesia

Protsailo, Sandra Guerrero, Jinho Park, Xiaohu Xia, Jinguo Wang, Moon J. Kim, *Nano Lett.*, **13**, 3420–3425 (2013).

8. C. Cui et al., *Nano Lett.*, **12**, 5885–5889 (2012).

9. S. Il Choi et al., *ChemSusChem*, **7**, 1476–1483 (2014).

10. M. Shen et al., *Nanoscale*, **12**, 11718–11727 (2020).

11. O. T. Holton and J. W. Stevenson, *J. Electrochem. Soc.*, **57**, 864–890 (2013).

12. V. Jalan and E. J. Taylor, *Electrochem. Soc. Ext. Abstr.*, **83**–**1**, 1072–1073 (1983).

13. S. Mukerjee, S. Srinivasan, M. P. Soriaga, and J. McBreen, *J. Electrochem. Soc.*, **142**, 1409 (1995).

14. N. M. Markovic, H. A. Gasteiger, and P. N. Ross, *J. Phys. Chem.*, **99**, 3411–3415 (1995).

15. S. A. Mauger et al., *J. Electrochem. Soc.*, **165**, F238–F245 (2018).

16. P. Yu, M. Pemberton, and P. Plasse, *J. Power Sources*, **144**, 11–20 (2005).

17. H. R. Colón-Mercado, H. Kim, and B. N. Popov, *Electrochem. commun.*, **6**, 795–799 (2004).

18. A. Kumar and V. Ramani, *ACS Catal.*, **4**, 1516–1525 (2014).

19. Y. Liu and W. E. Mustain, *J. Am. Chem. Soc.*, **135**, 530–533 (2013).

20. B. Seger, A. Kongkanand, K. Vinodgopal, and P. V. Kamat, *J. Electroanal. Chem.*, **621**, 198–204 (2008).

21. P. V. Shanahan et al., *J. Power Sources*, **185**, 423–427 (2008).

22. X. Wang, W. Li, Z. Chen, M. Waje, and Y. Yan, *J. Power Sources*, **158**, 154–159 (2006).

23. M. Choun, D. Nauryzbayev, D. Shin, and J. Lee, *Catal. Today*, **262**, 155–160 (2016).

24. J. J. Slack et al., *J. Electrochem. Soc.*, **167**, 054517 (2020).

25. M. Brodt, R. Wycisk, N. Dale, and P. Pintauro, *J. Electrochem. Soc.*, **163**, F401–F410 (2016).

26. K. Kinoshita, J. T. Lundquist, and P. Stonehart, *Electroanal. Chem. InterJacial Electrochem.*, **48**, 157–166 (1973).

27. Y. Sugawara, T. Okayasu, A. P. Yadav, A. Nishikata, and T. Tsuru, *J. Electrochem. Soc.*, **159**, F779–F786 (2012).

28. K. F. Blurton, H. R. Kunzt, and D. R. Rutt, *Electrochim. Acta*, **23**, 183–190 (1978).

29. M. S. Wilson, F. H. Garzon, K. E. Sickafus, and S. Gottesfeld, *J. Electrochem. Soc.*, **140**, 2872–2877 (1993).

30. *Off. Energy Effic. Renew. Energy* https://www.energy.gov/eere/fuelcells/doe-technical-targets-polymer-electrolyte-membrane-fuel-cell-components.

31. M. F. Mathias et al., *Electrochem. Soc. Interface*, **14**, 24–35 (2005).

32. C. A. Reiser et al., *Electrochem. Solid-State Lett.*, **8**, 273–276 (2005).

33. N. Macauley et al., *J. Electrochem. Soc.*, **165**, F3148–F3160 (2018).

34. T. Kitahara, H. Nakajima, M. Inamoto, and M. Morishita, *J. Power Sources*, **234**, 129–138 (2013).

35. B. Kienitz, J. Kolde, S. Priester, C. Baczkowski, and M. Crum, *ECS Trans.*, **41**, 1521–1530 (2011).

36. S. Jeon et al., *Int. J. Hydrogen Energy*, **35**, 9678–9686 (2010).

37. Y.-C. Park, K. Kakinuma, H. Uchida, and M. Watanabe, *J. Power Sources*, **275**, 384–391 (2015).

38. C. Lei et al., *J. Power Sources*, **196**, 6168–6176 (2011).

39. K. Shinozaki, H. Yamada, and Y. Morimoto, *J. Electrochem. Soc.*, **158**, B467–B475 (2011).

40. N. Inoue, M. Uchida, M. Watanabe, and H. Uchida, *Electrochem. commun.*, **16**, 100–102 (2012).

CHAPTER 2BACKGROUND

2.1 Fuel Cell Components

The PEMFC is comprised of several components, 1: flow fields to deliver feed gases, 2: gas diffusion layers (GDLs) to transport gases from the flow field to the electrodes, 3: electrodes where the electrochemical reactions occur, and 4: the proton exchange membrane which transports protons from the anode to the cathode. These components are illustrated in Figure 2.1.

The work of this thesis focuses on the membrane-electrode-assembly (MEA). The major components of the MEA are the electrocatalyst, ion conducting polymer (ionomer), and the proton exchange membrane. Most commonly, the electrocatalyst is a Pt-based metal supported on an electrically conductive carbon support. The catalyst layer is held together by the addition of a polymeric binder, typically an ionomer. Perfluorosulfonic acids (PFSAs) are by far the most prevalent proton conducting ionomers used in PEMFCs,[1] although sulfonated fluorocarbons and hydrocarbons have also been studied.[2–5] The structure of Nafion®, a commercial PFSA, is presented in Figure 2.2. The fluorinated backbone of PFSA provides excellent chemical and mechanical stability while the acidic side chain allows for proton conduction. PFSA films also serve as the proton exchange membrane.

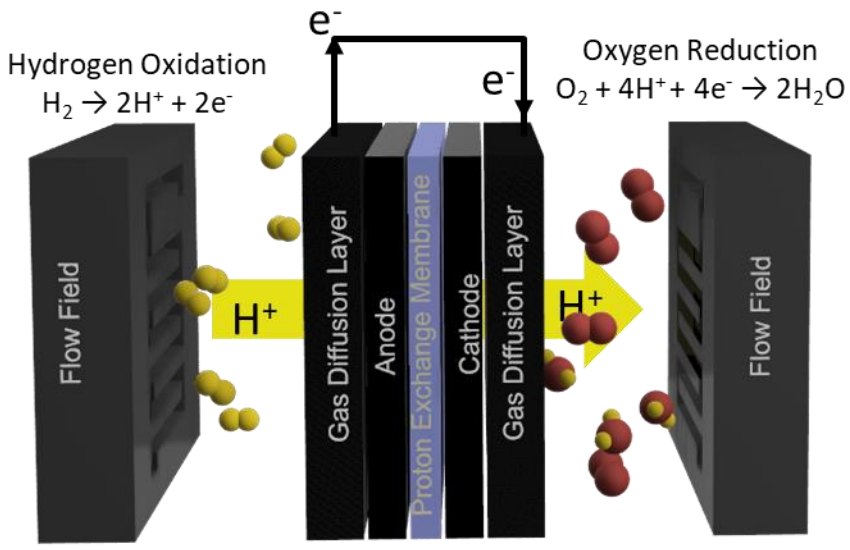

Figure 2.1: Schematic of PEMFC operation

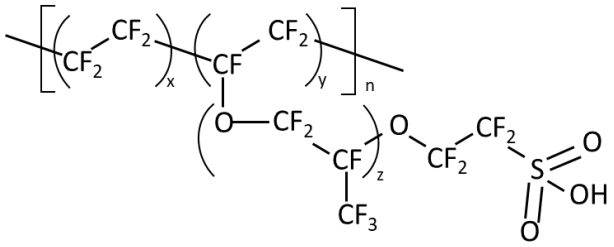

Figure 2.2: Chemical structure of PFSA Nafion®

2.2 PEMFC Operation and Theory

The proton exchange membrane fuel cell is governed by two half reactions, the hydrogen oxidation reaction (HOR) which occurs at the anode (Eq. 2.1) and the oxygen reduction reaction (ORR) which occurs at the cathode (Eq. 2.2). Molecular hydrogen splits into protons and electrons. The electrons go through an external circuit, where they can be utilized to power a device, and then reach the cathode. Protons are transported through the ionically conductive

polymer membrane to the cathode where they combine with oxygen and electrons to form water. This process is illustrated in Figure 2.1.

$$H_2 \rightarrow 2H^+ + 2e^- \qquad \text{Reaction 2.1}$$

$$\frac{1}{2}O_2 + 2H^+ + 2e^- \rightarrow H_2O \qquad \text{Reaction 2.2}$$

The overall reaction is spontaneous, meaning the process releases energy. The available electrical energy (or the Gibbs free energy) can be calculated from the enthalpy and entropy of the reaction. A theoretical cell potential of hydrogen and oxygen can be obtained using the Gibbs free energy and Equation 2.1, where: E is the theoretical cell potential (V), ΔG is the Gibbs free energy (J/mol), n is the number of electrons (2), and F is Faraday's constant (96485 C/mol). Solving this equation gives E= 1.23 V, but this only applies at 25 °C. As operating temperature increases, cell potential decreases. Cell potential also drops due to fuel crossover and mixed potentials. A finite amount of molecular hydrogen can permeate through the proton exchange membrane to react with oxygen which reduces cell potential. Similarly, any side reactions, for example the 4-electron process of $H_2 + O \rightarrow H_2O_2$, will result in a lower cell potential.[6]

$$E = \frac{-\Delta G}{nF} \qquad \text{Equation 2.1}$$

The cell potential at zero current is referred to as the open circuit voltage (OCV), and the factors affecting the OCV were discussed above. As current is drawn, cell potential will decrease due to overpotential losses. These losses are due to: 1) kinetics/activation, 2) ohmic resistance, and 3) mass transport. Activation losses refer to the reaction kinetics and dominate in the low current density regime. Although activation losses occur at both the anode and cathode, the ORR

is considered to be much slower than the HOR, meaning activation losses at the anode are negligible. Activation overpotential for the ORR reaction can be described by the cathodic portion of the Butler-Volmer equation (Eq. 2.2) where, R is the universal gas constant, T is temperature, α is the oxidant transfer coefficient, i is current density, and i_0 is exchange current density.

$$\eta_{activation} = \frac{RT}{\alpha F} ln \left(\frac{i}{i_0}\right) \quad \text{Equation 2.2}$$

Ohmic overpotentials are due to electronic and protonic resistances in the cell and are governed by Ohms Law (Eq. 2.3) where i is current density and R_i is the total cell internal resistance.

$$\eta_{Ohmic} = iR_i \quad \text{Equation 2.3}$$

Transport overpotentials (or concentration polarization) arise at high current densities, where oxygen consumption is limited by its rate of diffusion to catalyst sites. This phenomenon is described by equation Eq. 2.4 where i_L is the mass transfer limiting current density.

$$\eta_{Transport} = \frac{RT}{nF} ln \left(\frac{i_L}{i_L - i}\right) \quad \text{Equation 2.4}$$

Voltage losses and cell voltage as a function of current are plotted in Figures 2.3a and 2.3b, respectively. Figure 2.3b is referred to as a polarization curve and is an important tool for evaluating the performance of a fuel cell.

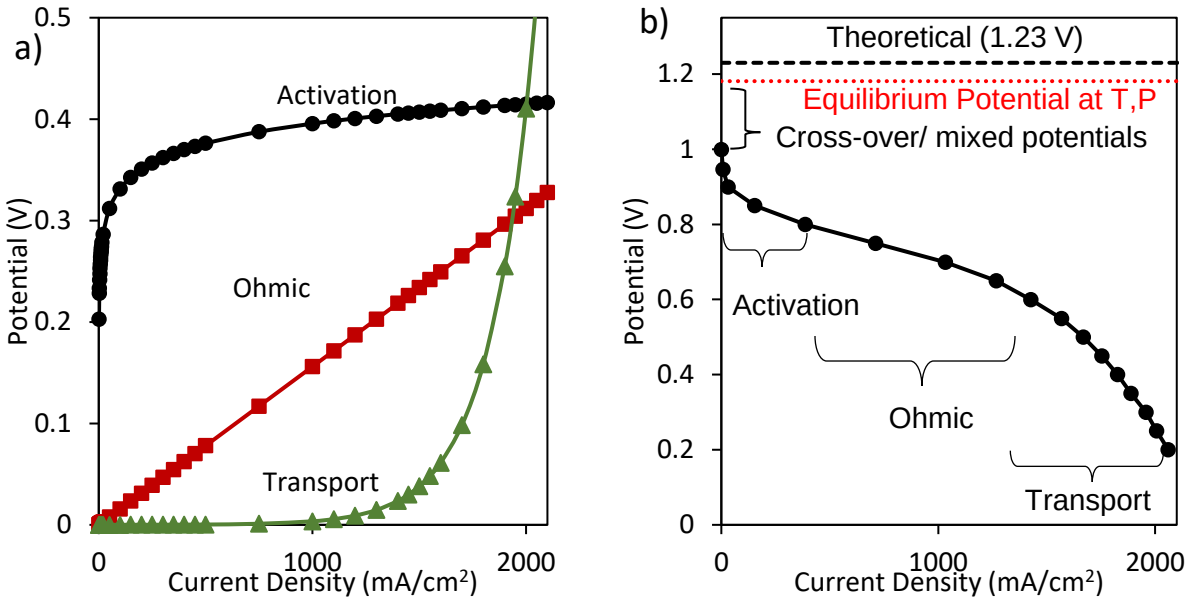

Figure 2.3: a) Overpotentials in a fuel cell and b) a typical fuel cell polarization curve

2.3 PEMFC Analysis

Polarization curve analysis is just one of many electrochemical techniques used to study fuel cells. This dissertation will also discuss the use of cyclic voltammetry (CV) to determine electrochemically active surface area (ECSA), electrochemical impedance spectroscopy (EIS), linear sweep voltammetry (LSV), gas transport resistance (GTR), mass activity, and accelerated stress tests (ASTs) to evaluate fuel cells.

2.3.1 Electrochemically Active Surface Area

Not all catalyst in an electrode is available for electrochemical reaction. Catalytic material may be inaccessible to oxygen, protons, and/or electrons. Electrochemically active surface area (ECSA) is a measurement of the catalyst surface available for electrochemical reaction normalized for catalyst loading. Using a potentiostat to drive the reaction, voltage is swept in the forward direction to oxidize any adsorbed hydrogen (H_{ads}) to H^+, and then voltage is swept in the reverse

direction to reduce the protons back to H_{ads} on the catalyst surface. A typical CV is plotted in Figure 2.4, where the shaded region corresponds to the charge density exchanged during hydrogen electroadsorption. Plugging the charge into Equation 2.5 gives the ECSA in m^2/g_{Pt}, where q_{Pt} is the charge density (C/cm^2), Γ is the charge required to reduce a monolayer of protons onto Pt (210 $\mu C/cm^2_{Pt}$) and L is the platinum loading (mg_{Pt}/cm^2_{geo}).[7]

$$ECSA = \frac{q_{Pt}}{\Gamma * L} \qquad \text{Equation 2.5}$$

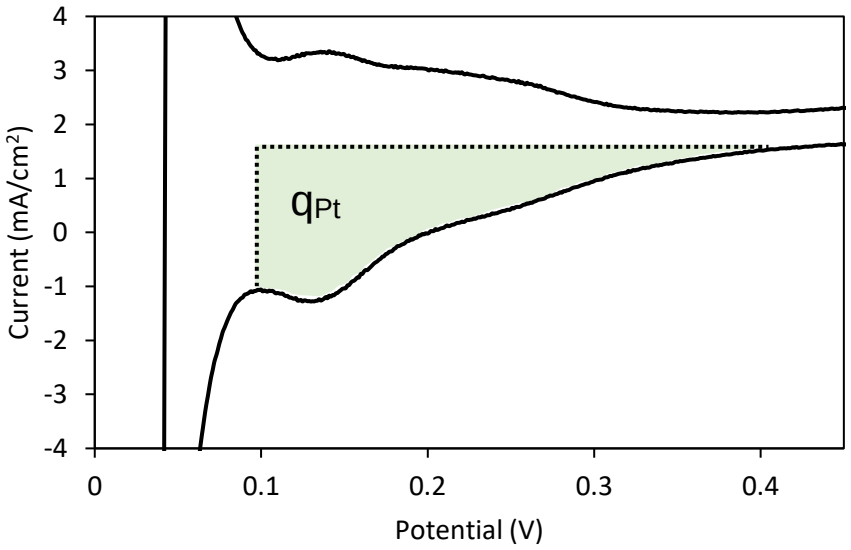

Figure 2.4: Example CV curve for ECSA measurement where the shaded region is charge density (C/cm^2)

2.3.2 Linear Sweep Voltammetry

Linear sweep voltammetry (LSV) is used to study hydrogen crossover *in situ*. The anode is fed humidified hydrogen and serves as both the reference and counter electrode, while the cathode (working electrode) is supplied with humidified nitrogen. Using a potentiostat, the cathode voltage is swept from 0.04 V to 0.90 V (vs. SHE) and the corresponding current is recorded.

Current arises from electrochemical oxidation of any molecular hydrogen which diffuses across the membrane from anode to cathode. From the current, the rate of hydrogen crossover can be calculated.[8] Crossover can be affected by operating parameters (temperature, pressure, and humidity) as well as membrane type and thickness.

2.3.3 Electrochemical Impedance Spectroscopy

Electrochemical impedance spectroscopy (EIS) is a technique which applies an AC signal at a set frequency to the DC current or voltage and the corresponding impedance is recorded. Plotting the imaginary and real impedances results in a Nyquist plot. EIS is a powerful tool which can be used to study charge transfer, ohmic, and mass transfer resistances.[2] For the purposes of this dissertation, EIS was primarily used to determine high frequency resistance (HFR). HFR is a measurement of both membrane resistance and contact resistance at the electrode/membrane interface.[9]

2.3.4 The Tafel Slope and Catalytic Activity

The oxygen reduction activity of an MEA is dictated by not only the catalyst, but by operating parameters such as temperature, humidity, pressure, and flowrate, as well as ionomer distribution/content. The Tafel slope is often used as an *in situ* means to evaluate the oxygen reduction activity of a cathode catalyst, where the greater the slope the lower the catalytic activity. The Tafel slope can be calculated from the Tafel equation (Equation 2.6) where ΔV_{act} is activation voltage loss and b is the slope.

$$\Delta V_{act} = a + b * log(i) \qquad \text{Equation 2.6}$$

This equation is of a similar form to Equation 2.2, and so it may be re-written as Equation 2.7, where E_{eq} represents the open circuit voltage of the cell at a defined temperature and pressure.

$$E_{cell} = E_{eq} - 2.3\frac{RT}{\alpha F} log\left(\frac{i}{i_0}\right) \quad \text{Equation 2.7}$$

Another common metric for catalytic activity is mass activity. Mass activity is defined in the DOE FC-PAD project literature as the current per gram of Pt at 0.9 V, 80 °C, 150 kPa_{abs}, under fully humidified H_2/O_2 after correction for hydrogen crossover and HFR.[10] To determine mass activity, current density is scanned from 200 to 2 mA/cm^2 under O_2 at a partial pressure of 100 kPa and the corresponding voltage is recorded (here current density is given by the applied current divided by the geometric MEA footprint). Operation at these low current densities mitigate transport overpotentials.[11] Current is corrected by adding the crossover current (collected from LSV) to the measured current. Ohmic overpotential is calculated from Equation 2.3 using the crossover-corrected current and the HFR calculated from EIS. This value is then added to the measured voltage to correct for iR loss. By fitting the corrected voltage (E_{cell}) and current (i) data to Equation 2.7 using the method of least squares, the constants E_{eq}, i_0, and α may be calculated. Once the constants are known, the current at 0.9 V may be calculated.

2.4 MEA Fabrication Methods

When preparing a fuel cell cathode, it is important to maximize the three-phase reaction boundary. This is where electrons, protons, and molecular oxygen meet at a platinum particle for oxygen reduction. Protons are transported through the ionomer, meaning if there is insufficient ionomer at a given platinum particle, or the ionomer is not adequately hydrated, the catalyst site

will not be electrochemically active. A site will also be inactive if electron conductivity is too low, either due to the lack of a conductive material or isolation of the electron conductor. Lastly, oxygen must be able to diffuse to the catalyst site via electrode void space. Oxygen transport resistance may arise due to ionomer blocking catalyst sites or product water filling void spaces (flooding).

Commonly, electrode inks (catalyst and ionomer dispersed in an alcohol/water solvent) are sprayed or slurry cast onto a substrate. The substrate may be the carbon paper GDL, the proton exchange membrane, or a blank polymer (Teflon®) substrate. Deposition onto the GDL is referred to as the gas diffusion electrode (GDE) method[12–19] while spraying onto the membrane is called the catalyst coated membrane (CCM) method.[13,20–24] When the electrode is deposited on a blank polymer film substrate, the electrode is then transferred onto the membrane using the decal transfer method.[23–27]

Early PEMFC electrodes were prepared via the GDE method using Pt black catalyst[17] and Teflon®.[18] The large platinum particle size (greater than 10 nm diameter) led to poor platinum utilization and a loading of ~4 mg_{Pt}/cm^2 was necessary to obtain appreciable power.[17] Depositing platinum on a porous carbon support allowed for the formation of small platinum particles and high electron conductivity.[28] Further advancement was made when researchers began impregnating the catalyst layer with ionomer, increasing the three-phase reaction zone where solid catalyst, gaseous oxygen, and protons in water meet.[15,16] The GDE method has proven useful for mass production but has several shortcomings. Catalyst may become imbedded in the gas diffusion media which is subsequently washed out during fuel cell operation, wasting

materials.[21] Additionally, the hot-pressing step used to bind the GDE to the membrane may result in structural deformation of both the catalyst layer[14] and the diffusion media,[23] creating a higher electronic resistance and water/gas transport limitations.

MEAs prepared via the CCM method exhibited an improved electrode/membrane contact,[13] improved catalyst utilization,[22] and higher power.[23,24] However, depositing the electrode ink directly onto the membrane can result in severe membrane swelling which affects MEA lifetime due to creep-failure.[29] Catalyst deposition at a high temperature[21] and use of vacuum plates have alleviated membrane swelling during catalyst coating, but this is not an attractive solution for large scale MEA fabrication.

Spraying an electrode onto a thin film Teflon® substrate and transferring the electrode onto the membrane eliminates the concern of GDL damage and catalyst loss associated with GDEs and membrane swelling that may occur during the CCM process. The decal transfer process poses its own problems, however. For example, during electrode deposition, catalyst and ionomer are prone to segregation, resulting in flooding during fuel cell operation.[30] The decal transfer process also requires many steps, including exchanging the catalyst layer ionomer and membrane into the salt form so deposition and transfer may occur at high temperatures (which improves mechanical properties of the materials).[24–26] Afterwards the MEA must be boiled in sulfuric acid to re-protonate the ionomer. Additionally, determining catalyst loading using the decal transfer method is difficult due to the possibility of uneven or incomplete transfer of the electrode to the membrane.[23]

2.5 Electrode Morphology

Typical GDE, CCM, or decal transfer electrodes are prepared via slurry deposition (i.e., spray, doctor blade, brushing). Although this is a facile method for electrode production there remain concerns about stability of the electrocatalyst and carbon support[31,32] as well as utilization of the catalyst.[33–36] Alternative electrode morphologies, such as nanostructured thin films (NSTF) from 3M Company,[31,32,34,37,38] electrospraying,[36,39–42] electrospinning/electrospraying,[35,43,44] and the electrospun fiber electrodes as described by Pintauro and co-workers,[33,45–51] have all exhibited improvements over conventional electrode fabrication methods.

NSTF electrodes are prepared by depositing platinum onto oriented whisker supports of an organic pigment material. The resulting electrode is carbon-powder and ionomer free and approximately 0.5 µm thick. The thin electrode is then pressed with a proton exchange membrane, compressing the whiskers to 0.23 µm and imbedding approximately 20% of the whisker length into the membrane.[34] At 80 °C and cathode loadings of ~0.2 mg_{Pt}/cm^2, a NSTF electrode prepared from a PtCoMn catalyst generated comparable power to a conventional PtCo/C electrode MEA (1020 mW/cm^2 vs. 975 mW/cm^2 at 0.65 V, respectively). The benefit of the NSTF structure is most notable at low loadings, where at ~0.053 mg_{Pt}/cm^2 the NSTF MEA produced 820 mW/cm^2 at 0.65 V whereas the convention PtCo/C MEA only generated 430 mW/cm^2.[38] NSTF MEAs are also highly robust. A 2006 study revealed that after high-voltage cycling (between 0.6 V and 1.2 V at a scan rate of 20 mV/s), a platinum NSTF electrode MEA lost only 22% of initial power (600 to 468 mW/cm^2 at 0.6 V) whereas a conventional Pt/C electrode MEA underwent a power loss of 42% at 0.65 V (462 to 270 mW/cm^2).[31]

There are two major drawbacks of the NSTF electrode architecture. Due to the low porosity of the electrodes, flooding is a major source of power loss at low operating temperatures. At 0.6 V and 40 °C a NSTF electrode MEA only produced 114 mW/cm^2 while a conventional electrode MEA produced 486 mW/cm^2. Although temperature is lower than what is typically used in vehicular fuel cells, the flooding could cause major performance problems for vehicles during start-up while temperature is still low.[32] Additionally, since only 20% of the length of the platinum whiskers are in direct contact with ionomer, protonic conductivity is much lower than what is reported for conventional catalyst layers (0.1 S/m vs. 9 S/m at 80 °C and 100% humidity). Although the discrepancy in conductivity does not seem to drastically affect the performance at high humidity, power drops significantly for NSTF MEAs at 30% RH, producing half the power of a conventional MEA operating under the same conditions.[34]

Similar to conventional sprayed electrodes, electrosprayed electrodes are prepared from a catalyst/ionomer electrode ink. The key difference is the way the ink is deposited onto a substrate. The ink is pumped through a capillary which has an applied voltage bias. The imposed electric field causes the ink to form small, mist-like droplets which land on a grounded collector. The small droplet size results in a more uniform distribution of catalyst and ionomer, leading to improved fuel cell performance. For example, Benitez et al. prepared electrosprayed electrode MEAs and reported 60% higher power than what a commercially available MEA produced. This was attributed to increased porosity and platinum utilization.[41] It was also determined that due to improved ionomer distribution, less ionomer was needed for electrosprayed electrodes.[41] Takahashi et al. have also shown that electrospraying leads to a more uniform distribution of catalyst and ionomer, and reported that activity more than doubled when going from a

conventional electrode to an electrosprayed electrode.[36] Unfortunately, none of the aforementioned researchers investigated the stability of these electrodes.

The next section of this chapter will discuss the use of electrospun materials for fuel cell electrodes.

2.6 Application of electrospinning for the fabrication of proton-exchange membrane fuel cell electrodes

Adapted from K. Waldrop, R. Wycisk, P. N. Pintauro, *Curr. Opin. Electrochem* **2020,** 21, 257-264 with permission from Elsevier.

2.6.1 Introduction

The hydrogen/air proton-exchange membrane fuel cell (PEMFC) is a promising energy conversion device for a variety of applications in commercial, residential, industrial, and transportation sectors. The widespread use of PEMFCs, however, is hindered by the high price and inadequate durability of the platinum-based cathode for oxygen reduction.[52] Cathode performance has been addressed primarily by focusing on new oxygen reduction reaction catalyst materials, e.g., carbon supported platinum metal alloys,[53] core-shell nanomaterials,[54] shape-controlled catalyst structures,[55] carbon nanotube supports,[56] Pt nanowires,[57] and oriented Pt-coated whiskers.[32] Although these studies have yielded promising results in terms of catalytic activity and potential cost savings by lowering Pt loading, they have not led to a cathode that could meet the cost, power density, and durability targets of end users, especially the automotive industry. Alternative studies attempted to increase power without substantially increasing Pt loading through improvement of the morphology of the electrodes, primarily the cathode, in order to

maximize catalyst contact with reactant gases while maintaining sufficient pathways for proton and electron conduction. Surprisingly, over the past 25 years there have been few advancements in electrode design/structure for improved catalyst activity and utilization. Most fuel cell MEAs are fabricated today using a decal transfer method,[27] wet coating or spraying catalyst and a polymer binder onto carbon paper GDLs,[19] or by depositing a catalyst and polymer binder onto the opposing surfaces of a proton-exchange membrane (PEM) (the catalyst coated membrane method).[20] In the last decade, a very promising electrode fabrication technique has emerged, which utilizes fiber electrospinning, and which is the subject matter of this opinion paper.

Electrospinning is a simple and highly versatile method to produce high aspect ratio polymeric and composite fibers with controllable diameter and composition. During fiber electrospinning, a polymer solution or melt is extruded through a spinneret under the influence of an electric field. High shear forces at the spinneret tip and fast solvent evaporation (or polymer melt cooling) prevent de-mixing of the ink components (e.g., ionomer binder and catalyst) leading to well-formed fibers with minimal nanoparticle agglomeration. Additionally, by controlling the electrospinning conditions, one can alter the internal fiber microstructure.

Electrospinning is currently used to fabricate a variety of fiber-based products including filtration media,[58] medical and pharmacological products,[59,60] nonwoven fabrics,[61] and sensors.[62] This chapter highlights advances in the application of electrospinning for the fabrication of nanofiber-based electrodes in a H_2/air PEMFC with the focus on: (i) correlating fiber structure and composition with fuel cell power output and durability, (ii) contrasting electrospun fiber mat

cathodes with those made by slot-die coating or catalyst spraying, and (iii) assessing the future prospects of electrospinning for the fabrication of high performance PEMFCs.

Primarily, electrospinning has been used for PEMFC electrode fabrication in two different ways: (1) for the preparation of catalyst support, where electrospun fibers are pyrolyzed or calcinated to produce carbon or metal-oxide fibers which are then segmented, decorated with catalyst, dispersed with a binder, and incorporated into a conventional coated or sprayed electrode MEA, and (2) for direct fabrication of fiber mat electrodes, where polymer fibers are used as-spun in the electrode and commercial catalyst can be either included in the electrospinning ink or sprayed onto the fibers. The first method is illustrated in Figure 2.5a where a carbon or inorganic support is first made from an electrospun and pyrolyzed precursor, followed by precious metal deposition. The mat is then pulverized into a short-fiber powder, mixed with an ionomer solution, and the resulting ink is deposited onto a PEM or GDL using conventional slurry coating/spraying methods. An example of the second method is depicted in Figure 2.5b, where a conventional fuel cell catalyst powder (e.g., Pt on a carbon support) is combined with ionomer, a carrier polymer, and solvent to form an ink, which is then electrospun into a fiber mat electrode. The fibers can be deposited directly onto a GDL or PEM.

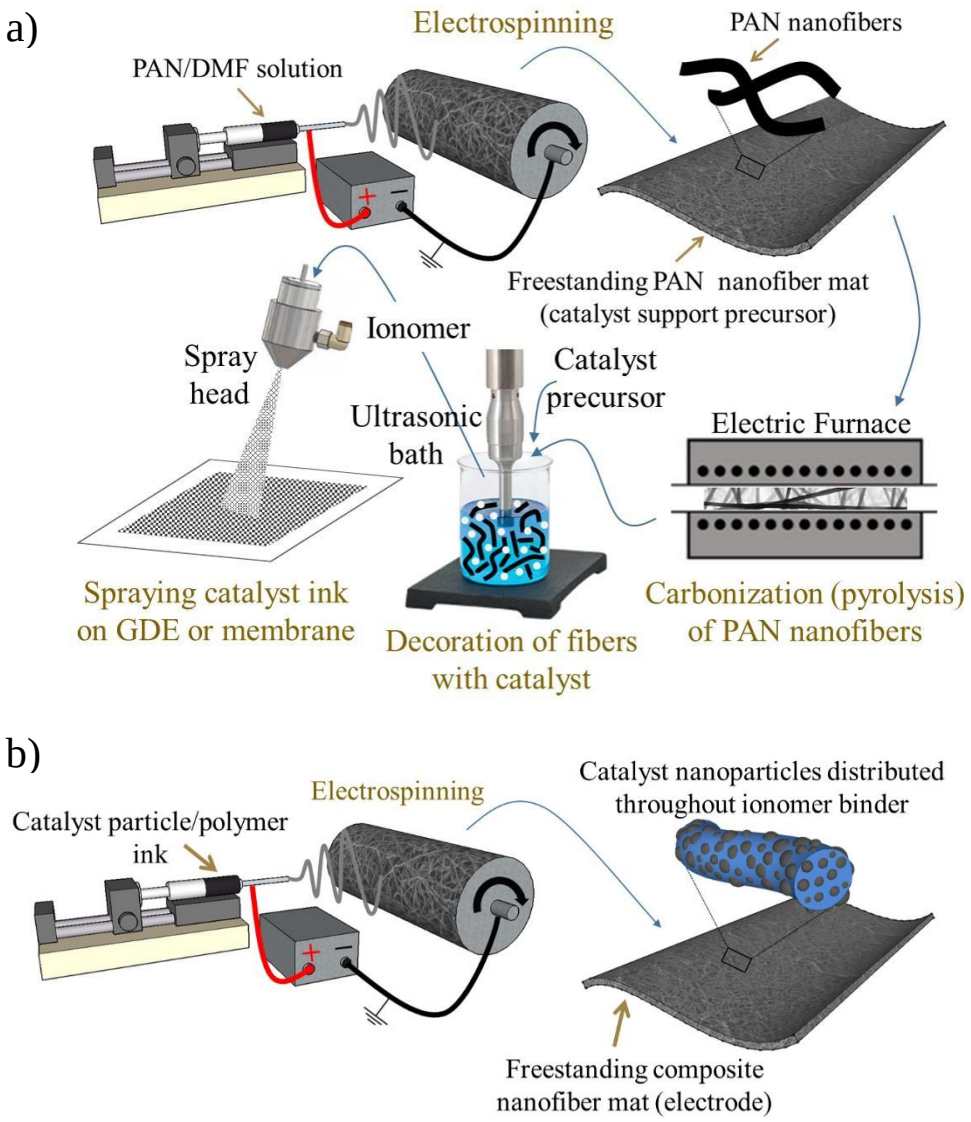

Figure 2.5: a) Preparation of an electrode from carbon fibers prepared through the electrospinning of PAN nanofibers, their carbonization, decoration with in-situ generated catalyst nanoparticles and deposition, after adding ionomer binder, onto a GDL or membrane.

2.6.2 Fuel Cell Catalysts Derived from Electrospun Carbon and Non-Carbon Nanofiber Supports

Electrospun carbon fiber supported catalysts have been investigated as a potential alternative to conventional carbon black-supported precious metal powders in PEMFC electrodes due to their

high electrical conductivity, good mechanical properties, and high surface area. Additionally, the fiber diameter and/or internal porosity can be controlled during electrospinning and thermal post-treatment, which might improve precious metal site activity and durability.

One way of preparing the catalyst from pyrolyzed carbon fibers is reported by Park et al.[63] Electrospun polyacrylonitrile (PAN) nanofibers were thermally stabilized at 280 °C in air and then carbonized at 1000 °C under nitrogen. The resultant carbon nanofibers with a mean diameter of 250 nm were ground into a fibrous powder (CFP), surface-oxidized in a boiling H_2SO_4-HNO_3 mixture, and then decorated with Pt nanoparticles by in-situ reduction of H_2PtCl_6 with ethylene glycol. The MEA cathodes with Pt/CFP catalyst had a high electrochemical surface area (ECSA) (74.5 m^2/g_{Pt} vs. 30.8 m^2/g_{Pt} for a commercial Pt on Vulcan carbon catalyst), with an average Pt particle size of 2.6 nm vs. 3.2 nm for the commercial catalyst. Fuel cell performance was poor for the Pt/CFP cathode MEAs; only 540 mW/cm^2 at 0.6 V was produced for an anode/cathode Pt loading of 0.5 mg/cm^2 each, with fully humidified H_2 (150 sccm) and O_2 (200 sccm).

In another study,[64] electrodes were prepared from pyrolyzed electrospun mats of a PAN/poly(methyl methacrylate) mixture followed by fiber decoration with Pt nanoparticles. The electrospun carbon nanofiber (eCNF) mat was used directly as the cathode in a MEA, without pulverizing the fibers. The authors speculated that the highly open interconnected 3D fibrous catalyst layer would improve gas transfer and facilitate water drainage (i.e., prevent electrode flooding), thus increasing fuel cell power generation. H_2/O_2 fuel cell experiments at room temperature with a 0.4 mg_{Pt}/cm^2 cathode, however, showed low power output with the Pt/eCNF cathode, a maximum power density of 130 mW/cm^2, with no power output improvement versus

a conventional cathode with Johnson-Matthey commercial Pt/C powder. Pt/eCNF cathode fiber mats were also examined by Chan,[65,66] starting with electrospun poly(acrylonitrile-co-methyl acrylate) fibers. The effects of fiber alignment, Pt and ionomer loading and distribution, and the method of Pt deposition on the eCNF support on fuel cell performance were investigated. MEAs performed best when Pt was deposited on eCNF by an electroless plating method (0.157 mg_{Pt}/cm^2 with an I/C ratio of 0.158), where the power density was 670 mW/cm^2 at 0.65 V and 68 °C, for fully humidified H_2/air.

Carbon supports for fuel cell Pt catalysts, while possessing several advantageous characteristics, i.e., controllable porosity, high conductivity, and low cost, suffer from poor electrochemical stability at high potentials, which can arise in a MEA during stop/start conditions. Recently, transition metal oxides of high surface area and relatively high electronic conductivity, such as TiO_2, SnO_2 and WO_2, have been investigated as potential replacements for carbon in fuel cell electrodes. Cavaliere's group reported on a novel corrosion-resistant Pt support from electrospun Nb doped SnO_2 hollow fibers that were ultrasonically segmented, mixed with ionomer (Nafion®) solution, and then coated onto carbon paper GDLs.[67,68] Fuel cell tests with H_2/O_2 at 80 °C, showed that an MEA with a Pt/Nb–SnO_2/Nafion cathode at 0.4 mg_{Pt}/cm^2 generated low power in beginning-of-life experiments (0.41 W/cm^2 at 1 A/cm^2 vs. 0.96 W/cm^2 for a Pt/C reference MEA), which most probably originated from the lower electron conductivity of the oxide support as compared to carbon. No degradation in performance, however, was observed for the Pt/Nb–SnO_2/Nafion cathode during voltage cycling accelerated stress tests, and SEM analyses of cathodes before and after voltage cycling revealed that the Nb-SnO_2 stabilized platinum nanoparticles against dissolution, migration, and re-precipitation in the membrane.

2.6.3 Electrospun Polymer/particle Electrodes for PEM Fuel Cells

Rather than pyrolyze polymer fibers, one can prepare and directly use a catalyst/binder fiber mat as the electrode in a H_2/air PEMFC. Here, conventional precious metal catalyst powders are employed, and the polymeric binder is retained after electrospinning and exploited for optimum fuel cell operation (primarily, for proton conductivity). Due to the rapid stretching of the electrified jet and the quick evaporation of the solvent, extremely strong shear stresses develop within the ejected fiber as it travels toward the grounded collector. These stresses not only orient the polymer chains but also disaggregate the catalyst nanoparticles within the jet leading to their enhanced wetting with ionomer, while the nearly instant solidification compacts and freezes this uniform dispersion into a robust, highly conductive (both, ionically and electronically), porous nanofiber with high catalytic activity. This concept is illustrated in Figure 2.6. Such systems have improved water management due to high inter-fiber electrode porosity and increased mass activity and electrochemically active surface area due to intra-fiber porosity. Consequently, MEAs prepared with fiber mat electrodes exhibit higher power output and better durability than MEAs prepared with conventional electrodes.[33,35,43–51,69–71] Commercially available fuel cell catalysts, including carbon-supported Pt, Pt-alloys, and precious-metal-free (PGM-free) powders can be utilized in fiber mats if the particle size is < 200 nm. The fiber spinning technique can easily accommodate new catalyst powders with improved activity and new proton conducting ionomer binders as they are developed/discovered. Most papers in the literature deal with the fabrication and performance of fiber mat cathodes in a H_2/air PEMFC, because the oxygen reduction reaction kinetics are sluggish and mass transfer effects (oxygen transport to reaction sites and water removal) play an important role, particularly at high current density operation.

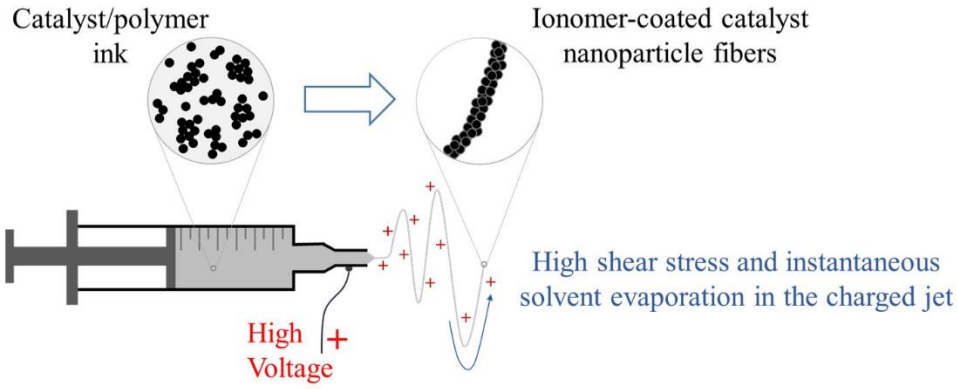

Figure 2.6:Nanoparticle fiber formation mechanisms: (1) the rapid stretching of the electrified jet and the rapid evaporation of the solvent generate strong shear stresses within the ejected fiber which orient the polymer chains and disaggregate the catalyst nanoparticles, (2) the nearly instant solidification compacts and freezes this uniform dispersion into a robust, porous nanofibers.

2.6.4 Fiber electrodes prepared by particle/polymer electrospinning

Electrospun particle/polymer electrodes were first reported in a 2009 paper by Kotera et al. from Asahi Glass Co.[69] Fibers were produced using a coaxial core-sheath needle with a catalyst/ionomer core (perfluorosulfonic acid ionomer) and a poly(ethylene oxide) (PEO) sheath. Of particular note was the authors' assertion that fibers could not be electrospun without the PEO sheath. The fiber electrode MEA exhibited higher power than an in-house slurry electrode MEA with the same platinum loading (0.2 mg_{Pt}/cm^2). Under fully humidified H_2/air at 95 °C and 150 kPa_{abs}, fiber and slurry electrode MEAs generated a maximum power of 445 mW/cm^2 and 350 mW/cm^2, respectively. Following this work, a series of papers was published by Pintauro and

co-workers detailing single needle electrospinning of nanofiber electrode mats where a carrier polymer was added to the spinning solution (catalyst and Nafion perfluorosulfonic acid ionomer) to eliminate the need for a core-shell fiber morphology.[33,45–51]

Pintauro and co-workers first published on electrospun fiber electrodes containing commercial Pt/C catalyst, ionomer, and poly(acrylic acid) (PAA) carrier.[33,45,46,49] Fibers had an average diameter of 300 nm, no visible spray droplets, and a uniform distribution of catalyst across the length of the fibers, as shown by the SEM image in Figure 2.7a. A fiber electrode MEA with a cathode catalyst loading of 0.1 mg_{Pt}/cm^2 outperformed a conventional spray electrode MEA with a cathode catalyst loading of 0.4 mg_{Pt}/cm^2 in terms of Pt-mass normalized oxygen reduction reaction (ORR) activity (230 vs. 110 A/g_{Pt}), and electrochemically active surface area (ECSA, 114 vs. 60 m^2/g_{Pt}). The power density output was similar between the two MEAs (~500 mW/cm^2 at 0.6 V in fully humidified H_2/air at 80 °C and ambient pressure), despite the spray having 4-times higher platinum content at the cathode.[45] Fiber electrode MEAs also exhibited improved durability over sprayed electrode MEAs (8% maximum power loss vs. 32% loss), as measured before and after a voltage cycling Pt dissolution accelerated stress test (30,000 voltage cycles between 0.6 and 0.95 V).[49] In one study, PVDF was used as a carrier polymer to increase the hydrophobicity of a fiber mat cathode, to better expel product water during fuel cell operation and minimize carbon corrosion during fuel cell start-up and shut-down.[47] The use of a 1:1 weight ratio Nafion:PVDF binder in a Pt/C particle cathode MEA resulted in constant fuel cell power output during a carbon corrosion voltage cycling accelerated stress test (1,000 voltage cycles between 1.0 and 1.5 V). Comparatively, a MEA with cathode fibers prepared with a Nafion ionomer and PAA carrier lost 40% of its initial power, and a conventional slurry cathode MEA with

neat Nafion binder lost 50%. The use of PVDF with Nafion as the binder in fiber mat cathodes also stabilized the long-term power output of a MEA during H_2/air fuel cell operation with a PGM-free oxygen reduction catalyst.[51] In a more recent study, PEO was used as the carrier polymer for electrospinning particle/polymer fiber mat electrodes with Nafion ionomer.[48] These fibers exhibited exceptionally high power (10% higher maximum power as compared to that measured with a Nafion/PAA fiber binder at the same Pt loading). The use of PEO as the fiber carrier polymer also produced a cathode mat that generated high power at both low and high relative humidity feed gas conditions (for hydrogen and air relative humidity between 40% and 100%). For example, a fiber electrode MEA prepared with PEO and a cathode catalyst loading 0.1 mg_{Pt}/cm^2 produced 840 mW/cm^2 maximum power at 100% RH and 820 mW/cm^2 maximum power at 40% RH (H_2/air gas feeds at 80 °C and 200 kPa_{abs}). The fuel cell performance of electrospun particle/polymer electrodes was further probed by Si et al., who showed that nanofiber electrodes lead to lower activation overpotentials.[70] In general, fiber mat electrodes that generated the highest power also showed the largest power loss after a voltage cycling accelerated stress test, although the magnitude of the power loss in a fiber mat was always less than that seen in a conventional slurry coated or sprayed cathode.

Hong et al. described the performance of a particle/polymer fiber mat cathode composed of a commercial Pd/C catalyst, with a binder of Nafion and PAA, where the fiber surface was altered after electrospinning by the underpotential deposition of a thin Pt skin layer.[71] The resulting fiber electrode (denoted as Pd/C@Pt_{skin}), which contained 61 wt.% Pd/C@Pt_{skin}, 25 wt.% Nafion, and 14 wt.% PAA, exhibited a significantly higher ORR activity, as compared to a spray electrode using commercial Pt/C (570 vs. 140 mA/mg_{Pt}). The fiber morphology also led to a high-

power generation at a very low platinum loading in a H_2/air fuel cell operating at 65 °C, e.g., a maximum power of 650 mW/cm^2 at a catalyst loading of 0.019 mg_{Pt}/cm^2 versus 550 mW/cm^2 for a MEA with a sprayed commercial Pt/C cathode at 0.1 mg_{Pt}/cm^2. Hong also reported an improvement in the metal dissolution durability when using a fiber mat cathode. After 30000 voltage cycles between 0.6 V and 1.0 V, the Pd/C@Pt_{skin} fiber cathode MEA lost 15% of initial peak power, while after only 10000 cycles, the conventional MEA lost ~23% of peak power.

2.6.5 PEMFC electrodes prepared with neat polymeric electrospun fibers and sprayed catalyst

There have been multiple studies that examined modified fiber mat fuel cell electrode morphologies, where fiber electrospinning was used during electrode fabrication. One approach was to electrospin ionomer fibers, using a perfluorosulfonic acid (PFSA) ionomer and PAA as the carrier polymer, while simultaneously spraying catalyst and PFSA without a carrier polymer.[35,43,44] The electrode mat consisted of highly uniform ionomer nanofibers ~200 nm in diameter with interspersed catalyst spray droplets with diameters primarily in the range of 50-300 nm (see Figure 7b).[36] A spray/spun cathode with a loading of 0.052 mg_{Pt}/cm^2 produced a maximum power of 656 mW/cm^2 during a hydrogen/air fuel cell test (fully humidified H_2/air at 80 °C and 272 kPa_{abs}), whereas a conventional sprayed cathode at 8-times the Pt loading (0.42 mg_{Pt}/cm^2) produced just 28% more power (839 mW/cm^2). The increase in platinum utilization was attributed to an increase in the triple phase (gas/catalyst/ionomer) boundary and rapid removal of product water. When 1 wt.% polytetrafluoroethylene (PTFE) was added to the Nafion fibers in a similar spray/spun cathode, the maximum power output increased by 10% due to the hydrophobicity of PTFE which helped to expel water.[44] Unfortunately, there were no reports on the durability of spray/spun electrodes and higher Pt loadings were not examined.

Another type of fiber-based catalyst/polymer fuel cell cathode was reported by Choi et al., where catalyst was sprayed onto a pre-formed mat of electrospun Nafion fibers.[72] An SEM image of this electrode morphology is shown in Figure 2.7c. MEAs with such a cathode generated more power than a conventional sprayed electrode MEA in a H_2/air fuel cell (480 mW/cm^2 vs. 400 mW/cm^2 maximum power at 80 °C, 100% RH, and 180 kPa_{abs}) due to the cathode's high surface area and lower protonic resistance. More recently, Sun et al. added pre-formed electrospun Nafion fibers (catalyst-free, made by adding polyvinylpyrrolidone carrier polymer) to a catalyst ink (composed of Pt/C, Nafion dispersion, and alcohol/water solvent).[73] MEAs were made by spraying the resulting ink onto the opposing surfaces of a Nafion 211 membrane, as can be seen in Figure 2.7d. With such an MEA design, the authors found improved catalyst layer proton conductivity and higher power output vs. a conventional slurry electrode MEA, e.g., a maximum power of 1.35 vs. 1.0 W/cm^2 for H_2/O_2 fuel cell operation at 70 °C, ambient pressure, and 100% relative humidity feed gases.

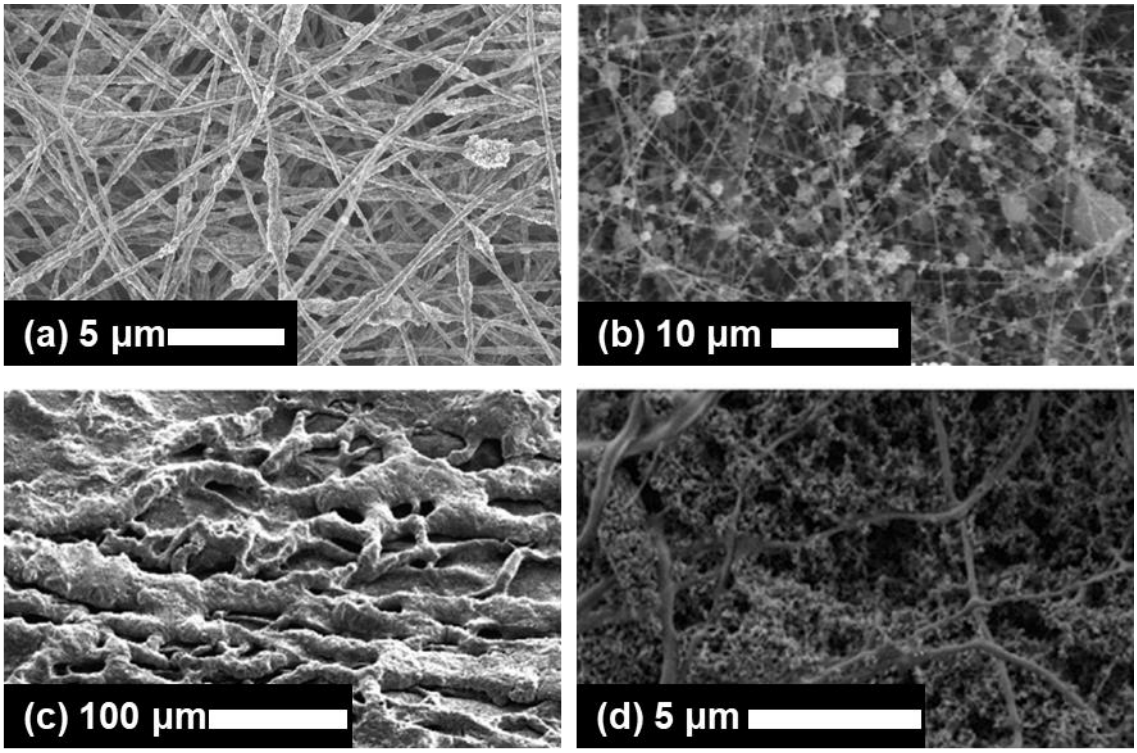

Figure 2.7: Scanning electron micrographs of electrodes prepared by a) particle/polymer electrospinning reproduced from [74] with permission from ECS, b) simultaneously spinning polymer fibers and spraying a particle/polymer ink reproduced from [75] with permission from Elsevier, c) spraying a particle/polymer ink onto a Nafion fiber mat reproduced from [76] with permission from Elsevier, and d) spraying a particle/polymer ink which also contains re-dispersed catalyst-free Nafion fibers reproduced from [77] with permission from ACS.

2.6.6 Conclusions

Electrospinning has proven to be a versatile and robust technique for energy materials fabrication. Use of electrospun catalyst support materials allow for greater electrochemically active surface area,[64] relatively high power,[66] and improved durability[68] depending on the materials and procedures used. Other work has shown that readily available commercial catalysts

can be incorporated into polymer fiber networks by combining particles and polymer into a single electrospinning ink. [33,35,51,69–71,43–50]These materials have proven to be highly durable,[47,49] with improved access to catalyst sites,[33] and high power at ultra-low platinum loadings.[71] While research has also focused on electrospinning polymer fibers and spraying catalyst, either simultaneously[35,43,44] or consecutively,[72,73] the materials did not match the performance of single-needle particle/polymer fibers. As summarized in Table 2.1, commercial catalyst/polymer electrospun fibers vastly outperform the other morphologies discussed in this chapter.

Table 2.1: Summary of power densities at 0.65 V for different cathode morphologies

Cathode Type	Pt on fiber eCNF support [67]	Pt on fiber Nb-SnO2 support [69]	PtCo/C fiber cathodes [50]	Pd/C@Pt_{skin} fiber cathodes [72]	Simultaneous Nafion spin/Pt/C spray [36]
Pt Loading (mg_{Pt}/cm^2)	0.157	0.5	0.1	.019	0.052
Power Density at 0.65 V (mW/cm^2)	670	260	751	325	390
Feed Gases	H_2/air	H_2/O_2	H_2/air	H_2/air	H_2/air
Operating Temperature (°C)	68	80	80	65	80
Pressure (kPa_{abs})	150	200	200	N/A	272

As the push for large scale commercialization of fuel cell electric vehicles continues, the spinning of catalyst and polymer from a single ink warrants genuine consideration. Such materials are highly adaptable and can easily incorporate a variety of catalysts and polymers. The unique morphology helps to minimize ionomer and catalyst aggregation, leading to increased availability of active sites and decreased ohmic overpotential. Furthermore, the highly porous structure

allows for facile removal of product water, resulting in lower reactant gas transport resistance and improved durability. These features make particle/polymer fiber electrodes promising for future development of fuel cell electric vehicles.

2.7 Project Objectives and Remaining Dissertation Format

The works published by Zhang,[45] Brodt,[33,46,47] and Slack[49–51] during their tenure in the Pintauro laboratory have shown electrospun fiber electrode MEAs to be highly active and durable compared to conventional electrode MEAs. To further understand and improve the performance of fiber electrode MEAs, this dissertation will detail the fabrication and characterization of the following:

(1) Fiber electrodes which utilize a PtNi/C cathode catalyst and a Nafion/poly(acrylic acid) binder: Previous work by Slack et al[49] showed the use of a PtCo/C cathode catalyst led to enhanced MEA performance at beginning-of-life (BoL). This chapter will explore the use of a PtNi catalyst and compare both performance and durability to the work of Slack. (Chapter 3)

(2) Fiber electrode prepared using Nafion in the sodium-salt form: Use of Nafion in the salt form allows for removal of carrier polymer, improving performance at both high and low humidity operation. (Chapter 4)

(3) Fiber electrode MEAs with a high ($0.2 mg_{Pt}/cm^2$) cathode catalyst loading with a neat Nafion binder: Heavy duty fuel cell vehicles operate at high cathode loadings. This chapter will explore the effect of cathode loading and preparation on the performance and durability of fiber electrode MEAs. (Chapter 5)

(4) The water distribution profile under different fuel cell operating conditions for MEAs prepared with sprayed and nanofiber mat electrodes via neutron scattering images. (Chapter 6)

2.8 References

1. K. A. Mauritz and R. B. Moore, *Chem. Rev.*, **104**, 4535–4585 (2004).

2. J. Zhang, Y. Tang, C. Song, and J. Zhang, *J. Power Sources*, **172**, 163–171 (2007).

3. C. Lee et al., *J. Mater. Sci.*, **48**, 3665–3671 (2013).

4. C. Shen, R. Wycisk, and P. N. Pintauro, *Energy Environ. Sci.*, **10**, 1435–1442 (2017).

5. D. C. Villa, S. Angioni, S. D. Barco, P. Mustarelli, and E. Quartarone, *Adv. Energy Mater.*, **4**, 1301949 (2014).

6. F. Barbir, *PEM Fuel Cells - Theory and Practice*, 2nd ed., p. 130–132, Elsevier, Boston, (2012).

7. K. Cooper, *Fuel Cell Mag.*, 1–3 (2009).

8. J. Zhang, H. Zhang, J. Wu, and J. Zhang, *PEM Fuel Cell Testing and Diagnosis*, Elsevier, Oxford, (2013).

9. K. R. Cooper and M. Smith, *J. Power Sources*, **160**, 1088–1095 (2006).

10. *Off. Energy Effic. Renew. Energy* https://www.energy.gov/eere/fuelcells/doe-technical-targets-polymer-electrolyte-membrane-fuel-cell-components.

11. H. A. Gasteiger, S. S. Kocha, B. Sompalli, and F. T. Wagner, *Appl. Catal. B Environ.*, **56**, 9–35 (2005).

12. E. Antolini, L. Giorgi, A. Pozio, and E. Passalacqua, *J. Power Sources*, **77**, 136–142 (1999).

13. M. G. Hosseini and R. Mahmoodi, *Int. J. Hydrogen Energy*, **42**, 10363–10375 (2017).

14. M. Prasanna, E. A. Cho, T.-H. Lim, and I.-H. Oh, *Electrochim. Acta*, **53**, 5434–5441 (2008).

15. S. Srinivasan, E. A. Ticianellli, C. R. Debrouin, and A. Redondo, *J. Power Sources*, **22**, 359–375 (1988).

16. S. J. Lee et al., *Electrochem. Acta*, **43**, 3693–3701 (1998).

17. E. J. Taylor, E. B. Anderson, and N. R. K. Vilambi, *J. Electrochem. Soc.*, **139**, L45–L46 (1992).

18. M. Uchida, Y. Aoyama, N. Eda, and A. Ohia, *J. Electrochem. Soc.*, **142**, 4143–4149 (1995).

19. M. S. Cogenli, S. Mukerjee, and B. Yurtcan, *Fuel Cells*, **15**, 288–297 (2015).

20. K.-H. Kim et al., *Int. J. Hydrogen Energy*, **35**, 2119–2126 (2010).

21. M. Hu et al., *Int. J. Hydrogen Energy*, **31**, 1010–1018 (2006).

22. A. Lindermeir, G. Rosenthal, U. Kunz, and U. Hoffman, *J. Power Sources*, **129**, 180–187 (2003).

23. T. Frey and M. Liinardi, *Electrochim. Acta*, **50**, 99–105 (2004).

24. J. H. Cho, J. M. Kim, J. Prabhuram, and S. Y. Hwang, *J. Power Sources*, **187**, 378–386 (2009).

25. J. Xie, K. L. More, T. A. Zawodzinski, and W. H. Smith, *J. Electrochem. Soc.*, **151**, A1841–A1846 (2004).

26. M. S. Wilson and S. Gottesfeld, *J. Electrochem. Soc.*, **139**, L28–L30 (1992).

27. S. Jeon et al., *Int. J. Hydrogen Energy*, **35**, 9678–9686 (2010).

28. I. D. Raistick, in *Proceedings of the Symposium on Diaphragms, Separators, and Ion-Exchange Membranes*, J. W. Van Zee, R. E. White, K. Kinoshita, and H. S. Burney, Editors, p. 172–178, The Electrochemical Society, Inc, Pennington (1986).

29. A. S. Alavijeh, R. M. H. Khorasany, A. Habisch, and G. G. Wang, *J. Power Sources*, **285**, 16–28 (2015).

30. J. Xie, G. Fernando, T. Zawodzinski, and W. Smith, *J. Electrochem. Soc.*, **151**, A1084–A1093 (2004).

31. M. K. Debe, A. K. Schmoeckel, G. D. Vernstrom, and R. Atanasoski, *J. Power Sources*, **161**, 1002–1011 (2006).

32. A. Kongkanand et al., *J. Electrochem. Soc.*, **159**, F676–F682 (2012).

33. M. Brodt, R. Wycisk, and P. N. Pintauro, *J. Electrochem. Soc.*, **160**, F744–F749 (2013).

34. P. K. Sinha, W. Gu, A. Kongkanand, and E. Thompson, *J. Electrochem. Soc.*, **158**, B831 (2011).

35. X. Wang, F. W. Richey, K. H. Wujcik, and Y. A. Elabd, *J. Power Sources*, **264**, 42–48 (2014).

36. K. Takahashi, K. Kakinuma, and M. Uchida, *J. Electrochem. Soc.*, **163**, F1182–F1188 (2016).

37. M. K. Debe, R. T. Atanasoski, and A. J. Steinbach, *ECS Trans.*, **41**, 937–954 (2011).

38. M. K. Debe, *J. Electrochem. Soc.*, **159**, B53–B66 (2012).

39. S. Cho, K. Tamoto, and M. Uchida, *Energy and Fuels*, **Just Accep** (2020).

40. A. M. Chaparro, B. Gallardo, M. A. Folgado, A. J. Martin, and L. Daza, *Catal. Today*, **143**, 237–241 (2009).

41. R. Benitez, J. Soler, and L. Daza, *J. Power Sources*, **151**, 108–113 (2005).

42. S. Martin, P. L. Garcia-Ybarra, and J. L. Castillo, *Int. J. Hydrogen Energy*, **35**, 10446–10451

(2010).

43. M. Hwang and Y. A. Elabd, *Int. J. Hydrogen Energy*, **44**, 6245–6256 (2019).

44. X. Wang et al., *Electrochem. Acta*, **139**, 217–224 (2014).

45. W. Zhang and P. N. Pintauro, *ChemSusChem*, **4**, 1753–1757 (2011).

46. M. Brodt et al., *J. Electrochem. Soc.*, **162**, F84–F91 (2015).

47. M. Brodt, R. Wycisk, N. Dale, and P. Pintauro, *J. Electrochem. Soc.*, **163**, F401–F410 (2016).

48. K. Waldrop et al., *ECS Trans.*, **92**, 595–602 (2019).

49. J. J. Slack et al., *J. Electrochem. Soc.*, **166**, F3202–F3209 (2019).

50. J. J. Slack et al., *J. Electrochem. Soc.*, **167**, 054517 (2020).

51. J. Slack et al., *ChemElectroChem*, **5**, 1537–1542 (2018).

52. S. Litster and G. McLean, *J. Power Sources*, **130**, 61–76 (2004).

53. S. Mukerjee and S. Srinivasan, *J. Electroanal. Chem.*, **357**, 201–224 (1993).

54. P. Strasser et al., *Nat. Chem.*, **2**, 454–460 (2010).

55. V. R. Stamenkovic et al., *Science (80-.).*, **315**, 493–497 (2007).

56. X. Wang, W. Li, Z. Chen, M. Waje, and Y. Yan, *J. Power Sources*, **158**, 154–159 (2006).

57. B. Li et al., *Appl. Catal. B Environ.*, **162**, 133–140 (2015).

58. Y. Wang, W. Li, Y. Xia, X. Jiao, and D. Chen, *J. Mater. Chem. A*, **2**, 15124–15131 (2014).

59. J. Wang and M. Windbergs, *Eur. J. Pharm. Biopharm.*, **119**, 283–299 (2017).

60. S. Meiners et al., *Polym. Int.*, **56**, 1340–1348 (2007).

61. Y. K. Kang, C. H. Park, J. Kim, and T. J. Kang, *Fibers Polym.*, **8**, 564–570 (2007).

62. D. Aussawasathien, J.-H. Dong, and L. Dai, *Synth. Met.*, **154**, 37–40 (2005).

63. J.-H. Park et al., *J. Appl. Electrochem.*, **39**, 1229–1236 (2009).

64. Y. Wang, J. Jin, S. Yang, G. Li, and J. Qiao, *Electrochem. Acta*, **177**, 181–189 (2015).

65. S. Chan et al., *J. Mater. Sci.*, **53**, 11633–11647 (2018).

66. S. Chan et al., *J. Power Sources*, **392**, 239–250 (2018).

67. S. Cavaliere, S. Subianto, I. Savych, D. J. Jones, and J. Roziere, *Energy Environ. Sci.*, **4**, 4761–4785 (2011).

68. I. Savych et al., *Phys. Chem. Chem. Phys.*, **17**, 16970–16976 (2015).

69. S. Kotera et al., **25**, 821–830 (2009).

70. D. Si et al., *Fuel Cells*, **18**, 576–585 (2018).

71. S. Hong et al., *Electrochem. Acta*, **245**, 403–409 (2017).

72. S. Choi et al., *Electrochem. Acta*, **268**, 469–475 (2018).

73. Y. Sun et al., *ACS Sustain. Chem. Eng.*, **7**, 2955–2963 (2019).

74. Reproduced with permission from. J Electrochem Soc 2019, 166:F3202. Copyright 2019, The Electrochemical Society.

75. X. Wang, F. W. Richey, K. H. Wujcik, and Y. A. Elabd, *J. Power Sources*, **246**, 42–48 (2014). Reprinted from J. Power Sources, 246. Copyright (2014), with permission from Elsevier.

76. S. Choi et al., *Electrochimica Acta*, **268**, 469–475 (2018). Reprinted from Electrochim Acta, 268. Copyright (2018), with permission from Elsevier.

77. Reprinted with permissions from Y. Sun et al., *ACS Sustain. Chem. Eng.*, **7**, 2955–2963 (2019). Copyright (2019), American Chemical Society.

CHAPTER 3 PERFORMANCE AND DURABILITY OF ELECTROSPUN FIBER CATHODES WITH PTNI/C CATALYST FOR HYDROGEN/AIR FUEL CELLS

3.1 Introduction

With the growing global demand for affordable and clean energy, hydrogen/air proton exchange membrane fuel cells (PEMFCs) are highly attractive for both automotive and stationary applications due to their zero-emissions operation, high efficiency, and low operating temperatures. While battery powered electric vehicles, such as those made by Tesla, Nissan's Leaf, and Chevrolet's Bolt, have gained a substantial foothold in the automotive market ,they are limited by mileage per charge and recharge time. For example, the 2020 Tesla Model S Long Range Plus claims 402 miles per charge[1] with recharging to 80% battery capacity taking at least 30 minutes.[2] Conversely, Toyota's 2015 Mirai, a fuel cell electric vehicle (FCEV), gets 300 miles per tank of H_2 and takes 3-5 minutes to refuel.[3] Honda and Hyundai have also released FCEVs but the ability of fuel cell-powered autos to realistically compete in the passenger vehicle market will depend on how successful researchers are in overcoming obstacles associated with the high price and long-term durability of the platinum catalyst in the fuel cell stack. The US Department of Energy[4] has set a target for total catalyst loading in a fuel cell membrane-electrode-assembly (MEA) of 0.125 mg_{Pt}/cm^2, but as it stands today, higher loadings are being used in commercial vehicles, e.g., 0.38 mg_{Pt}/cm^2 for the Toyota Mirai.[5] Therefore, the goal of many research efforts has been to reduce the Pt catalyst content in an MEA without sacrificing power and durability.

To minimize precious metal catalyst loading in a H_2/air fuel cell, researchers have focused their attention on improving the kinetics of the oxygen reduction reaction (ORR) cathode rather

than the hydrogen oxidation anode, because the former is rate limiting at moderate and high operating voltages. Efforts to improve the activity of oxygen reduction catalysts through alloying have shown promise. Platinum binds strongly with O and OH groups, and the slow desorption of these groups hinders the ORR.[6] Alloying platinum with a transition metal shortens the Pt-Pt bond length which weakens the bond strength of Pt-O and Pt-OH, thus allowing for improved catalytic mass activity.[7–9] Recently, Slack et al. found that the ORR mass activity of a PtCo/C nanofiber cathode was higher than that for an MEA with a Pt/C fiber mat cathode (270 mA/mg_{Pt} vs 160 mA/mg_{Pt}) with 30% higher fuel cell power generation.[10] With such high activity catalysts, the total mass of Pt catalyst in a fuel cell MEA can be reduced without sacrificing power.

In addition to achieving high power at low platinum content, fuel cell MEAs (in particular the cathode) must also be highly durable with long operational lifetimes in a FCEV. There are two main cathode catalyst degradation processes in a fuel cell MEA: (i) electrocatalyst (typically Pt metal) dissolution during changes in load, e.g., when the vehicle is idling versus accelerating and (ii) the corrosion of the carbon support during fuel cell start-up and shut down. It has been well-documented that changes from high to low voltage result in degradation of the cathode electrocatalyst.[11–13] Precious metal nanoparticles may coalesce on the carbon support material of Pt and Pt-alloy ORR catalysts via sintering[14,15] or Ostwald ripening,[16,17] with a reduction in surface area and, consequently, a reduction in power in the kinetic region of a polarization curve. after particle growth. Pt islands on the electrocatalyst may also physically detach from the support or dissolve, only to be relocated/redeposited in the ionomer binder or membrane.[12,18] Based on U.S. DOE 2020 targets, the mass activity and electrochemical surface area (ECSA) after

a voltage cycling accelerated stress test for Pt dissolution, should decrease by no more than 40% while the voltage loss at 0.8 A/cm^2 should be less than 30 mV.[4] Pt alloying has proven to be a promising approach to improve electrocatalyst durability. Popov and coworkers studied a PtNi/C gas diffusion electrode in a 0.3 M H_2SO_4 solution before and after long operating times at voltages between 0.4 V and 0.9 V. PtNi catalyst showed negligible metal particle growth after a durability test, while Pt catalyst metal particle diameters increased by 30%.[19] This was attributed to an anchoring effect, where the presence of Ni strengthens the Pt-C bond and hinders sintering of platinum atoms. Similar results were reported by Plasse and coworkers who found that an MEA with a PtCo/C cathode catalyst retained more power than a commercial Pt/C cathode catalyst after a metal dissolution accelerated stress test (AST) where voltage was cycled between 0.87 V and 1.2 V.[20] Notably, neither of these experimental studies employed the metal dissolution AST outline by the DOE, which calls for voltage cycling between 0.6 V and 0.95 V in a gaseous environment. Under the DOE protocols, the durability of alloyed catalyst worsened. Papadias et al. reported on a PtCo/C MEA which exhibited a 40% loss in ECSA and a 60% decrease in oxygen reduction mass activity after 30,000 voltage cycles between 0.6 v and 0.95 V. Analysis of the MEA at end-of-test (EoT) showed thinning of the catalyst layer, increased particle size distribution, and reduced cobalt content in the metal nanoparticles.[21] Similarly, Slack et al. studied the durability of PtCo/C MEAs using electrospun fiber electrodes. After 30,000 cycles of the DOE AST protocol, the authors reported a 15% loss of ECSA and a 20% decrease in ORR mass activity.[10] Unfortunately, neither Papadias nor Slack made a direct comparison to a pure platinum electrocatalyst, making it difficult to conclude if the presence of cobalt aids or hinders durability during the DOE AST protocol.

The durability of the catalyst carbon support is also an issue in automotive fuel cells. After vehicle shut-down, the anode compartment may fill with air. Upon vehicle start-up, a hydrogen/air front is formed in the anode, causing the cathode voltage to spike up to 1.5 V[22], at which point carbon rapidly oxidizes.[23] Oxidation of the carbon support causes a loss in Pt catalyst material, a thinning of the cathode catalyst layer, and a loss in cathode porosity, where the latter leads to O_2 and water mass transport limitations.[24] Partial oxidation of the carbon, with the formation of C-OH and COOH surface species makes the cathode more hydrophilic and prone to flooding.[25] Efforts to improve the stability of the catalyst support have involved the use of non-carbon oxide material supports,[26–28] which are highly stable, but lack the required electrical conductivity and surface area for Pt sites. Tuning the hydrophobicity of the catalyst layer has also proven helpful in minimizing carbon corrosion in a fuel cell cathode. Incorporating a hydrophobic material, such as poly(vinylidene fluoride)[29,30] or polydimethylsiloxane,[31] aids in water removal and, consequently, suppresses the oxidation of carbon support. Rather than solve this problem via new materials development, auto companies employ system-mitigation strategies to minimize corrosion of the support. Examples of these strategies include drawing current from the fuel cell stack during hydrogen introduction to prevent voltage spiking during start-up, keeping the anode compartment filled with hydrogen during shut-down periods to prevent the formation of the hydrogen/air front, and the use of a fuel-recycle loop to prevent local fuel starvation.[32]

An important recent development in the design of fuel cell electrodes has been the use of particle/binder electrospun fibers. It has been shown that fiber mat cathode MEAs produce

higher power at beginning-of-life (BoL) and exhibit improved durability after a metal dissolution or carbon corrosion voltage cycling AST, as compared to a conventional slurry-type electrode MEA with sprayed or coated electrodes.[10,33–35] For example, Brodt et al. showed that electrodes prepared from Pt/C with a binder of Nafion and poly(acrylic acid) (PAA) (where PAA was added to the electrode ink to achieve sufficient chain entanglement for fiber electrospinning) showed 30% higher electrochemically active surface area and 45% higher maximum power versus a conventional spray electrode with neat Nafion binder.[35] After a carbon corrosion AST, the fiber electrode MEA experience a 42% loss in power at 0.65 V whereas the sprayed electrode MEA lost 70%.[35] Interestingly, both the fiber and spray electrode MEAs lost the same amount of carbon after the AST (~17 wt.%), and the improved EoT power for the fiber mat MEA was attributed to interfiber cathode porosity which facilitated rapid water removal thus mitigating cathode flooding. A recent paper by Slack et al.[10] showed very high power output (a maximum power density of 1,043 mW/cm^2) and excellent durability (only a 9% loss in maximum power after a metal dissolution AST) for a PtCo/C:Nafion:PAA fiber cathode MEA, with a cathode loading of 0.1 mg/cm^2. The corresponding metrics for a conventional slurry electrode with the same catalyst and cathode loading are 869 mW/cm^2 maximum power and a 32% loss after the AST. The improvement in initial performance of the fiber electrode MEA was attributed to a higher ECSA and mass activity as well as a lower gas transport resistance (GTR). Improved durability was attributed to the fiber electrode morphology, which allows for a more uniform distribution of catalyst and polymer.

The work presented in this chapter deals with the performance and durability of a commercially available PtNi/C catalyst in an electrospun fiber mat cathode architecture. Fiber cathodes were electrospun using PtNi/C powder and a binder of Nafion + PAA and the resulting MEAs were evaluated in a hydrogen/air fuel cell. The power and durability of PtNi/C fiber cathode MEAs are contrasted with a PtNi/C sprayed cathode MEA using only Nafion as the anode and cathode binder and with data in the literature on Pt/C and PtCo/C fiber cathode MEAs.

3.2 Experimental Materials and Methods

Ketjen carbon-supported Platinum-nickel catalysts with metal contents of 52 wt.% and 22 wt.% (TECNiE52 and TECNiE22, respectively) were acquired from Tanaka Kikinzoku Kogyo (TKK). A 40 wt.% Pt/C catalyst was purchased from Johnson Matthey (HiSPEC 4000). Nafion NR211 membranes, 1100 equivalent weight Nafion ionomer dispersion (LQ-1115), and Sigracet 29 BC gas diffusion layers (GDLs) were purchased from Ion Power Inc. Solvents and 450 kDa poly(acrylic acid) (PAA) were purchased from Sigma Aldrich and used without further purification.

3.2.1 Electrospun fiber and spray electrode preparation

Electrospinning inks were prepared by mixing catalyst powder (either PtNi/C or Pt/C) with acid-form Nafion and PAA in a 3:2 (wt.) water:isopropanol dispersion where the solids content of the ink was 15 wt.%. PtNi/C inks were shear mixed in an ice bath using an Omni THQ homogenizer for 4 hours at 10,000 rpm and then mixed on a stirring plate (magnetic stirring bar) for 72 hours. Pt/C inks were mixed on a magnetic stirring plate for 24 hours. After mixing, inks were electrospun using a single 22-gauge stainless-steel needle spinneret. Fibers were collected on a grounded rotating drum. The electrospinning parameters and dry fiber mat compositions for the

two different catalysts are listed in Table 3.1, where the I/C ratio of fiber electrodes is the ratio of polymer (i.e., Nafion + PAA) to carbon.

Sprayed PtNi/C gas diffusion electrodes (GDEs) were prepared at Nissan Technical Center North America (NTCNA). Catalyst and Nafion ionomer (no PAA) were added to water/alcohol solvent and then mixed using a homogenizer (Ika T25) for 4 hours. An electrocatalyst cathode layer was formed on a gas diffusion layer (GDL) using an automated robotic spray system (Asymtek, Nordson). The polymer to carbon ratio (I/C ratio) for all sprayed PtNi/C inks was ~1.2:1 corresponding to catalyst:ionomer weight ratios of 63:37 and 52:48 for the 52% and 22% PtNi/C electrodes, respectively.

3.2.2 Membrane-electrode-assembly (MEA) preparation

Catalyst-coated membranes (CCMs) using fiber electrodes with a geometric electrode footprint of either 5 cm^2 or 10 cm^2 were prepared by hot-pressing a PtNi/C fiber mat cathode and a Pt/C fiber anode onto the opposing surfaces of a Nafion 211 membrane at 140 °C and 4 MPa for 5 minutes. Both PtNi/C and Pt/C electrode loadings were 0.1 mg_{Pt}/cm^2. Sigracet 29 BC carbon paper gas diffusion layers were pressed onto the anode and cathode when the CCM was loaded into the fuel cell test fixture.

Spray GDE electrode MEAs with an electrode area 10 cm^2 were prepared at NTCNA, where the PtNi/C cathodes loading was 0.1 mg_{Pt}/cm^2. Commercial Pt/C GDEs from Johnson Matthey at 0.4 mg_{Pt}/cm^2 were used as anodes. MEAs were prepared by hot-pressing anode and cathode GDEs to a Nafion 211 at 2 MPa and 130 °C for 10 minutes.

Table 3.1: Dry mat compositions and electrospinning conditions for fiber electrodes

Catalyst Type and Composition	52% PtNi/C	22% PtNi/C	40% Pt/C
Catalyst:Nafion:PAA (dry wt.)	65:23:12	51:27:22	65:20:15
Solids content of the ink* (wt. %)	15	15	12
I/C ratio (wt.:wt.)**	1.12	1.23	0.90
Potential (kV)	7.5	9	12
Relative Humidity (%)	30	21	40
Flow Rate (ml/h)	0.6	1	0.75
Needle to Collector Distance (cm)	11	9	8

*Solids content refers to the weight % of catalyst + Nafion + PAA in the ink

** I/C ratio refers to the weight ratio between polymer binder (Nafion + PAA) to carbon

3.2.3 Structural characterization of electrodes

Top-down and cross-sectional scanning electron micrographs of fiber electrode MEAs were collected using a Zeiss Merlin SEM. MEA cross-sectional samples were prepared for imaging via freeze fracturing. Electrode structure and composition were also studied by scanning transmission electron microscopy (STEM), and energy dispersive x-ray analysis (EDX) using a Tecnai Osiris S/TEM at Oak Ridge National Laboratory and a single-tilt aluminum holder. STEM samples were embedded in epoxy and cut to a thickness between 50-100 nm using a Leica EM UC7 microtome at Oak Ridge National Laboratory. Slices of embedded sample were placed onto TEM copper grids. For both SEM and STEM samples, the gas diffusion carbon paper was removed from both the anode and cathode side of the MEAs.

3.2.4 Fuel cell testing and electrochemical analysis

Fiber electrode MEAs were evaluated using a Scribner 850e test station and a Fuel Cell Technologies Inc. test fixture with single serpentine flow fields and a 5 cm^2 active electrode area. Polarization data were collected at 80 °C, 200 kPa_{abs}, and 125/500 sccm H_2/air at the anode and cathode, respectively. Fiber and spray electrode MEAs were evaluated at NTCNA using a 10 cm^2 test fixture with parallel flow fields. Polarization data were collected at 80 °C and 200 kPa_{abs}, with H_2/air supplied at 4000/8000 sccm.

The oxygen reduction reaction mass activity (corrected for H_2 cross-over and iR overpotential) at 0.9 V were determined at 80°C, 150 kPa_{abs}, and 100% relative humidity (RH), with H_2/O_2 flow rates of 100/100 sccm, based on methods described in literature.[36] Electrochemically active surface area (ECSA) was calculated from cyclic voltammograms (CVs) at 30 °C, 100 kPa_{abs}, and 100% RH using an external potentiostat (Gamry Reference 3000).[37]

Two different AST durability experiments were conducted. The first was a metal dissolution AST where repeated high and low load operation was simulated by square-wave voltage cycling from 0.60 V to 0.95 V (3 seconds at each voltage, 30,000 cycles) at 80 °C, 100 kPa_{abs}, with H_2 fed to the anode and N_2 gas to the cathode. A carbon corrosion AST was also carried out, where repeated fuel cell start-up and shut-down were simulated by triangular-wave voltage cycling from 1.0 V to 1.5 V at a rate of 500 mV/s for 1,000 cycles at 80 °C, 100 kPa_{abs}, under H_2/N_2.[4,38] During the carbon corrosion AST, the CO_2 concentration of the cathode air exhaust was recorded using a CO2Meter CM-152 solid-state sensor.

The gas transport resistance (GTR) in fiber and sprayed cathodes was determined by measuring the ORR limiting current at different oxygen feed concentrations (0.000%, 0.525%, 0.787%, 1.838% and 2.625% O_2 with the balance being N_2) and different total pressures (100, 150, 200, and 250 kPa_{abs}). Data were collected at 80 °C and 90% RH with anode/cathode feed gas flowrates of 4000/8000 sccm, respectively, following the procedure described in the literature.[10,39]

The proton transport resistance of the cathode catalyst ionomer ($R_{ionomer}$) in an MEA was determined via electrochemical impedance spectroscopy (EIS). Measurements were performed at 0.45 V (DC) with frequencies varying from 15 kHz to 0.1 Hz and an AC amplitude of 10 mV. The fuel cell test fixture was operated at 80 °C and 100% RH with H_2 and N_2 supplied to the anode and cathode, respectively, at 500 sccm. An in-depth description of the procedure and method of data analysis for this set of experiments can be found in reference 10.

3.3 Results and discussion

3.3.1 Analysis of PtNi/C fiber structure

Top-down SEM images of an as-spun fiber mat with 52 wt.% PtNi/C are shown in Figures 3.1a and 3.1b. The images show a mat free of spray droplet defects with a fiber diameter in the 400-800 nm range. The surface of the fibers is highly roughened, with catalyst well distributed at the fiber surface in the fiber length direction. These fibers are similar in appearance to both PtCo/C and Pt/C fibers prepared with a Nafion/PAA binder as reported in the literature[10,34,35] as well as Pt/C fibers (Figures 3.1e and 3.1f). Figures 3.1c and 3.1d show a PtNi/C fiber electrode after an initial

(beginning-of-life, BoL) polarization experiment and after measuring the initial ECSA, and ORR mass activity. The fiber structure after these experiments is the same as that of an as-spun mat.

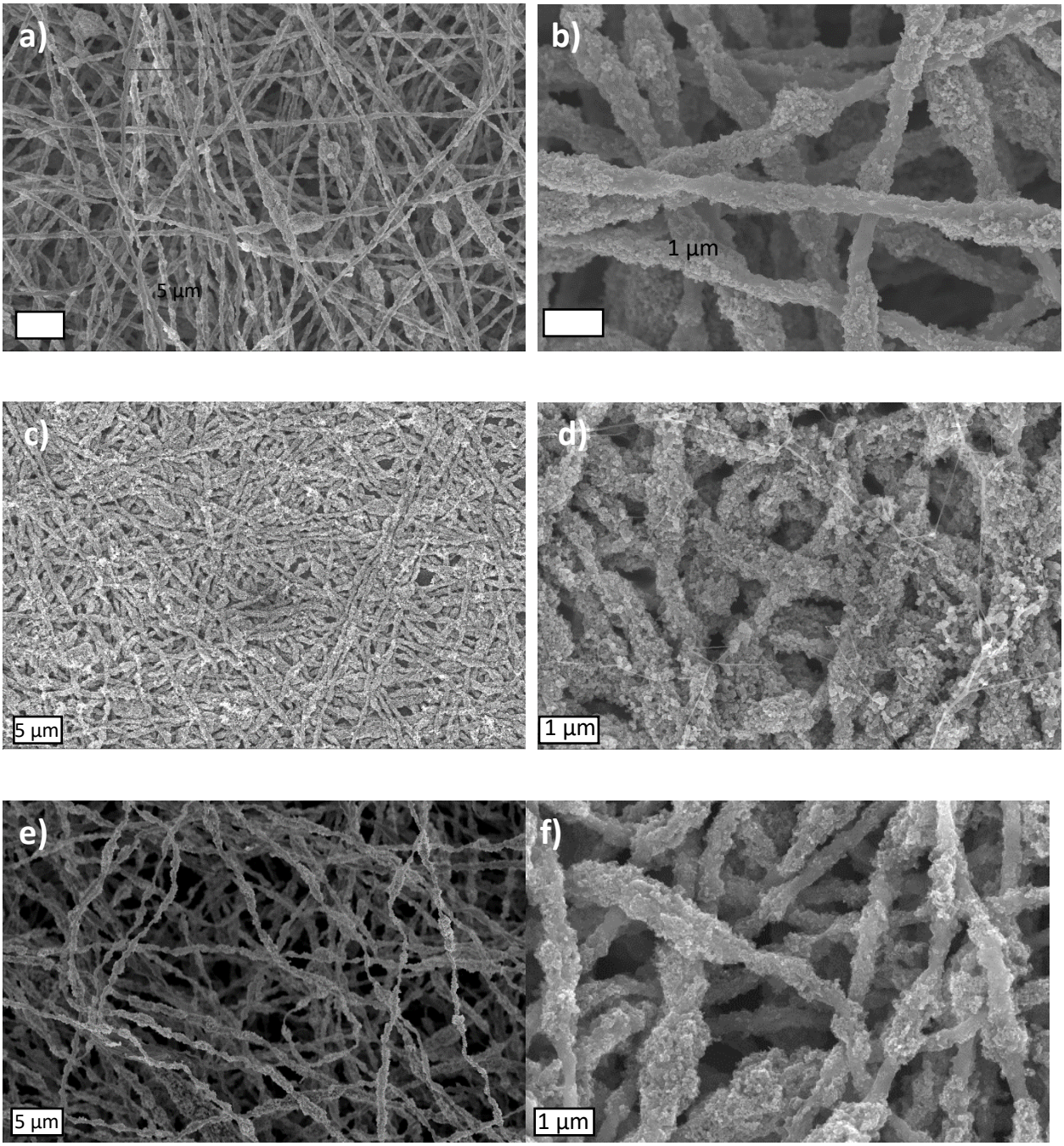

Figure 3.1: (a-d) Top-down SEM images of 52% PtNi/C fiber cathodes (a and b) before and (c and d) after BoL experiments. (e,f) Top-down SEM images of Pt/C fiber cathodes before fuel cell

testing. Magnification was (a, c, and e) 5,000x and (b, d, and f) 30,000x. Both catalysts were spun with a binder of H^+ -Nafion and PAA.

After BoL assessment (i.e., the collection of i-V polarization data, ECSA, and ORR mass activity), PtNi/C MEAs were prepared for analysis via STEM. As can be seen in the elemental maps of fiber cross sections in Figure 3.2, the PtNi/C fibers have an ionomer-rich surface and a catalyst-enriched interior. In a prior publication by Slack et al.,[10] fibers with PtCo/C catalyst and H^+-Nafion/PAA binder did not show the Nafion surface enrichment seen in Figure 3.2. Upon further inspection of cross-sectional images from that PtCo/C study, it was found that the majority of the fibers did indeed show ionomer surface enrichment, consistent with the fibers shown in Figure 3.2a. An intrafiber porosity of 12% was determined from STEM high-angle annular dark-field (HAADF) images, which is in contrast to a Pt/C fiber with the same binder where the internal porosity was 6%. ImageJ analysis of the pore size distribution for 8 individual fiber cross sections (Figure 3.3) show that the PtNi/C fibers had substantially more pores with a radius smaller than 0.75 nm, as compared to an electrospun fiber mat with Pt/C and the same binder. Notably the trends in Figure 3.3 are similar to those observed by Slack et al. who showed that a PtCo/C fiber electrode spun from a binder of Na^+-Nafion-polyethylene oxide (PEO) (where the PEO could be washed out of the final fiber mat) had Intrafiber pores of a smaller radius than a PtCo/C fiber electrode spun from a binder of H^+-Nafion-PAA.[40] Although Slack does not discuss why the Nafion/PEO fibers had smaller pores, it may be due to the voids created by the removal of PEO. If this is true, then one may speculate that in the case of PtNi/C fibers spun from H^+-Nafion/PAA some/all of the carrier polymer can be removed, resulting in smaller pores.

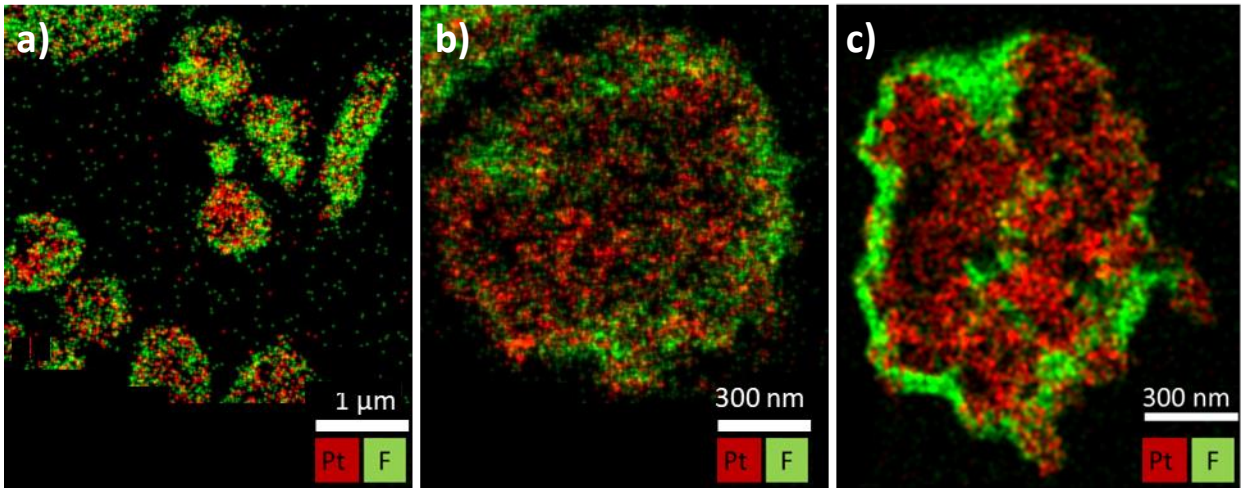

Figure 3.2: Elemental maps of 52% PtNi/C:H$^+$-Nafion:PAA fiber electrode cross-sections at (a) 14,000x and (b) 56,000x magnifications, and (c) 50% Pt/C:H$^+$-Nafion:PAA fiber electrode cross-section at 56,000x magnification. Red represents platinum (catalyst), and green represents fluorine (ionomer).

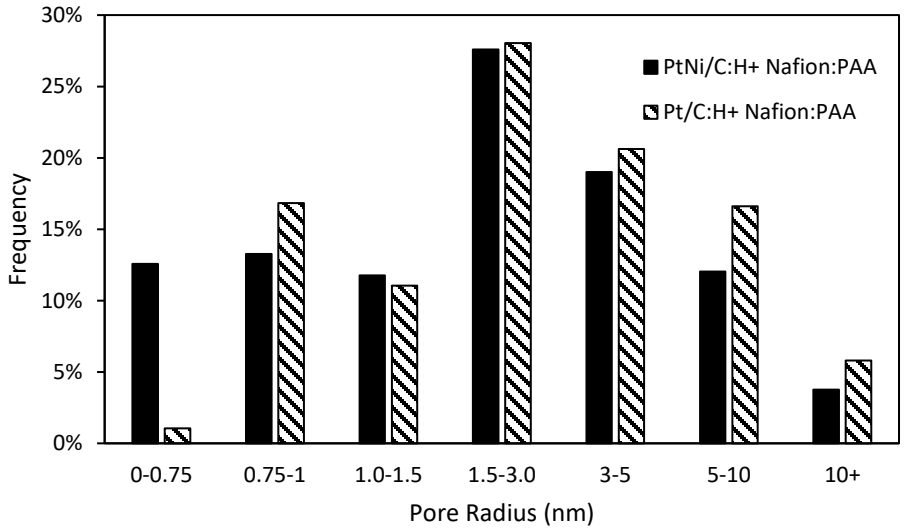

Figure 3.3: Intrafiber pore-size distribution of (solid) 52% PtNi/C:H$^+$-Nafion:PAA fibers and (striped) Pt/C:H$^+$-Nafion:PAA fibers.

3.3.2 BoL Fuel Cell Performance

Fuel cell polarization data for a fiber cathode MEA with 52% PtNi/C were collected at Nissan Technical Center North America (NTCNA). A representative polarization curve is contrasted with that from a sprayed PtNi/C electrode in Figure 3.4a. An improvement in power of ~20% was found, where peak power densities of fiber (with a binder of Nafion:PAA) and spray (with a binder of neat Nafion) MEAs were 990 and 810 mW/cm^2, respectively. This power density improvement is in good agreement with published data in the literature, e.g., a 20% improvement in the maximum power for a PtCo/C fiber cathode MEA with H^+-Nafion/PAA binder versus a PtCo/C sprayed cathode MEA with neat Nafion binder.[10] As listed in Table 3.2, the measured ECSA and mass activity for PtNi/C fiber cathodes were greater than those for sprayed electrodes with neat Nafion binder, presumably due to the high interfiber and intrafiber porosity and fewer catalyst particle and ionomer binder agglomerates, leading to improved access to catalyst sites and lowered ORR activation overpotentials. Fibers also showed lower ionomer resistance and a lower O_2 GTR compared to sprayed electrodes (cathodes), likely due to the highly uniform distribution of ionomer along the length of the fibers and a highly accessible electrochemical surface area, respectively.

Figure 3.4b compares nanofiber electrode MEAs where PtNi/C, PtCo/C or Pt/C is used as the ORR catalyst in fiber mat cathode MEAs (all MEAs with the same Nafion/PAA binder). As expected, both Pt-alloy catalyst MEAs produced higher power than the Pt/C MEA. The improved performance is attributed to the higher ORR catalytic activity of alloyed catalysts, where activities of 266 and 270 mA/mg$_{Pt}$,[10] were measured for PtNi/C and PtCo/C, respectively, whereas the activity of Pt/C was only 160 mA/mg$_{Pt}$ as is listed in Table 3.2.[29] Although all three catalyst types

had a similar ECSA in the fiber morphology (~45 m^2/g_{Pt}), alloyed catalysts have intrinsically higher oxygen reduction activity due to compressive lattice strain imposed by the transition metals. Interestingly, although the PtNi/C fiber MEA performed almost identically to the PtCo/C fiber MEA in terms of polarization performance, activity, and O_2 GTR, the two catalysts seem to vary significantly with respect to ionomer resistance. Both PtNi/C spray and fiber MEAs have an ionomer resistance about 40% higher than that of their PtCo/C analogs. This may be due to leached nickel ions exchanging with protons at the sulfonic acid sites of Nafion which has been shown to hinder performance if the MEA is not acid-washed prior to testing.[41]

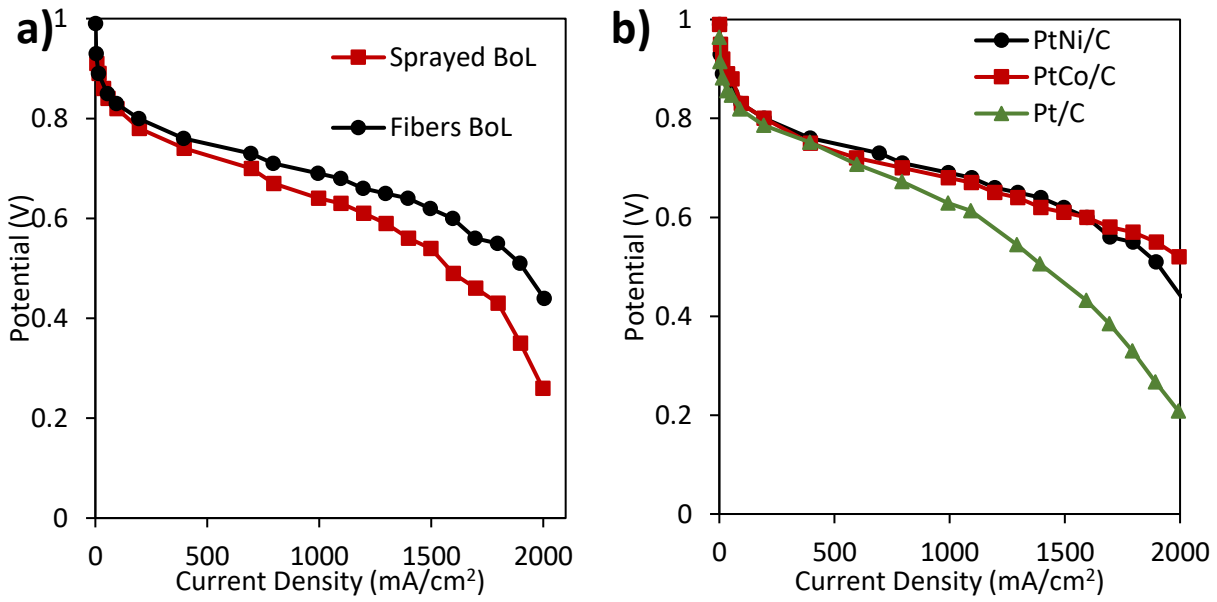

Figure 3.4: (a) Polarization data for a (red squares) PtNi/C:H^+-Nafion spray electrode MEA and a (black circles) 52% PtNi/C:H^+-Nafion:PAA fiber electrode MEA. (b) Polarization curves for fiber electrode MEAs with a binder of H^+-Nafion:PAA with a cathode catalyst of (black circles) 52% PtNi/C, (red squares) PtCo/C,[10] or (green triangles) Pt/C.[36] Data were collected at NTCNA at 100% RH, 200 kPa_{abs}, 80 °C, with H_2/air flowrates of 4000/8000 sccm.

Table 3.2 also compares the electrodes prepared in this work to those in the literature. A non-fibrous de-alloyed PtNi/C cathode MEA (prepared at the Johnson Matthey Technology Centre) had ~20% higher ECSA and nearly double the mass activity of the fiber PtNi/C cathode MEAs prepared for this study.[42] Despite an appreciably lower ORR activity, the fiber MEA gave higher power at 0.65 V and at maximum power versus the Johnson Matthey electrode. Notably, at 0.65V and 100% RH conditions, the fiber electrode had an HFR of 0.05 $m\Omega \cdot cm^2$ while the Johnson Matthey electrode had an HFR of 0.1 $m\Omega \cdot cm^2$. It is unclear why the membrane ohmic loss was double in the Johnson Matthey MEA compared to the fiber electrode MEA which both used 25 μm thick membranes and had a similar catalyst:polymer weight ratios, but the discrepancy may explain why use of a more active catalyst did not translate to a higher power. Fortunately, electrospinning is a technique that has been used successfully to prepare fiber mat electrodes with many different catalysts, suggesting that use of the Johnson Matthey PtNi/C material in a fiber morphology could lead to higher power.

The final row of data in Table 3.2 refers to a PtCo/C fiber cathode MEA which was spun from a binder of Na^+-form Nafion and poly(ethylene oxide) (PEO). The PEO carrier polymer was washed out of the MEA, so the binder during fuel cell operation was neat Nafion.

Table 3.2: BoL performance metrics for 52% PtNi/C spray and fiber cathode MEAs, as compared to MEAs from the literature prepared with binders, morphologies, and cathode catalysts.

Cathode Material	ECSA m^2/g_{Pt}	Mass Activity mA/mg_{Pt}	Power at 0.65 V mW/cm^2	Maximum Power mW/cm^2	O_2 Transport Resistance s/m	$R_{ionomer}$ $\Omega \cdot cm^2$
52% PtNi/C Sprayed	40	221	605	809	48	0.31
52% PtNi/C Fibers	46	266	842	988	39	0.25
52% PtCo/C Fibers (H^+-Nafion/PAA)[10]	48	270	777	1043	35	0.14
Pt/C Fibers (H^+-Nafion/PAA)[35]	64	n/a	580	704	n/a	n/a
35% PtNi/C[42]	54	530	812	878	n/a	n/a
52% PtCo/C Fibers (Na^+-Nafion/PEO)[40]	69	350	910	1150	n/a	n/a

The 22 wt.% PtNi/C catalyst in fiber mat or sprayed cathodes with Nafion/PAA performed essentially the same as a 52% PtNi/C cathode at operating voltages below 0.65 V, as can be seen in the polarization data of Figure 3.5. In the low voltage region of the fuel cell polarization curves, the 22 wt.% catalyst cathodes (sprayed and fibers) showed more mass transfer resistance (~20% lower power), a consequence of the thicker cathodes when the lower Pt content catalyst powder was used. Additionally, ORR activity and O_2 GTR were comparable between the two catalysts (see Table 3.3). Because of the similarity in performance, the remaining experiments were carried out using the 52% PtNi/C.

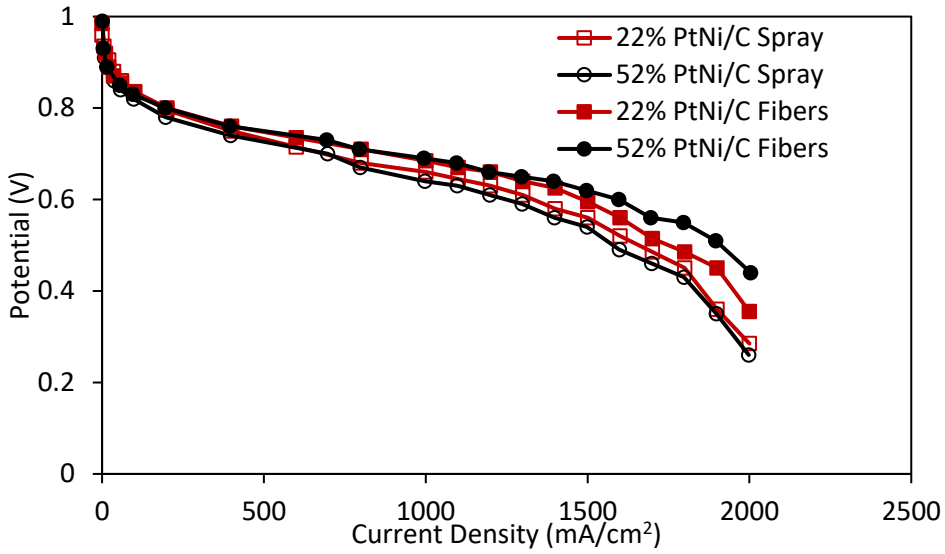

Figure 3.5: Polarization data for (red squares) 22 wt.% PtNi/C and (black circles) 52 wt.% PtNi/C cathode MEAs in the (open) sprayed and (filled) fiber electrode morphologies. Data were collected at NTCNA at 100% RH, 200 kPa_{abs}, 80 °C, with H_2/air flowrates of 4000/8000 sccm.

Table 3.3: BoL performance metrics for 22% PtNi/C spray and fiber cathode MEAs

22% PtNi/C	Mass Activity (mA/mg_{Pt})	Power at 0.65 V (mW/cm^2)	Maximum Power (mW/cm^2)	O_2 Transport Resistance (s/m)
PtNi/C Sprayed	211	707	840	51
PtNi/C Fibers	248	833	896	39

3.3.3 Low humidity performance of PtNi/C fiber cathode MEAs

Polarization data at 100% RH and 40% RH for PtNi/C fiber MEAs are shown in Figure 3.6a. Maximum power density is plotted as a function of humidity in Figure 3.6b. The PtNi/C data is averaged over 6 different MEAs and compared to PtCo/C fiber MEAs (with the same binder).[40] It is evident from the data that PtNi/C fiber cathode MEA performance is less dependent on

humidity than a PtCo/C fiber cathode MEA. Fiber electrodes prepared with acid-form Nafion and PAA using either PtCo/C or Pt/C have both shown a significant power loss at 40% RH as compared to the power generated under full humidification.[10,43] The low humidity performance of PtNi/C:H^+-Nafion:PAA cathode MEAs more closely resembles the performance of PtCo/C fiber electrodes prepared with a binder of Na^+-Nafion:PEO (the dashed line in Figure 3.6b).[40] In the Nafion/PEO system, carrier polymer washes out of the electrode during operation, resulting in an increased number of small pores in a fiber (radius < 3 nm) and higher intrafiber porosity. It has been hypothesized that the presence of small radius pores in the electrode fibers may facilitate capillary condensation at low humidity, resulting in improved proton conductivity and performance.[41] Past publications have shown that PAA cannot be removed from a fiber electrode spun with Nafion in the acid form due to strong Nafion/PAA interactions.[43] Exchanging the protons at the sulfonic acid sites of Nafion with Na^+ may weaken this interaction, allowing for the removal of the PAA carrier polymer. It is possible that, when using PtNi/C catalyst, leached nickel may ion exchange with the acid sites of either Nafion or PAA during ink mixing, weakening the Nafion/PAA interaction and allowing for at least partial removal of PAA during fuel cell operation. The high intrafiber porosity (12% in PtNi/C fibers vs. 6% in Pt/C fibers), the increased number of small pores in the PtNi/C fibers, and the high performance of PtNi/C fibers at low humidity support this hypothesis. High performance at low humidity has not been observed in other systems using PtNi/C. The data collected on the Johnson Matthey PtNi/C cathode MEA by Xin et al., represented by the triangle markers in Figure 3.6b, show a severe drop in power when the humidity decreased from 85% to 55% RH which is in-line with the assumption that intrafiber porosity lessens humidity dependence.[42]

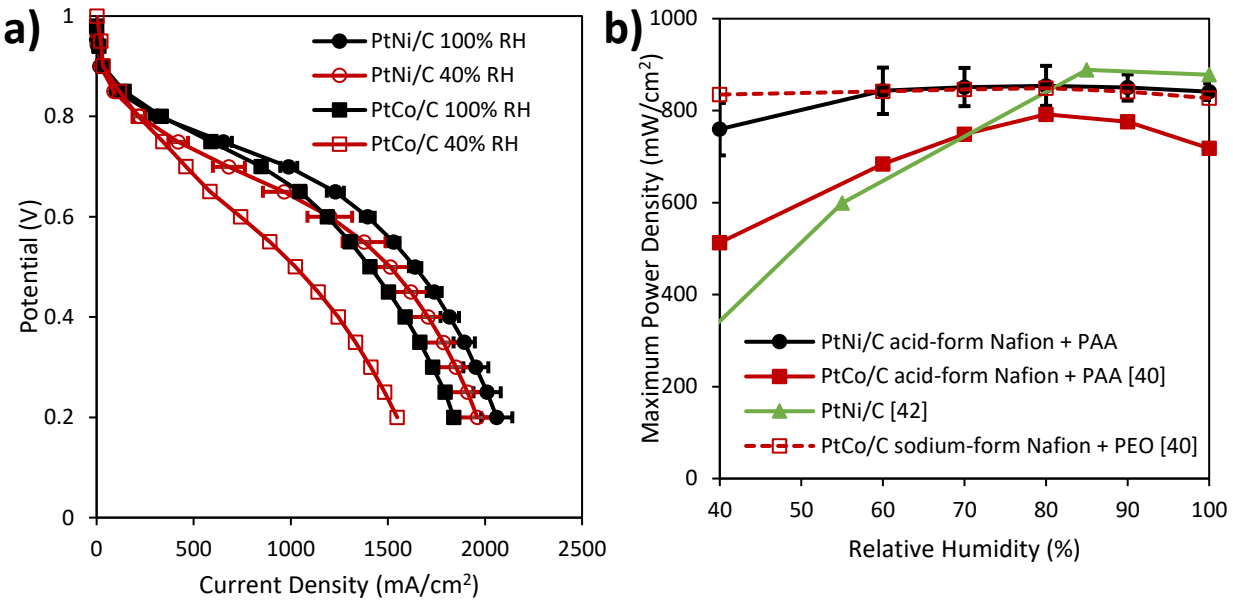

Figure 3.6: (a) Polarization data for fiber electrode MEAs prepared with (circles) PtNi/C and (squares) PtCo/C cathode catalyst at (filled) 100% RH and (open) 40% RH. (b) Maximum power density versus relative humidity for fiber electrode MEAs prepared with (circles) fiber PtNi/C cathodes with acid-form Nafion + PAA binder, (filled squares) fiber PtCo/C cathodes with acid-form Nafion + PAA binder,[40] (open squares) fiber PtCo/C cathodes prepared from a sodium-form Nafion + PEO binder, [40] and (triangles) slurry PtNi/C cathodes with a neat Nafion binder.[42]

3.3.4 Metal dissolution AST

Polarization curves for sprayed and fiber PtNi/C electrode MEAs before and after 30,000 metal dissolution voltage cycles are plotted in Figure 3.7. Similar to other reports in the literature, the fiber morphology led to improved retention of power at end-of-test (EoT), as compared to sprayed electrodes.[10,35] Peak power only decreased by 7% for the PtNi/C fiber cathode MEA, whereas the maximum power density for a sprayed electrode MEA dropped by 19%, as shown in Table 3.4. Interestingly, both sprayed and fiber electrode MEAs lost 15% of their initial ECSA, but

the sprayed MEA lost appreciably more catalytic activity. While leaching of the transition metal could result in lower activity,[21] a loss of Pt surface area is also expected during this AST.[14] The loss of Ni and change in PtNi particle size in fiber mat and sprayed electrode cathodes at EoT, as determined from elemental analysis and STEM images, is shown in Figure 3.8(a and b). These measurements were collected as is described in the literatue.[10] The results reveal that neither the sprayed nor fiber electrode MEAs lost appreciable amounts of transition metal after the AST (Figure 3.8a), with similar particle growth for the two cathode morphologies (Figure 3.8b). Instead, this loss in activity may arise from migration of nickel from the outer layers of the catalyst to the core. Elemental analysis of individual catalyst particles from EDS maps of fiber cross-sections revealed that the concentration of nickel in the particle center relative to the whole particle increased for both electrode morphologies after 30,000 metal dissolution cycles. Metal particles in a fiber electrode at BoL had 3.6 at.% higher nickel content in the core compared to the entire particle, and at EoT, the nickel content increased to 5.7%. Metal particles in the sprayed electrode had 2.3 at.% higher Ni content in the particle center relative to the entire particle, but at EoT this value increased to 6.3 at.%. It has been shown by Oezaslan et al. that if the transition metal is concentrated in the core, then the benefits of alloying are diminished.[44] The present AST results are in contrast to PtCo/C fibers, where Co content was reduced by 5% after the AST, but ORR mass activity only decreased by 19%.[10]

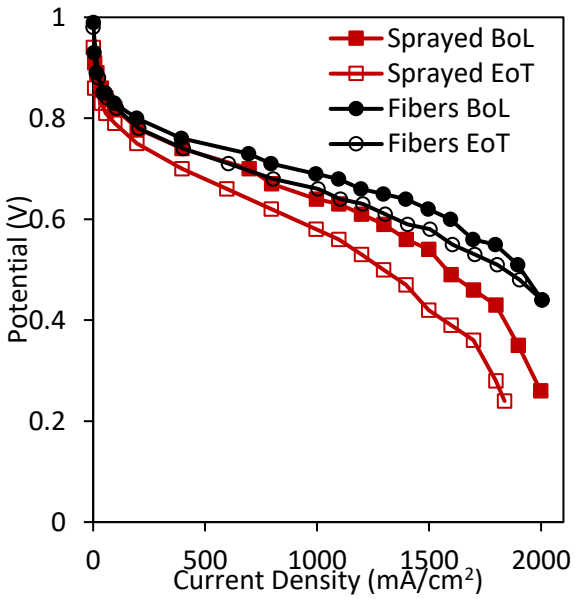

Figure 3.7: (filled) BoL and (open) EoT polarization curves for PtNi/C (red squares) sprayed and (black circles) fiber cathode MEAs. Data were collected at NTCNA at 100% RH, 200 kPa_{abs}, 80 °C, with H_2/air flowrates of 4000/8000 sccm. EoT is defined at 30,000 metal dissolution cycles.

Table 3.4: Performance metrics for PtNi/C sprayed and fiber cathode MEAs after 30,000 metal dissolution cycles compared to a PtCo/C fiber cathode MEA.[10]

	ECSA m^2/g_{Pt}		Mass Activity mA/mg_{Pt}		Maximum Power mW/cm^2		Power at 0.65 V mW/cm^2	
	BoL	EoT	BoL	EoT	BoL	EoT	BoL	EoT
PtNi/C Sprayed	40	34	221	136	809	656	605	419
PtNi/C Fibers	46	39	266	202	987	920	842	685
PtCo/C Fibers[10]	48	41	270	219	1043	952	777	646

It should also be noted that BoL Ni content in both fiber and spray electrodes was much lower than the theoretical value of 28 atomic%, with less Ni in the metal catalyst particles of a fiber cathode versus a sprayed cathode. This is associated with nickel leaching during ink preparation. The mixing time for PtNi/C powder with poly(acrylic acid) and Nafion was 3 days for an electrospinning ink, but only 24 hours for Pt/C and PtCo/C based inks (for spraying or electrospinning).[10,35] This extended mixing time may have allowed more of the Ni to leach from the catalyst. Examinations of shorter mixing times and the effects of mixing with neat Nafion versus Nafion + PAA are warranted. Leached nickel may displace the protons at the sulfonic acid sites of Nafion.[45] If this is the case, the migration of protons from the anode to cathode during fuel cell operation would displace any divalent nickel ions, with the later exiting the fuel cell via water droplets in the air exhaust. Examination of the elemental composition of the exhaust may provide useful insights into the mechanism through which nickel is lost.

Figure 3.9 shows changes in O_2 GTR and cathode ionomer resistance ($R_{ionomer}$) at BoL and EoT for: (i) a sprayed cathode MEA with PtNi/C and neat Nafion binder, (ii) PtNi/C fibers with Nafion + PAA binder, and (iii) PtCo/C the fibers with Nafion + PAA binder.[10] Both the GTR and $R_{ionomer}$ were lower for the PtNi/C fiber cathode than a sprayed cathode by ~20%. These results are consistent with prior studies by Slack et al. who attributed the lower GTR of fiber electrodes to the higher electrode surface area and the lower $R_{ionomer}$ to the reduction of catalyst and binder agglomerates. For presumably the same reasons, GTR and ionomer resistance of the PtNi/C fiber electrode at EoT were lower than those for the spray electrode. These findings are in good agreement with the polarization data where voltage losses at BoL and EoT are less for the fiber

electrode than the spray in both the ohmic range (relating to $R_{ionomer}$) and the high current density range (relating to GTR).

Comparing PtNi/C and PtCo/C fiber mats, both GTR and $R_{ionomer}$ were higher in the PtNi/C fiber cathode versus the PtCo/C fiber MEA at both BoL and EoT. This is possibly due to the differences in Pt roughness factor (the product of ECSA and platinum loading) which is inversely proportional to GTR.[46] As the PtCo/C fibers had a higher ECSA than the PtNi/C fiber at both BoL and EoT, it is reasonable that the GTR would be lower for PtCo/C electrodes. The increase in $R_{ionomer}$ at EoT, however, was only 16% in PtNi/C fibers and 32% in PtCo/C fibers. This may be because during the AST, the PtCo/C catalyst lost a higher percentage of its transition metal versus the PtNi/C catalyst. During the AST, metal particles may redeposit in the polymeric binder which is known to lower proton conductivity.[47] Therefore, the greater amount of leached transition metal during the AST in the PtCo system as compared to the PtNi system is likely the reason for the greater percent increase in $R_{ionomer}$.

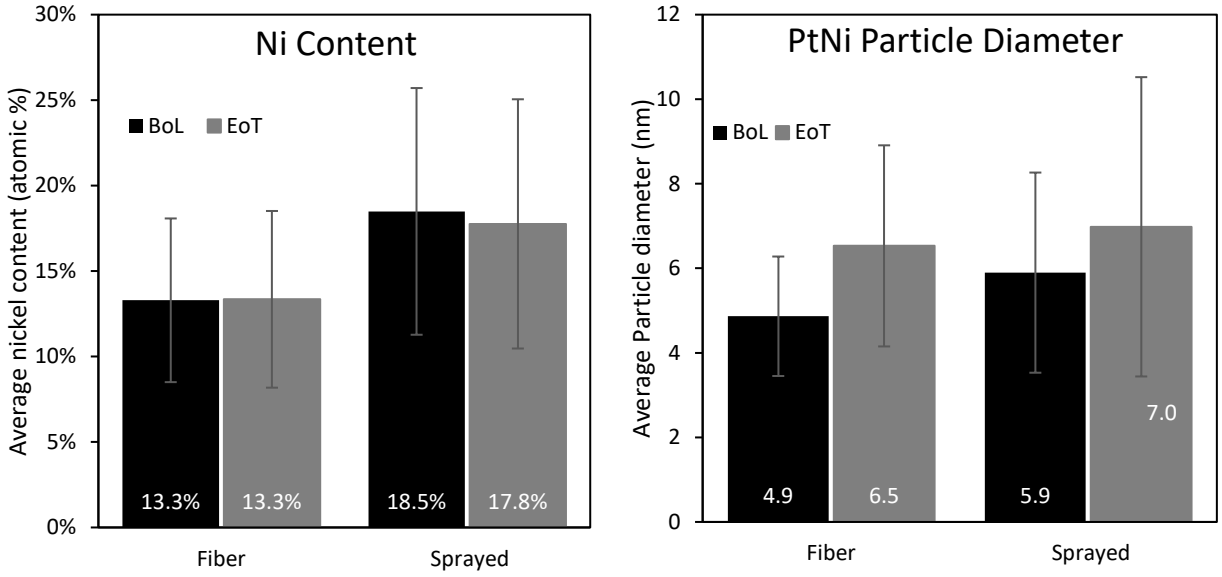

Figure 3.8: (a) Average nickel content in a given metal nanoparticle and (b) average metal nanoparticle diameter at (black) BoL and (grey) after 30,000 metal dissolution cycles (EoT) for PtNi/C sprayed and fiber cathode MEAs.

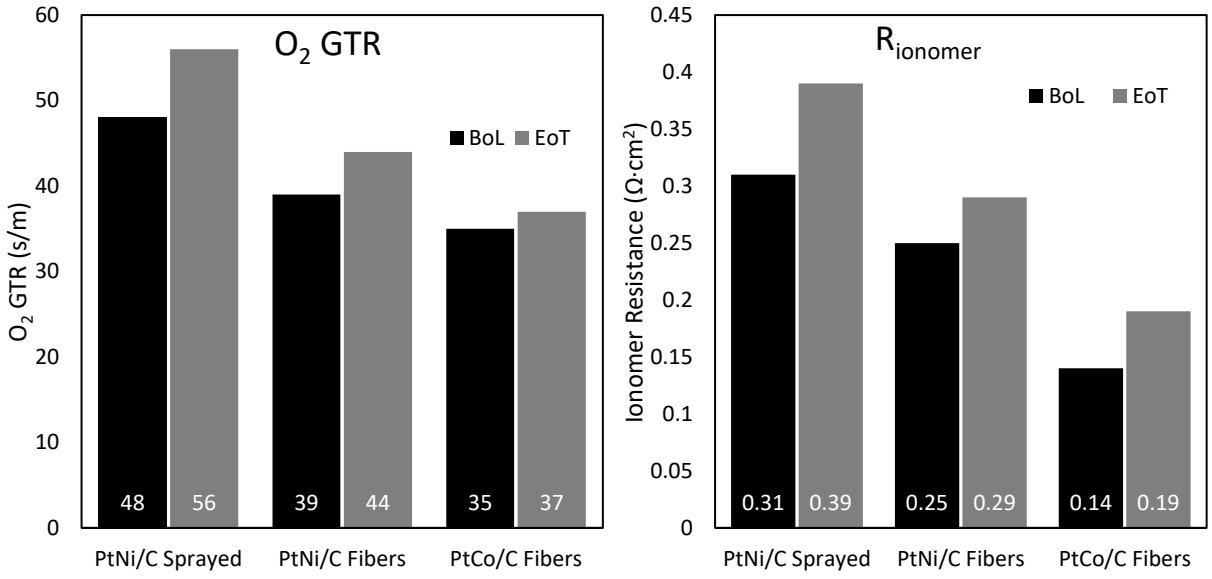

Figure 3.9: (a) O_2 GTR and (b) $R_{ionomer}$ at (black) BoL and (grey) after 30,000 metal dissolution cycles (EoT) for PtNi/C sprayed, PtNi/C fiber, and PtCo/C[10] fiber cathode MEAs.

3.3.5 Carbon corrosion AST

A standard carbon corrosion voltage cycling durability test was carried out on PtNi/C fiber mat cathodes with a H^+-Nafion/PAA binder. The polarization data in Figure 3.10 show a significant drop in power after 1,000 voltage cycles (triangular wave between 1.0 V and 1.5 V). The steep downturn in the EoT V-i curve at high current densities is indicative of electrode flooding. Flooding is a common occurrence after carbon corrosion due to thinning of the electrode, a decrease in electrode porosity, and hydrophilization of carbon support surface.[24] Indeed, SEM analyses of fiber mat MEA cross-sections at BoL and EoT revealed that cathode thickness decreased by 69%, from 3.2 µm to 1.0 µm (see Figure 3.11). It was determined that 22% of the initial mass of carbon support was lost from the fiber cathode, based on the measurement of CO_2 in the cathode exhaust during the AST experiment. For comparison, a fiber cathode MEA with Pt/C catalyst (and a Nafion/PAA binder) lost less carbon (15%), with a smaller reduction in cathode thickness (63%).[30] In that study, the cathode catalyst was platinum supported on Vulcan carbon, whereas the PtNi alloy used in the present tests was supported on Ketjen carbon, which is known to be more susceptible to oxidation, thus explaining the more severe carbon loss and cathode thinning for the PtNi/C MEA.[48,49] However, carbon type alone does not explain the severe power loss after the AST (e.g., a 60% power drop at 0.65 V), which is considerably more pronounced than that found in a 2017 study with PtCo supported on Ketjen carbon (a power loss of only 36% at EoT).[50] At this time, it is unclear why PtNi decorated on carbon is less durable than catalysts where carbon is decorated with Pt or PtCo. However, system strategies designed to mitigate carbon oxidation during fuel cell shut down and start-up may allow for the use of PtNi/C in an automotive fuel cell despite its poor carbon support durability.[32]

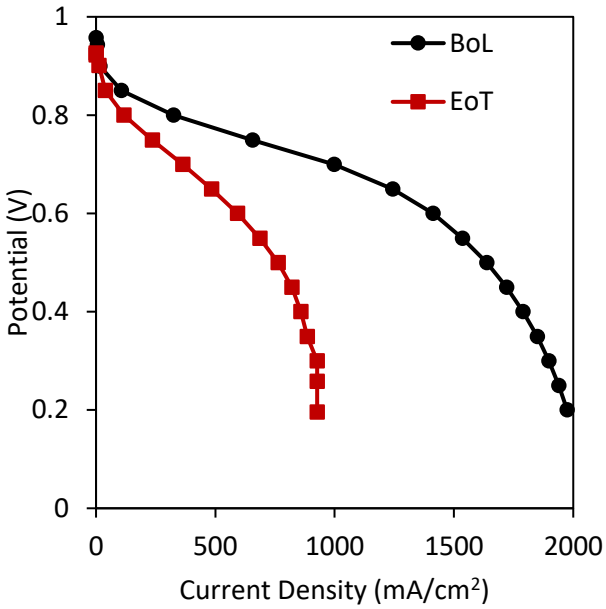

Figure 3.10: Polarization data for a PtNi/C:Nafion:PAA fiber cathode MEA at (black circles) BoL and (red squares) after 1,000 carbon corrosion cycles. Data were collected at Vanderbilt University and the operating conditions were 80 °C, 200 kPa_{abs}, 100% RH, and H_2/air flowrates of 125/500 sccm.

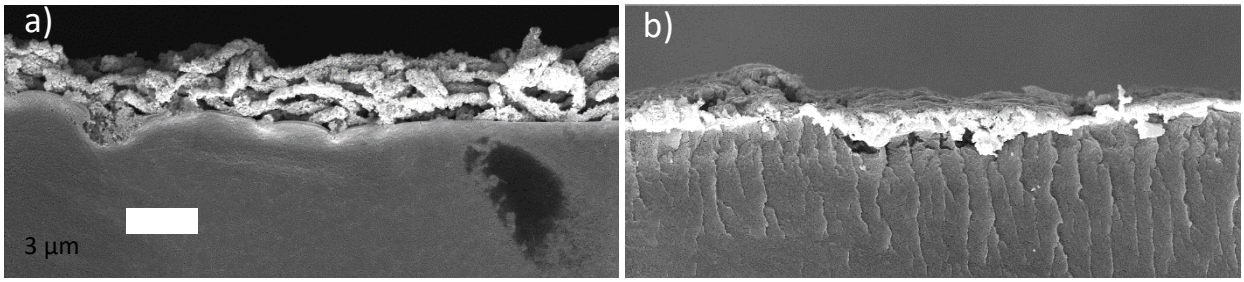

Figure 3.11: Cross-sectional SEMs of PtNi/C fiber cathodes at (a) BoL and (b) EoT. Images were collected at 10,000X magnification.

3.4 Conclusions

PtNi/C fiber mat cathodes were successfully produced via electrospinning. In a fuel cell, the PtNi/C fiber cathode MEAs exhibited excellent performance, producing up to 30% higher power than a PtNi/C sprayed cathode MEA and reaching a peak power of 988 mW/cm^2 at 80 °C, 100% RH, and 200 kPa$_{abs}$ under H_2/air. Improved performance is attributed to a uniform distribution of ionomer and catalyst as well as the high inter and intrafiber porosity which increased ECSA and ORR mass activity and decreased ohmic and gas transport resistances in the cathode. Performance of the PtNi/C fiber MEA at 100% RH and BoL closely aligned with that of a PtCo/C fiber MEA in terms of power, activity, ECSA, and O_2 GTR. Two key differences between the two catalysts were catalyst layer ionomer resistance, which was higher for PtNi/C, and transition metal content in the catalyst powder which was lower for PtNi/C. These data suggested that Ni was leached from the catalyst and contaminated the ionomer during ink preparation. Fiber cathode MEAs prepared from PtNi/C catalyst produced significantly higher power (760 mW/cm^2) at low humidity (40% RH) than a PtCo/C fiber cathode MEA (513 mW/cm^2) despite similar performance between the two catalyst types at 100% RH. This is possibly due to high porosity and the presence of small radius intrafiber pores which may aid in MEA hydration via capillary condensation. The metal content of the PtNi/C catalyst had little effect on MEA performance, where power, ORR activity, and O_2 GTR were similar between MEAs made with either a 22 wt.% or 52 wt.% PtNi/C. After 30,000 metal dissolution tests, the PtNi/C fiber cathode MEA lost only 19% of its power at 0.65 V (similar to the loss observed in a PtCo/C fiber cathode MEA), while the sprayed MEA lost 30%. The PtNi/C fiber cathode, however, was highly susceptible to oxidation of

the carbon support after a carbon corrosion voltage cycling AST, where the maximum power decreased by 55% with a 22 wt.% decrease in carbon support via oxidation to CO_2.

3.5 References

1. T. T. Team, *Tesla* (2020).

2. *Tesla* https://www.tesla.com/supercharger.

3. *Green Car Congr.* (2014) https://www.greencarcongress.com/2014/11/20141118-mirai.html.

4. *Off. Energy Effic. Renew. Energy* https://www.energy.gov/eere/fuelcells/doe-technical-targets-polymer-electrolyte-membrane-fuel-cell-components.

5. R. Borup, in *Presentation to USCAR*, (2019).

6. O. T. Holton and J. W. Stevenson, *J. Electrochem. Soc.*, **57**, 864–890 (2013).

7. V. Jalan and E. J. Taylor, *Electrochem. Soc. Ext. Abstr.*, **83**–**1**, 1072–1073 (1983).

8. S. Mukerjee, S. Srinivasan, M. P. Soriaga, and J. McBreen, *J. Electrochem. Soc.*, **142**, 1409 (1995).

9. N. M. Markovic, H. A. Gasteiger, and P. N. Ross, *J. Phys. Chem.*, **99**, 3411–3415 (1995).

10. J. J. Slack et al., *J. Electrochem. Soc.*, **166**, F3202–F3209 (2019).

11. S. Mitsushima, S. Kawahara, K. Ota, and N. Kamiya, *J. Electrochem. Soc.*, **154**, B153–B158 (2007).

12. S. Chen, H. A. Gasteiger, K. Hayakawa, T. Tada, and Y. Shao-Horn, *J. Electrochem. Soc.*, **157**, A82–A97 (2010).

13. H. Yano, T. Akiyama, P. Bele, H. Uchida, and M. Watanabe, *Phys. Chem. Chem. Phys.*, **12**, 3806–3814 (2010).

14. K. F. Blurton, H. R. Kunzt, and D. R. Rutt, *Electrochim. Acta*, **23**, 183–190 (1978).

15. M. S. Wilson, F. H. Garzon, K. E. Sickafus, and S. Gottesfeld, *J. Electrochem. Soc.*, **140**, 2872–2877 (1993).

16. K. Kinoshita, J. T. Lundquist, and P. Stonehart, *Electroanal. Chem. InterJacial Electrochem.*, **48**, 157–166 (1973).

17. Y. Sugawara, T. Okayasu, A. P. Yadav, A. Nishikata, and T. Tsuru, *J. Electrochem. Soc.*, **159**, F779–F786 (2012).

18. P. J. Ferreira et al., *J. Electrochem. Soc.*, **152**, A2256–A2271 (2005).

19. H. R. Colón-Mercado, H. Kim, and B. N. Popov, *Electrochem. commun.*, **6**, 795–799 (2004).

20. P. Yu, M. Pemberton, and P. Plasse, *J. Power Sources*, **144**, 11–20 (2005).

21. D. D. Papadias et al., *J. Electrochem. Soc.*, **165**, F3166–F3177 (2018).

22. C. A. Reiser et al., *Electrochem. Solid-State Lett.*, **8**, 273–276 (2005).

23. M. F. Mathias et al., *Electrochem. Soc. Interface*, **14**, 24–35 (2005).

24. N. Macauley et al., *J. Electrochem. Soc.*, **165**, F3148–F3160 (2018).

25. S. S. Kocha, in *Polymer Electrolyte Fuel Cell Degradation*, M. M. Mench, E. C. Kumbur, and T. N. Veziroglu, Editors, p. 89, Academic Press, Boston (2012).

26. A. Kumar and V. Ramani, *ACS Catal.*, **4**, 1516–1525 (2014).

27. Y. Liu and W. E. Mustain, *J. Am. Chem. Soc.*, **135**, 530–533 (2013).

28. B. Seger, A. Kongkanand, K. Vinodgopal, and P. V. Kamat, *J. Electroanal. Chem.*, **621**, 198–204 (2008).

29. M. Brodt, R. Wycisk, N. Dale, and P. Pintauro, *J. Electrochem. Soc.*, **163**, F401–F410 (2016).

30. J. J. Slack et al., *J. Electrochem. Soc.*, **167**, 054517 (2020).

31. M. Choun, D. Nauryzbayev, D. Shin, and J. Lee, *Catal. Today*, **262**, 155–160 (2016).

32. M. L. Perry, T. Patterson, and C. Reiser, *ECS Trans.*, **3**, 783–795 (2006).

33. W. Zhang and P. N. Pintauro, *ChemSusChem*, **4**, 1753–1757 (2011).

34. M. Brodt, R. Wycisk, and P. N. Pintauro, *J. Electrochem. Soc.*, **160**, F744–F749 (2013).

35. M. Brodt et al., *J. Electrochem. Soc.*, **162**, F84–F91 (2015).

36. H. A. Gasteiger, S. S. Kocha, B. Sompalli, and F. T. Wagner, *Appl. Catal. B Environ.*, **56**, 9–35 (2005).

37. K. Cooper, *Fuel Cell Mag.*, 1–3 (2009).

38. A. Ohma, K. Shinohara, A. Iiyama, T. Yoshida, and A. Daimaru, *ECS Trans.*, **41**, 775–784 (2011).

39. T. Mashio et al., *ECS Trans.*, **11**, 529–540 (2007).

40. J. J. Slack, thesis, Vanderbilt University (2019).

41. R. K. Ahluwalia et al., *J. Electrochem. Soc.*, **165**, F3316–F3327 (2018).

42. L. Xin et al., *J. Electrochem. Soc.*, **164**, F674–F684 (2017).

43. K. Waldrop et al., *ECS Trans.*, **92**, 595–602 (2019).

44. M. Oezaslan, F. Hasché, and P. Strasser, *J. Phys. Chem. Lett.*, **4**, 3273–3291 (2013).

45. P. N. Pintauro, R. Tandon, L. Chao, W. Xu, and R. Evilia, *J. Phys. Chem.*, **99**, 12915–12924 (1995).

46. T. A. Greszler, D. Caulk, and P. Sinha, *J. Electrochem. Soc.*, **159**, F831–F840 (2012).

47. R. L. Borup et al., *Curr. Opin. Electrochem.*, **21**, 192–200 (2020).

48. E. Padgett et al., *J. Electrochem. Soc.*, **166**, F198–F207 (2019).

49. D. A. Stevens, M. T. Hicks, G. M. Haugen, and J. R. Dahn, *J. Electrochem. Soc.*, **152**, A2309–A2315 (2005).

50. J. J. Slack, R. Wycisk, N. Dale, A. Kumar, and P. N. Pintauro, *ECS Trans.*, **80**, 829–837 (2017).

CHAPTER 4 ELECTROSPUN NANOFIBER ELECTRODES SPUN FROM SALT-FORM NAFION FOR HIGH AND LOW HUMIDITY PEMFC OPERATION

Adapted from K. Waldrop, J.J. Slack, C. Gumeci, N. Dale, S. Reeves, D. Cullen, K. L. Moore, P. N. Pintauro, *ECS Trans.* **2019,** 92, 595-602 with permission from ECS.

4.1 Introduction

With atmospheric CO_2 levels on the rise and non-renewable energy sources being rapidly depleted, the need for sustainable, clean energy strategies is greater than ever. Proton-exchange membrane fuel cells (PEMFCs) have proven to be an excellent solution to the clean power issue, particularly for vehicular applications, owing to their zero-emissions operation and high energy conversion efficiencies. Several major automotive companies are engaged in fuel cell research and Toyota, Honda, and Hyundai are currently selling fuel cell electric vehicles (FCEVs). The current sale price of the fuel cell stack, however, is much too high for significant FCEV market share growth. This high price is largely due to the cost of the fuel cell stack components, particularly the expensive platinum-group-metal (PGM) catalysts. The cost of the hydrogen fuel is an additional economic barrier and therefore increasing the fuel utilization efficiency of the fuel cell stack is also important. To minimize Pt usage, the U.S. Department of Energy has set loading and power output targets of 0.125 mg_{Pt}/cm^2 and 1 W/cm^2 at rated power for an automotive PEMFC membrane-electrode-assembly (MEA),[1] which is significantly less than the 0.38 mg_{Pt}/cm^2 presently used , for example, in the Toyota Mirai.[2] The need for high power at low Pt loading has driven much of the fuel cell MEA research in recent years, such as the nanostructured thin film catalyst work at 3M Company,[3] electrosprayed catalyst layers,[4] and the

nanofiber mat electrode work from the Pintauro group,[5–11] which is the subject matter of this paper.

Presently, most fuel cell MEAs are tested and operate at high relative humidity feed gas conditions. It would be desirable for an automotive fuel cell stack to operate with high and near constant power and H_2 gas utilization at both low and high relative humidity (RH) feed gas conditions. Such a fuel cell stack would minimize/eliminate the need for pre-humidifying incoming feed gases, thus simplifying the fuel cell balance of plant. Unfortunately, at low humidity the ionic conductivity of the often used perfluorosulfonic acid ionomer (e.g., Nafion®) in the membrane and electrode binder drops significantly, resulting in increased cell resistance and low power output. Several strategies have been studied to mitigate power losses at low RH, including the use of lower equivalent weight (EW) ionomers[12,13] which are better proton conductors at low humidity, increased ionomer content in the catalyst layer,[14,15] modified gas diffusion layers to trap product water at the cathode,[16] incorporation of hydrophilic additives to the catalyst layers,[17] and the use of ultra-thin membranes[18] to promote the back diffusion of electrogenerated water from the cathode to the anode. While all of the methods resulted in some performance improvements, the low humidity power output was still far less than that at 100% RH and in some cases highly hydrophilic MEAs that worked well at low RH were prone to cathode flooding at 100% relative humidity operation. For example, Uchida and co-workers found that an MEA with 557 EW PFSA ionomer binder exhibited improved performance at 53% RH (e.g., 240 mW/cm^2 versus 120 mW/cm^2 for an 1100 EW binder MEA at 0.6 V), but the current density from 700 mA/cm^2 at 80% RH to 300 mA/cm^2 at 100% RH and 0.6 V due to flooding.[12] Park et al. qualitatively saw a similar effect when increasing the catalyst layer ionomer content from

20% to 35%.[14] Inoue et al. observed a 150% improvement in power density at 30% RH when hydrophilic SiO_2 was added to the cathode catalyst layer, but the low RH power was still half that reported at full humidification conditions.[17] The only method to improve low RH performance without sacrificing power at high humidity was the use of ultrathin membranes. For example, researchers from W. L. Gore & Associates reported in 2011 that the current density at 0.6 V for an MEA with a 35 μm thick membrane was 1100 mA/cm^2 at 100% RH and 790 mA/cm^2 at 18% RH, whereas a 10 μm thick membrane led to a current of 1380 mA/cm^2 at 100% RH and 1010 mA/cm^2 at 18% RH (a higher power at 18% RH for the thin versus a thick membrane, although the percentage power loss at 18% vs. 100% RH was the same for thick and thin membranes).[18]

The focus of the present study was two-fold: (i) to prepare and evaluate the performance of nanofiber mat electrodes using electrospinning inks containing Nafion and polyethylene oxide (PEO) and (ii) to assess the power output of the resulting nanofiber mat electrode MEAs at high and low relative humidity conditions. This work represents the latest in a series of studies by Pintauro research group, who have illustrated the utility of electrospun particle polymer electrodes for fuel cell applications.[5–8,10] It has already been shown[6] that MEAs with fiber mat Pt/C electrodes at a cathode Pt loading of 0.1 mg/cm^2 produced 34% more power at 100% RH than a conventional spray electrode MEA with a cathode loading of 0.4 mgPt/cm^2 . Fiber electrode MEAs also exhibited improved durability in carbon corrosion and Pt dissolution accelerated stress tests (ASTs), where the deleterious effects of flooding after a cathode carbon corrosion AST did not occur.[7] More recently, Slack et al. compared fiber and sprayed electrode MEAs with a PtCo/C cathode catalyst and found that the nanofiber MEAs produced 20% higher power and exhibited better durability in a metal dissolution AST, where metal loss/aggregation

was less in the fiber electrode MEA as compared to a conventional spray.[10] In all of these studies, the binder for anode and cathode fiber mats was a mixture of Nafion perfluorosulfonic acid (PFSA) and poly(acrylic acid) (PAA), where PAA was added in order to effectively electrospin an alcohol/water Nafion dispersion (PAA is often referred to as a "carrier polymer" for PFSA electrospinning). Ideally, PAA should be extracted from a fiber mat after electrospinning. It has been shown that the presence of carrier polymer in Nafion fibers leads to a decrease in the proton conductivity of the ionomer, either via Nafion/carrier polymer interactions through Nafion's sulfonic acid groups or simply by diluting Nafion with the carrier polymer which has no/minimal proton conductivity.[19] The presence of PAA with acid form Nafion (i.e., in fibers made with an ink containing Nafion with H^+ counterions) suppressed fuel cell power output in a slurry electrode MEA, and attempts to remove PAA from slurry and fiber electrodes by soaking in hot H_2SO_4 or 3% H_2O_2 at room temperature were unsuccessful.[7]

Prior polymeric fiber mat studies with Nafion and no catalyst particles showed that the proton conductivity of the final fiber mat could be improved if an extractable carrier polymer is used during the electrospinning.[20] This was achieved in the present study by using salt-form Nafion binder (where the counterion is not H^+) with either PAA or poly(ethylene oxide) (PEO) as the electrospinning carrier polymer. After removal of carrier by soaking in water, the fiber mat electrodes generated higher power in beginning-of-life experiments , as compared to fibers with acid-form Nafion and PAA, with the unexpected added benefit of high power at low feed gas RH.

The use of a Na^+-Nafion + PEO binder for electrospun fiber electrodes was first reported by Slack who examined both PtCo and Pt cathode catalysts with this new binder.[21] Removal of

PEO from the fiber electrode was confirmed via NMR analysis of water after soaking the MEA for 1 hour at 80 °C. Slack also reported that use of a Na^+-Nafion + PEO electrode binder resulted in a 25% increase in power density at 0.65 V versus a H^+-Nafion + PAA electrode binder. Power generation of MEAs with fiber electrodes prepared with a Na^+-Nafion + PEO binder was also less dependent on the relative humidity of the feed gases as compared to MEAs with H^+-Nafion + PAA fiber electrodes. This chapter is a continuation and expansion upon the work of Slack, with a more in-depth investigation of the effects of electrode binder and morphology.

4.2 Experimental

4.2.1 Electrode and MEA Preparation

Electrode inks for electrospinning were prepared with a 46 wt.% Pt/C catalyst (TEC10F50E from the Tanaka Kikinzoku Kogyo Group that utilizes Acetylene black as the carbon substrate), 1100 EW Nafion ionomer dispersion (Ion-Power Liquion LQ-1115), and either poly(acrylic acid) (450kDa) or poly(ethylene oxide) (600 kDa) (purchase from Sigma Aldrich), which served as a carrier polymer to enable fiber formation from the Nafion dispersion. Addition of PEO to a catalyst ink containing acid-form Nafion resulted in rapid loss of ink viscosity and insufficient chain entanglement for fiber production (presumably due to decomposition of PEO in the presence of catalyst and strongly acidic Nafion). To correct this problem, Nafion in the sodium counter-ion form was used when spinning electrode fibers with PEO. To deconvolute the effects of salt-form Nafion vs. PEO carrier on cathode performance in a fuel cell, an ink with Na^+-form Nafion/PAA binder was also examined. For completeness, fiber mat cathodes were prepared with acid-form Nafion/PAA binder. All cathodes had a Pt loading of 0.1 mg/cm^2.

After mixing, inks were electrospun using a single needle spinneret. Fibers were collected on an electrically grounded rotating drum. The needle and collector drum were housed in a humidity-controlled plexiglass chamber. Acid-form Nafion/PAA inks were spun at a rate of 1.0 mL/h, a needle tip-to-collector distance of 11.0 cm, 11.0 kV applied voltage, and 40% RH. Na^+-form Nafion inks with either PEO or PAA were spun at a rate of 0.75 mL/h, 20.0 cm needle-to-collector distance, an applied voltage of 8.0 kV, and 20% RH. Spinning was stopped when fiber mats reached the required Pt loading, based on the flow rate of ink during electrospinning and the Pt/C content of the ink. The dry mat composition (weight % catalyst:ionomer:carrier) was 58:28:14 for the H^+-Nafion:PAA and Na^+-Nafion:PAA fibers; and 52:37:11 for the Na^+-Nafion:PEO fibers.

Catalyst coated membranes (CCMs) were prepared via hot-pressing at 140 °C and 3 MPa for 5 minutes, where fiber electrodes of the same composition and Pt loading were used as both the anode and cathode. Sections of 5 cm^2 fiber mat were pressed onto the opposing surfaces of a Nafion 211 membrane. CCMs made with salt-form Nafion fibers were soaked in 0.5 M H_2SO_4 at 80 °C for one hour and then DI water at 80 °C for 1 hour. These two soaking steps were used to replace the alkali metal cations (counterions) in Nafion with H^+ and to remove water soluble PAA or PEO carrier polymer from the fibers. The CCMs were then dried under vacuum for 10 minutes prior to being fitted with gaskets and Sigracet 29 BC gas diffusion layers (GDLs).

In order to contrast the effects of binder type and electrode morphology (slurry vs. fiber) on fuel cell performance, Pt/C slurry electrodes were prepared with: (i) neat H^+-Nafion binder(slurry electrodes only), (ii) H^+-Nafion:PAA binder (slurry and fibers), (iii) Na^+-Nafion:PAA binder

(slurry and fiber), and (iv) Na^+-Nafion:PEO binder (slurry and fiber), with weight ratio compositions of 58:42 catalyst:H^+-Nafion, 58:28:14 catalyst:H^+-Nafion:PAA, 58:28:14 catalyst:Na^+-Nafion:PAA, and 52:37:11 catalyst:Na^+-Nafion:PEO, respectively. Inks were prepared in an alcohol/water solvent, cast onto carbon paper, and allowed to dry. Electrodes were soaked in 80 °C water for 1 hour and then vacuum dried to remove the "carrier" polymer before being hot-pressed onto a Nafion 211 membrane. In a given MEA, the anode and cathode (each at 0.1 mg_{Pt}/cm^2) used the same binder.

4.2.2 Microscopy

Top-down SEM micrographs of fiber mats were collected using a Zeiss Merlin scanning electron microscope. Samples for scanning transmission electron microscopy (STEM) were prepared by embedding MEA sections in epoxy, which were then cut into 50-100 nm thick cross-sections at Oak Ridge National Laboratory with a Leica EM UC7 microtome. Samples were placed onto transmission electron microscope (TEM) grids. STEM high angle annular dark field images (HAADFs) and elemental maps were collected with a Tecnai Osiris S/TEM using a single-tilt aluminum holder. Intrafiber porosity and the pore-size distribution of fiber mat cathodes were determined from ImageJ analyses of binarized HAADF images of fiber cross sections. Elemental maps of Pt and F from fiber cross sections were obtained using energy dispersive x-ray spectroscopy (EDS).

4.2.3 Fuel Cell Testing

At Vanderbilt University, fuel cell tests were carried out using a Scribner 850e test station and a Fuel Cell Technologies 5 cm^2 testing block with single serpentine anode and cathode flow fields.

Polarization data were collected at 80 °C, with hydrogen and air flowrates of 125 and 500 sccm, respectively. Relative humidity was varied from 40-100% for operating pressures between 100-250 kPa_{abs}. Voltage was swept from 0.2 V to OCV at intervals of 0.05 V with a 1-minute hold at each voltage to allow for current stabilization. Oxygen reduction mass activity was calculated from the hydrogen cross-over and high-frequency resistance corrected current density at 0.9 V and 80 °C with fully humidified H_2 and O_2 feeds to the anode and cathode, respectively, as described elsewhere.[20] Electrochemically active surface area (ECSA) was measured at 30 °C and ambient pressure from hydrogen adsorption/desorption cyclic voltammograms, using an external potentiostat (Gamry Reference 3000).[22]

4.3 Results and Discussion

4.3.1 Analysis of Fiber Structure

Fiber electrode structure was investigated using SEM and STEM/EDX. Top-down SEM micrographs and EDS elemental maps of individual fiber cross-sections are illustrated in Figures 4.1 and 4.2, respectively. It can be seen from the SEMs that all three binder types (H^+-Nafion/PAA, Na^+-Nafion/PAA, and Na^+-Nafion/PEO) result in well-formed fibers. Although there is some variability in fiber diameter, there are no droplets or bead-on-fiber defects and the distribution of catalyst along the length of the fibers appears to be uniform. The elemental maps in Figure 4.2, where red denotes platinum and green represent fluorine (from Nafion), reveal that the cross-sectional fiber composition/structure is similar for all three binders, where the fiber surface is ionomer-rich and the interior is enriched with catalyst. Numerous nanovoids are present in all three fibers. Unfortunately, due to the difference in molar mass between Pt and F (with Pt being

a much heavier element), the counts for fluorine were not sufficiently accurate for determination of the radial variation in I/C ratio.[22] For comparison, electrode cross-section elemental maps of sprayed electrodes with neat H^+-Nafion and Na^+-Nafion/PEO binders are shown in Figure 4.3. Here, the ionomer and catalyst are uniformly distributed in the electrode thickness direction. These results clearly show that the observed phase separation of ionomer and catalyst in Figure 4.2 is a consequence of the electrospinning process and not the ink composition. In a prior publication,[14] fibers with PtCo/C catalyst with H^+-Nafion/PAA binder did not show the Nafion surface enrichment that is seen in Figure 4.2a. Upon further investigation of cross-sectional elemental map images of PtCo/C fibers with acid-form Nafion and PAA, it was found that the majority of the fibers did indeed show ionomer surface enrichment. Thus, it can be further concluded that the cross-sectional distribution of catalyst and ionomer seen in Figure 4.2 is observed for both Pt/C and carbon-supported Pt-alloy catalysts.

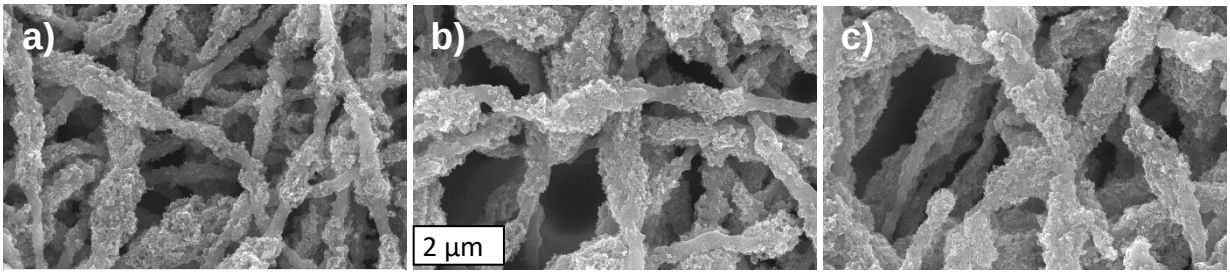

Figure 4.1: Top-down SEM images at 30,000 times magnification of fiber electrodes prepared with a binder of a) H^+-Nafion/PAA, b) Na^+-Nafion/PAA, and c) Na^+-Nafion/PEO.

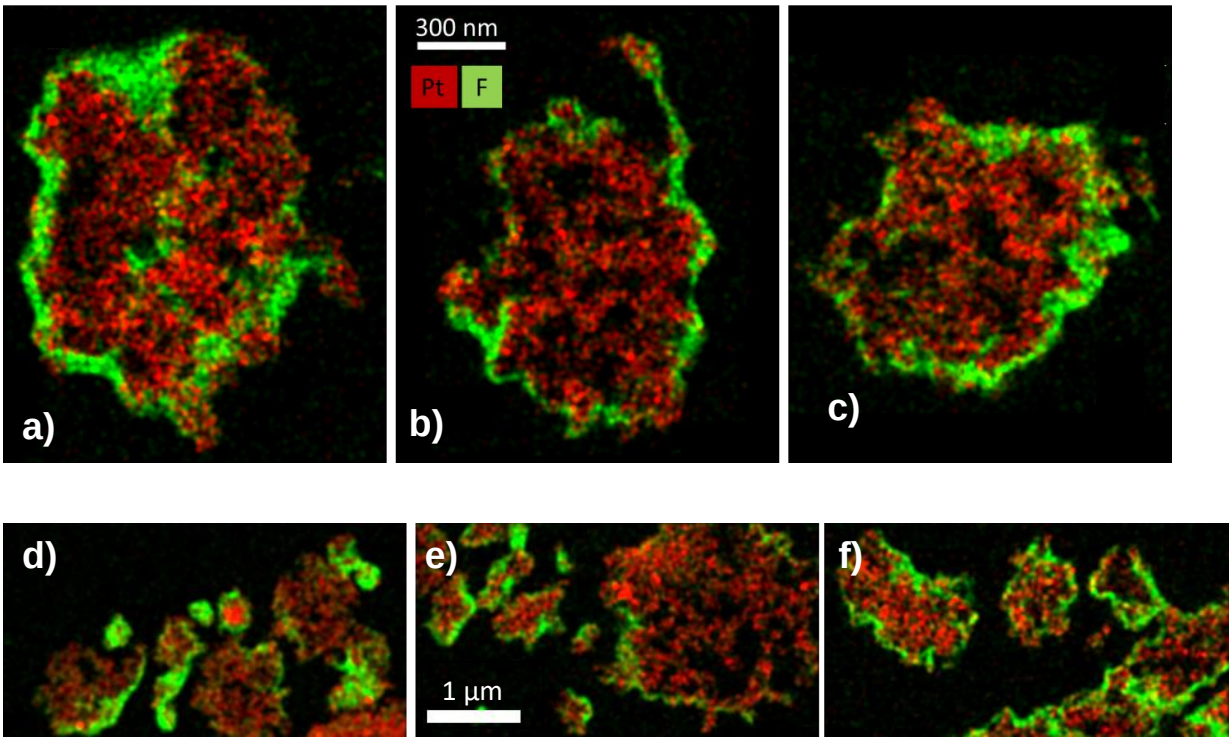

Figure 4.2: Fiber cross-section elemental maps at (a-c) 56,000 and (d-f) 20,000 times magnification for fibers prepared with a binder of a,d) H^+-Nafion/PAA, b,e) Na^+-Nafion/PAA, and c,f) Na^+-Nafion/PEO. Green denotes Nafion ionomer, red denotes Pt and black is open void space.

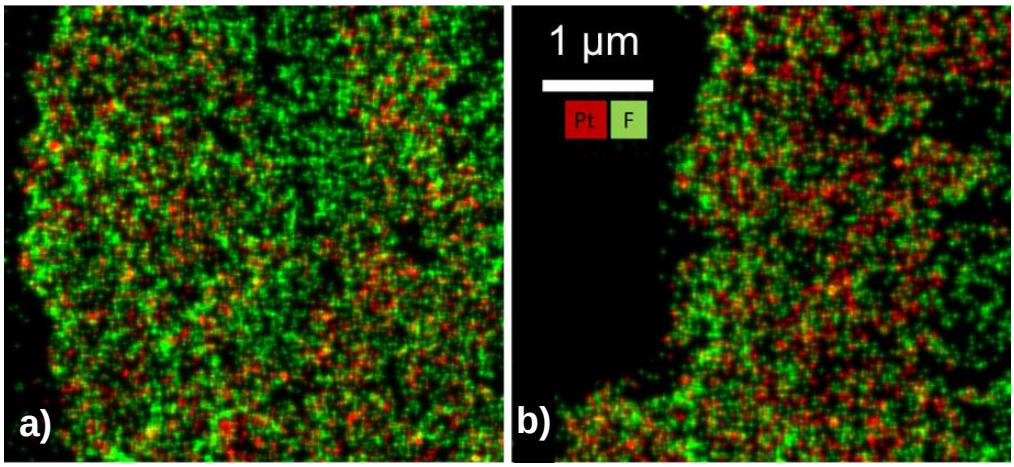

Figure 4.3: Cross-section elemental maps of sprayed electrodes prepared with a binder of a) neat H^+-Nafion and b) Na^+-Nafion/PEO.

4.3.2 Removal of Carrier Polymers as Determined by NMR

Fiber electrode mats were soaked in 80 °C D_2O for 1 hour to leach out water-soluble carrier polymer (either PEO or PAA), followed by analysis of the soak solution by NMR (Bruker AV-400 400 MHz NMR). The experiments were performed to determine if the counterion form of Nafion in the catalyst ink affected carrier polymer removal after fiber spinning. The NMR results showed a distinct PEO peak in the wash water after soaking a fiber mat cathode with a Na^+-Nafion/PEO binder. The peak height correlated well (within 97%) with the known PEO content in the prepared ink. A small peak for PAA with many other unidentifiable peaks were seen in the wash water of a fiber mat electrode made with Na^+-form Nafion/PAA, suggesting PAA leaching and decomposition. No such PAA peak was seen after soaking a fiber mat electrode with H^+-Nafion/PAA binder, confirming the results reported previously that PAA cannot be removed from acid-form Nafion fibers.[7]

4.3.3 Fuel Cell Performance of Fiber Electrode MEAs

4.3.3.1 Fuel Cell Performance Under Full Humidification

Nanofiber H_2/air fuel cell polarization data were collected under fully humidified conditions, as plotted in Figure 4.4. Power densities for the entire voltage regime (0.2 V to OCV) were higher for the fiber mat MEA with Na^+-form Nafion versus the H^+-form Nafion fiber electrode. The Na^+-Nafion/PEO, Na^+-Nafion/PAA, and H^+-Nafion/PAA fibers produced maximum power densities of 906, 875, and 788 mW/cm^2, respectively. The higher power is associated with a high binder conductivity when no carrier is present, but the cathode ECSA for salt-form Nafion binder fibers (with PAA or PEO) also increased by 20% as compared to fibers made with H^+-Nafion/PAA (see Table 4.1). The carrier polymer is a significant component of the binder (either 28:14 or 37:11

Nafion:carrier ratio) and carrier extraction appears to increase the catalyst surface area in contact with air. As expected, the high frequency resistance (HFR) of the acid-form Nafion/PAA fiber mat is higher than that with salt-form Nafion due to its higher ionic resistance. Interestingly, despite the difference in ECSA, there was no appreciable change in oxygen reduction reaction mass activity for the three different fiber compositions (where the 10% increase in activity for the Nafion/PEO mat was within experimental error).

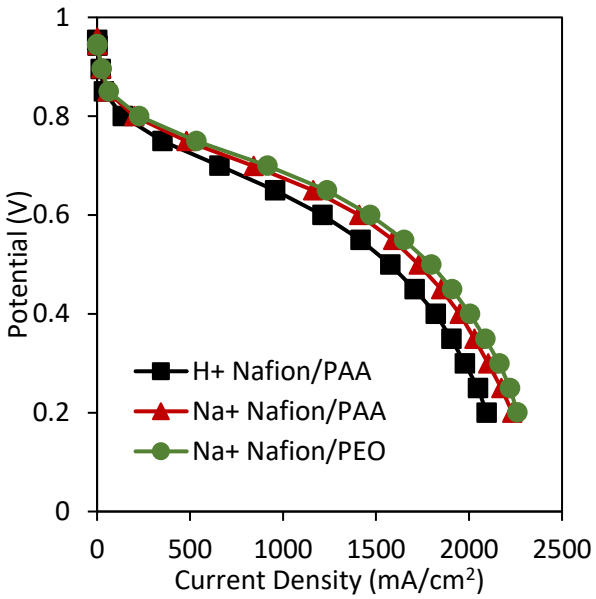

Figure 4.4: Polarization curves for fiber electrode MEAs using Pt/C (TKK) with binders of (black squares) H^+-Nafion/PAA, (red triangles) Na^+-Nafion/PAA, and (green circles) Na^+-Nafion/PEO. Data were collected at 80 °C, 200 kPa_{abs}, 100% RH, with hydrogen and air flowrates of 125 and 500 sccm, respectively.

Table 4.1: Oxygen reduction reaction (ORR) mass activity, electrochemically active surface area, and high frequency resistance for fiber electrode MEAs with varying binders.

	H^+-Nafion/PAA	Na^+-Nafion/PAA	Na^+-Nafion/PEO
ORR Mass Activity (mA/mg_{Pt})	138	138	150
ECSA (m^2/g_{Pt})	58	65	70
HFR ($m\Omega \cdot cm^2$)	65	51	53

4.3.3.2 The Effect of Humidity on MEA Performance

Whereas the results in Figure 4.4 show a modest but significant improvement in fuel cell performance when using a salt-form Nafion binder, the effect of binder on power output was more pronounced when the feed gas RH was lowered. Polarization data at 40% RH (see Figure 4.5a), show that the H^+-form Nafion/PAA fiber electrode MEA suffered a significant power loss with decreasing RH, as compared to MEAs prepared with Na^+-form Nafion and either PEO or PAA. The difference in binder types was most prominent in the ohmic region (0.4-0.65 V), where the HFR was 194, 85, and 86 $m\Omega \cdot cm^2$ at 0.65 V for H^+-Nafion/PAA, Na^+-Nafion/PAA, and Na^+-Nafion/PEO fibers, respectively. Since HFR is a measurement of membrane and membrane/electrode contact resistance, it is concluded that fiber electrodes prepared with Na^+-Nafion allow the electrodes and membrane to retain more water at low humidity (the ionic resistance of Nafion drops significantly with decreasing water content). The removal of PEO or PAA from the electrode fibers also helps to improve power, since these carrier polymers dilute Nafion and their presence lowers the overall conductivity of the binder at both high and low RH.[12,15] As shown in Figure 4.5b, the maximum power was nearly constant from 40%-100% RH

for the two nanofiber electrode MEAs prepared using Na^+-form Nafion. For MEAs with H^+-Nafion/PAA fiber electrodes, there was a modest but discernible optimum in maximum power vs. relative humidity at ~80% RH; at higher humidification there was some electrode flooding (the PAA carrier polymer added to the hydrophilicity of the cathode) while at lower RH there was ionomer dehydration and a drop in proton conductivity. There was no indication of cathode flooding with salt-form Nafion binder at high current densities. Notably, fiber electrodes were also spun with PEO and Nafion in either the Li^+ and Cs^+ counterion form; for these binders, the fuel cell results were comparable to those observed using a Na^+-form of Nafion in the anode and cathode fibers.

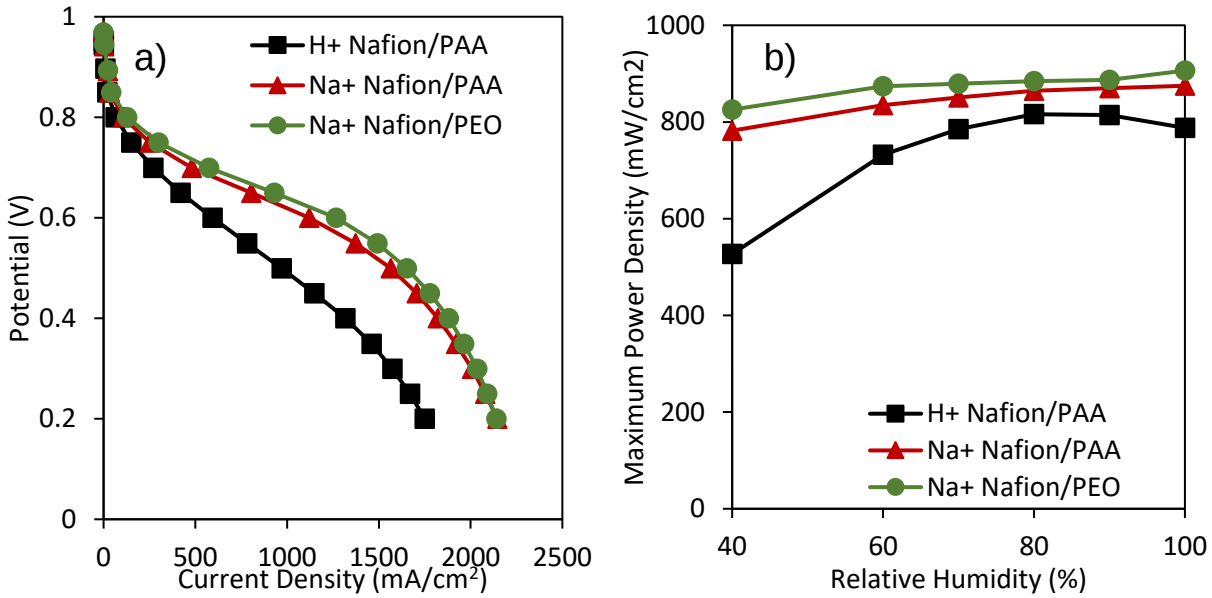

Figure 4.5: a) Polarization data at 40% RH and b) maximum power density vs. relative humidity for fiber electrode MEAs using Pt/C (TKK) with binders of (black squares) H^+-Nafion/PAA, (red triangles) Na^+-Nafion/PAA, and (green circles) Na^+-Nafion/PEO. Data were collected at 80 °C, 200 kPa_{abs}, with hydrogen and air flowrates of 125 and 500 sccm, respectively.

4.3.3.3 The Effect of Operating Pressure on Performance

The pressure of the incoming H_2 and air feed gases significantly influenced nanofiber MEA power output, as can be seen in the polarization curves plotted in Figures 4.6a (for Na^+-Nafion/PEO fiber binder) and 4.6b (H^+-Nafion/PAA). The effect of backpressure on power at 100% RH and 40% RH was more pronounced for the H^+-Nafion/PAA fiber MEA, e.g., at 100% RH and 0.65 V, the power density for the acid-form Nafion MEA increased by 77% vs. a 63% increase for the salt-form Nafion binder, when the pressure was increased from 100 to 250 kPa_{abs}. For both binder types, the shape of the V-i curves suggests this improvement arises in the activation region, where there is better oxygen reduction kinetics, likely due to the increased partial pressure of oxygen when operating at elevated pressure. The effect of pressure was most notable at 40% RH, where the maximum power doubled for the Na^+-Nafion/PEO MEA at 250 kPa_{abs} as compared to 100 kPa_{abs}, and the H^+-Nafion/PAA MEA maximum power increased by a factor of 3 for the same change in back pressure. The slopes of the polarization curves in the ohmic region are less steep at elevated pressure and the measured HFR decreased by 50% and 60% for the Na^+-Nafion/PEO and H^+-Nafion/PAA MEAs, respectively, when the backpressure was increased from 100 kPa_{abs} to 250 kPa_{abs}. Also, as pressure is increased, fewer moles of water are needed to saturate air. Consequently, at higher pressures the cathode is better hydrated, leading to reduced ohmic losses and high power at low humidity.[23–25]

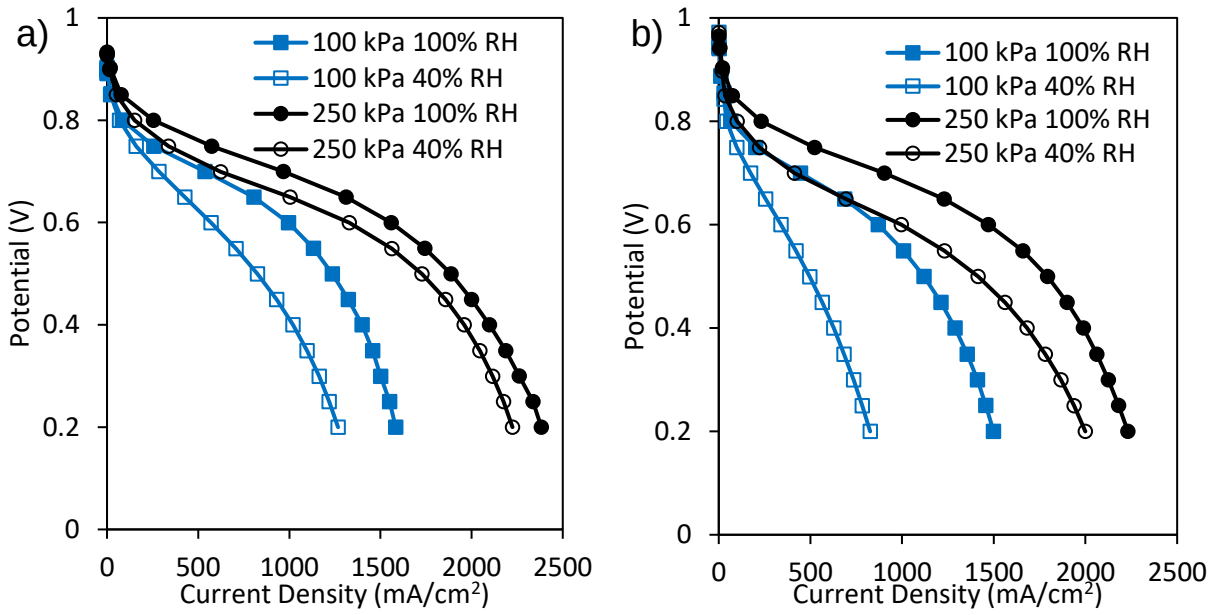

Figure 4.6: Polarization curves for fiber electrode MEAs prepared with (a) Na^+-Nafion/PEO and (b) H^+-Nafion/PAA at 100% (filled) and 40% RH (open) and either 100 kPa_{abs} (blue squares) or 250 kPa_{abs} (black circles). Data were collected at 80 °C with H_2/air flowrates of 125/500 sccm.

The ratio of power densities at 40% RH and at 100% RH as a function of operating voltage was examined to better understand RH effects in fiber mat electrode MEAs. The resulting data are plotted for Na^+-Nafion/PEO and H^+-Nafion/PAA fiber electrode MEAs in Figure 4.7. It is expected that higher operating voltages would result in poor power retention at low humidity due to less water production at the cathode and consequently less back diffusion of water from the cathode to the anode. For both binders, the power ratio decreased with increasing potential and decreasing backpressure, but fiber electrode MEAs prepared with Na^+-Nafion binder were less sensitive to these operating conditions and retained more power overall than the H^+-Nafion/PAA MEA. Even at high voltage (low current density) where little water was produced, the Na^+-Nafion/PEO fibers retained more power than the H^+-Nafion/PAA fibers. Thus, for a fiber

mat MEA made with Na^+-Nafion/PEO binder, the power densities at 40% RH and 100% RH are essentially the same for operating voltages between 0.20 and 0.55 V. The voltage window for a power ratio of 1.0 in Figure 4.7a could be extended to higher voltages if thinner membranes were used for the fiber MEAs (a 25 µm thick membrane was used for all MEAs in the present study). Similarly, the use of a thinner membrane in a MEA with nanofiber electrodes will generate higher power at feed gas humidities less than the 40% RH lower limit of the present study. Such experiments will be the subject of a future study, where the goal is to achieve a 20%/100% RH power density ratio of near 1.0 at voltages as high as 0.75 V at 80 °C (to improve H_2 utilization efficiency and minimize radiator size for automotive fuel cell stacks). The effect of RH on the performance of slurry electrodes with H^+-form Nafion and salt-form Nafion is discussed next.

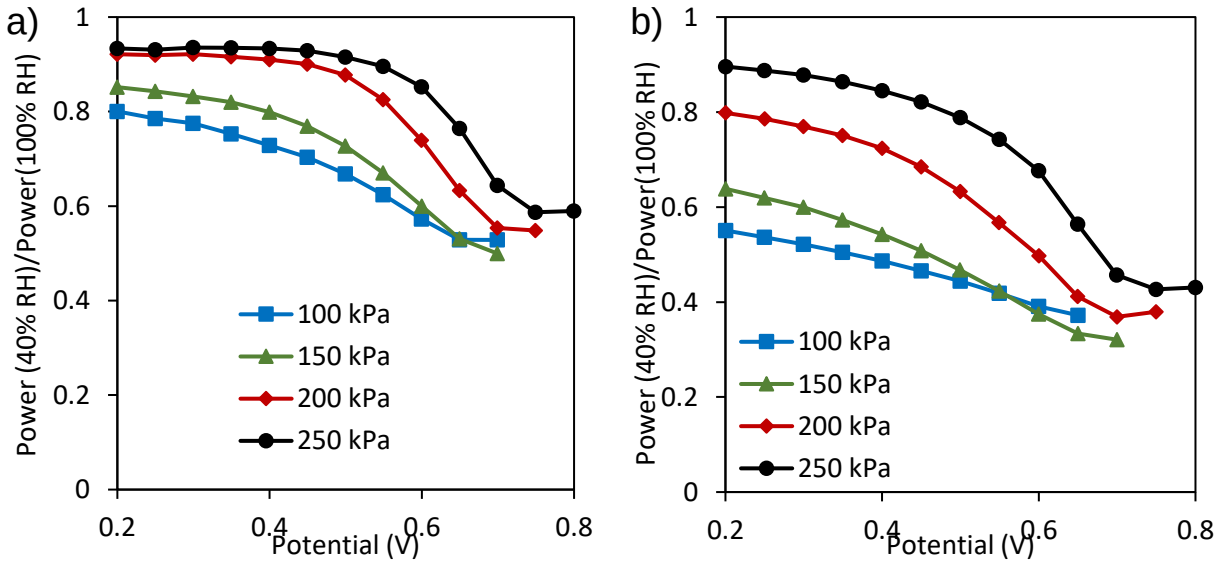

Figure 4.7: Ratio of power at 40% RH and 100% RH vs. potential at varied pressures for fiber electrode MEAs prepared with a binder of a) Na^+-Nafion/PEO and b) H^+-Nafion/PAA. Data were collected at 80 °C with hydrogen/air flowrates of 125/500 sccm.

4.3.4 The Effect of Binder on the Performance of Slurry Electrode MEAs

From the data above it is unclear if the high power at low humidity was a consequence of the electrode binder or was due to the combined effects of electrode binder and fiber morphology. To address this question, the performance of slurry electrode MEAs was studied with various salt-form Nafion binders, where the inks also contained the PAA and PEO carrier polymers that were required to electrospin fiber mats. Polarization curves are plotted in Figure 4.8a, where MEAs prepared with Na^+-Nafion and either PAA or PEO produced the same power at 100% RH as the neat H^+-Nafion slurry MEA (after PAA or PEO removal). These data further support the earlier finding that both of the water-soluble electrospinning carrier polymers can be removed from electrodes with Na^+-Nafion binder by soaking the MEA in water. The slurry MEA with H^+-Nafion and PAA generated low power, which is consistent with results from prior studies where the presence of PAA lowers the proton conductivity of Nafion.[7] At 40% RH (Figure 4.8b), there was a significant drop in power density for all four MEAs, with the neat Nafion and Na^+-Nafion/PEO electrode MEAs performing best (a drop of ~20% in peak power). The difference in low humidity performance when comparing Na^+-Nafion/PEO and Na^+-Nafion/PAA likely arises from a difference in ionomer-to-carbon (I/C) ratio. After leaching PEO from the binder, the I/C ratio of the Na^+-Nafion/PEO sample was 1.34 (very close to the I/C ratio of the neat Nafion electrode of 1.37), while removal of PAA from the Na^+-Nafion/PAA sample resulted in an I/C ratio of 0.91. It has been reported in the literature that a lower I/C ratio will lead to a greater loss in power with decreasing relative humidity of the feed gases.[15,19,26,27] The lower I/C ratio also resulted in increased HFR at low humidity, as shown by the data in Table 4.2. Considering the power loss experienced by all slurry MEAs at low humidity, it can be concluded that the humidity

independent behavior of Na^+-Nafion fibers with either PEO or PAA is a consequence of both the electrode binder and morphology.

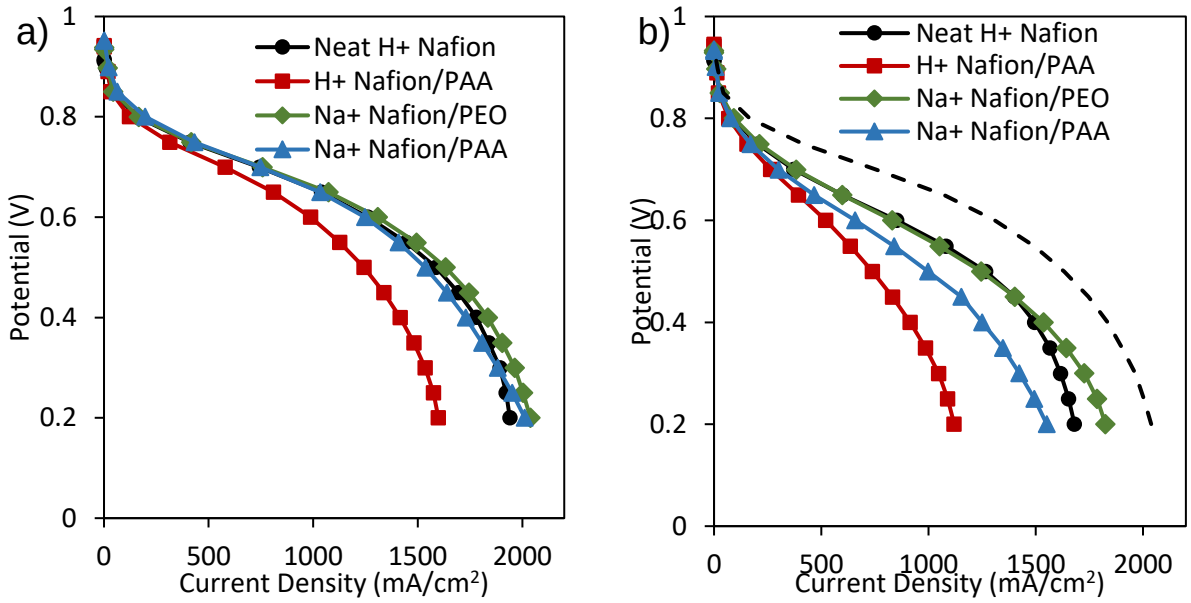

Figure 4.8: Polarization curves for slurry electrode MEAs with different anode/cathode binders at: (a) 100% RH and (b) 40% RH .The performance of a Na^+-Nafion/PEO slurry at 100% RH is also plotted in 8b as a dashed line. Data were collected at 80 °C and 200 kPa_{abs} with hydrogen/air flowrates of 125/500 sccm.

Table 4.2: High frequency resistance at 0.6 V for different slurry electrode binders and 100% RH and 40% RH.

	Neat H^+ -Nafion	H^+-Nafion/PAA	Na^+-Nafion/PAA	Na^+-Nafion/PEO
100% RH HFR ($m\Omega \cdot cm^2$)	58	65	74	60
40% RH HFR ($m\Omega \cdot cm^2$)	131	160	177	137

It is important to note that while these slurry electrodes were soaked in water to remove carrier polymer, they were not acid-washed to exchange the sodium ions in the Nafion binder. However, the data in Figure 4.8 show that the presence of sodium ions had no adverse effect on measured polarization curves. During the initial stages of fuel cell operation, it is believed that electrogenerated H^+ will displace Na^+ counterions in the cathode binder. Such counterion displacement was used previously to create Pt-alloy type cathodes in MEAs for electro-organic synthesis.[28] Qualitative evidence in support of this hypothesis was found by measuring the ionic conductivity of cathode product water during MEA break-in. For MEAs, made with Na^+-form Nafion binder, the combination of a water soaking step (to remove carrier) and acid soaking step (to exchange Na^+ with H^+) resulted in polarization curves identical to a neat Nafion binder MEA, with very low conductivity of the cathode effluent water. On the other hand, when the MEA was only soaked in water (i.e., the MEA in Figure 4.8a), the conductivity of the collected water in the cathode air exhaust was initially high, suggesting sodium ion release from the binder.

4.3.5 Pore Size Analysis

It is hypothesized that capillary condensation in nm-size pores present within electrospun fibers facilitates water retention at low RH, the unusual humidity independent power density behavior of certain nanofiber mat electrode MEAs. The pores form during electrospinning and/or after leaching of PEO or PAA from salt-form Nafion binder. Intrafiber porosity before and after a one-hour soak in 80 °C water is listed in Table 4.3 (the data were collected from digitized SEM fiber cross-sections). The water soak led to an appreciable increase in porosity for both Na^+-Nafion/PAA and Na^+-Nafion/PEO fibers, which serves as further evidence for removal of carrier polymer during a MEA water soaking step. In contrast, the internal fiber porosity of H^+-

Nafion/PAA fibers after a hot water soak was the same as that of a Na^+-Nafion/PAA fiber mat before water exposure. This observation is consistent with the NMR analysis discussed in Section 4.3.2, which showed that PAA did not leach out of H^+-Nafion/PAA fibers. The measured pore size distributions for the three binder types are plotted in Figure 4.9a where the y-axis represents the total number of pores in a given size range. Fibers prepared with Na^+-Nafion had more pores across the entire pore radius spectrum, as compared to the H^+-form Nafion/PAA fibers. For fibers made with Na^+-form Nafion: (i) The greater number of large pores (with a radius > 10 nm) may aid in removal of excess water during fuel cell operation, minimizing flooding and improving power under fully humidified conditions and (ii) the increased number of small pores (< 3 nm) could allow for capillary condensation of water within the fibers which would improve protonic conductivity and MEA performance during low humidity operation.

Table 4.3: Intra-fiber porosity before and after a one-hour soak in 80 °C water for fiber electrodes prepared with different binders.

	Porosity before water soak	**Porosity after water soak**
H^+-Nafion/PAA	--	6%
Na^+-Nafion/PAA	7%	15%
Na^+-Nafion/PEO	13%	17%

Costamagna et al. developed a model of capillary condensation within Nafion pores using a modified Kelvin equation.[29] Analysis of the critical pore radius needed for capillary condensation in Nafion pores at a given humidity was carried out using this model. The relationship between relative humidity and critical pore radius, r_C is given by Equation 4.1. Pores

smaller than this critical size will be filled with condensed water. In Equation 4.1, γ and V_L are the surface tension and molar volume of bulk water, respectively. At 80 °C γ = 0.00625 N/m and V_L = 18.5 ml/mol. R is the universal gas constant, T is temperature, p/p_0 is the partial pressure of water vapor over the saturation pressure (which defines the relative humidity), and t is statistical film thickness which accounts for a very thin layer of water adsorbed on the pore wall surface before the pore is flooded.

$$r_c = \frac{-2\gamma V_L}{RT\ ln\left(\frac{p}{p_0}\right)} + t \qquad \text{Equation 4.1}$$

In large pores, t is negligibly small compared to r_c, but in nanometer sized pores, as is the case for the intrafiber pores, it must be taken into consideration. The water film thickness is correlated to the relative humidity as defined by Costamagna and given in Equation 4.2, where λ is the moles of adsorbed water per mole of sulfonic acid, λm is a fitting parameter, and σ is the molecular diameter of a water molecule (~ 3 Å).

$$t = \frac{\lambda}{\lambda_m}\sigma \qquad \text{Equation 4.2}$$

Furthermore, Costamagna et al. defined the λ/λ_m ratio with relative humidity using the modified Brunauer–Emmet–Teller equation,

$$\frac{\lambda}{\lambda_m} = \frac{ck\frac{p}{p_0}}{\left(1-k\frac{p}{p_0}\right)\left(1+(c-1)k\frac{p}{p_0}\right)} \qquad \text{Equation 4.3}$$

where the constants c and k were obtained from a paper by Mashio et al.[30] for water adsorption in Nafion at 80 °C; they are listed in Table 4.4. The effect of RH on the critical pore radius, as

determined by Equations 4.1-4.3 is shown in Figure 4.9b. Based on the model, capillary condensation should occur to some extent for all three binder types (Na^+-form Nafion/PEO, Na^+-form Nafion/PAA, and H^+-form Nafion/PAA). However, fibers made with Na^+ form Nafion clearly have more pores in the size range for capillary condensation at 40% RH, i.e., a pore radius ≤ 1.25 nm.

Table 4.4: Fitting parameters for Equation 4.3 that were calculated from experimental water adsorption isotherms of Nafion at 80 °C

Fitting Parameter	Value
c	20
k	0.769

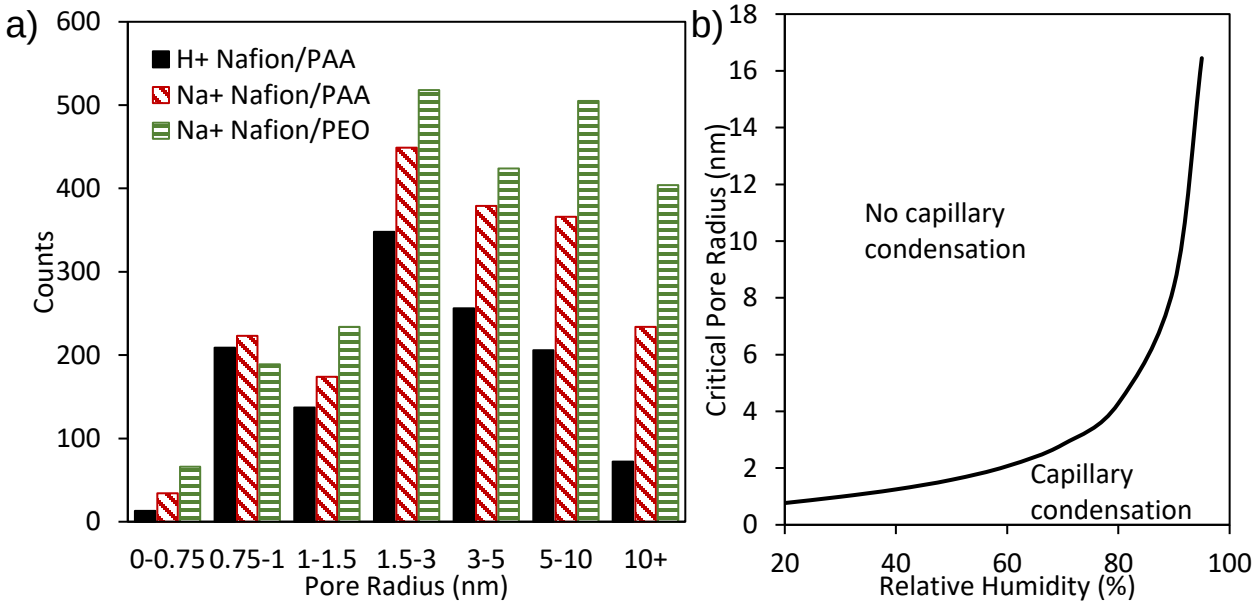

Figure 4.9: a) Intra-fiber pore radius distribution for fiber electrodes after a 1-hour soak in 80 °C water where the binder was (solid black) H^+-Nafion/PAA, (diagonal red) Na^+-Nafion/PAA, and (horizontal green) Na^+-Nafion/PEO. b) Theoretical critical pore radius vs. relative humidity for capillary condensation based on a modified Kelvin equation for desorption.

4.4 Conclusions

Fiber electrodes with Pt/C catalyst were prepared using a binder of Nafion in the sodium counter-ion form with either PEO or PAA as the electrospinning carrier polymer and the performance of MEAs with these electrodes were compared to MEAs with H^+-Nafion/PAA fibers. NMR analysis of the soaking water after fiber mat immersion revealed that PAA could not be removed from acid-form Nafion even though it is a water-soluble polymer (due to strong interactions between Nafion and PAA), whereas PEO and PAA did leach out of Na^+-Nafion fibers. Under fully humidified conditions and 200 kPa_{abs}, electrodes prepared with Na^+-Nafion and either PEO or PAA produced 20% higher power at 0.65 V than H^+-Nafion/PAA fiber electrodes. Sodium-form Nafion MEAs also exhibited excellent performance at low humidity, where the peak power decreased by only ~10% when the feed gas RH was decreased from 100% to 40%. In contrast, the H^+-Nafion/PAA fiber MEA lost 35% power for the same RH change. Humidity independent power density was also observed in fiber electrodes prepared with Nafion in the Cs^+ or Li^+ counter-ion form.

At 100% RH, slurry MEAs with Na^+-Nafion and either PEO or PAA produced the same power as neat H^+-Nafion, further confirming removal of polymer. The presence of PAA in the acid-form Nafion/PAA slurry lowered power under fully humidified conditions, likely due to flooding and lower protonic conductivity. Decreasing humidity from 100 to 40% RH in slurry electrode MEAs produced a substantial drop in power density (> 20%) for all binder types, although this effect was most pronounced in the H^+-Nafion/PAA slurry. The results confirmed that both binder type and electrode morphology affect humidity dependence.

Increased operating pressure lessened the effect of humidity on power output for both Na^+-Nafion and H^+-Nafion binder electrode MEAs. This was most noticeable in a H^+-Nafion/PAA binder system where the maximum power at 40% RH increased by a factor of 3 (from 250 to 710 mW/cm^2) when going from 100 to 250 kPa_{abs}. The maximum power of the Na^+-Nafion/PEO MEA only increased by a factor of 2 (418 to 863 mW/cm^2).

A STEM analysis revealed that intrafiber porosity of Na^+-Nafion fibers with either PEO or PAA increased appreciably after a 1-hour 80 °C water soak, presumably due to removal of the water-soluble carrier polymer. An increase in the number of pores with a radius greater than 5 nm allowed for facile accumulation and removal of product water from the catalyst/Nafion interface and, consequently, mitigated flooding at high operating humidity, while an increase in the number of pores with a radius less than 2 nm facilitated capillary condensation which resulted in high power at feed gas low humidity conditions.

4.5 References

1. *Off. Energy Effic. Renew. Energy* https://www.energy.gov/eere/fuelcells/doe-technical-targets-polymer-electrolyte-membrane-fuel-cell-components.

2. R. Borup, in *Presentation to USCAR*, (2019).

3. M. K. Debe, R. T. Atanasoski, and A. J. Steinbach, *ECS Trans.*, **41**, 937–954 (2011).

4. K. Takahashi, K. Kakinuma, and M. Uchida, *J. Electrochem. Soc.*, **163**, F1182–F1188 (2016).

5. W. Zhang and P. N. Pintauro, *ChemSusChem*, **4**, 1753–1757 (2011).

6. M. Brodt, R. Wycisk, and P. N. Pintauro, *J. Electrochem. Soc.*, **160**, F744–F749 (2013).

7. M. Brodt et al., *J. Electrochem. Soc.*, **162**, F84–F91 (2015).

8. M. Brodt, R. Wycisk, N. Dale, and P. Pintauro, *J. Electrochem. Soc.*, **163**, F401–F410 (2016).

9. J. Slack et al., *ChemElectroChem*, **5**, 1537–1542 (2018).

10. J. J. Slack et al., *J. Electrochem. Soc.*, **166**, F3202–F3209 (2019).

11. J. J. Slack et al., *J. Electrochem. Soc.*, **167**, 054517 (2020).

12. Y.-C. Park, K. Kakinuma, H. Uchida, and M. Watanabe, *J. Power Sources*, **275**, 384–391 (2015).

13. C. Lei et al., *J. Power Sources*, **196**, 6168–6176 (2011).

14. K.-H. Kim et al., *Int. J. Hydrogen Energy*, **35**, 2119–2126 (2010).

15. S. Jeon et al., *Int. J. Hydrogen Energy*, **35**, 9678–9686 (2010).

16. T. Kitahara, H. Nakajima, M. Inamoto, and M. Morishita, *J. Power Sources*, **234**, 129–138 (2013).

17. N. Inoue, M. Uchida, M. Watanabe, and H. Uchida, *Electrochem. commun.*, **16**, 100–102 (2012).

18. B. Kienitz, J. Kolde, S. Priester, C. Baczkowski, and M. Crum, *ECS Trans.*, **41**, 1521–1530 (2011).

19. Y. Liu et al., *J. Electrochem. Soc.*, **156**, B970–B980 (2009).

20. J. Choi, K. M. Lee, R. Wycisk, P. N. Pintauro, and P. T. Mather, *J. Mater. Chem.*, **20**, 6282–6290 (2010).

21. J. J. Slack, thesis, Vanderbilt University (2019).

22. K. Cooper, *Fuel Cell Mag.*, 1–3 (2009).

23. F. Barbir, *PEM Fuel Cells - Theory and Practice*, 2nd ed., p. 130–132, Elsevier, Boston, (2012).

24. T. V. Reshetenko, G. Bender, K. Bethune, and R. Rocheleau, *Electrochim. Acta*, **56**, 8700–8710 (2011).

25. Q. Zhang, R. Lin, L. Técher, and X. Cui, *Energy*, **115**, 550–560 (2016).

26. K.-H. Kim et al., *Int. J. Hydrogen Energy*, **35**, 13104–13110 (2010).

27. K. Shinozaki, H. Yamada, and Y. Morimoto, *J. Electrochem. Soc.*, **158**, B467–B475 (2011).

28. W. An, P. N. Pintauro, K. Warner, and W. Neff, *J. Am. Oil Chem. Soc.*, **76**, 215–222 (1999).

29. P. Costamagna, S. Grosso, and R. Di Felice, *J. Power Sources*, **178**, 537–546 (2008).

30. T. Mashio, K. Sato, and A. Ohma, *Electrochim. Acta*, **140**, 238–249 (2014).

CHAPTER 5 FIBER ELECTRODE MEAS FOR IMPROVED PERFORMANCE AD DURABILITY OF HYDROGEN/AIR FUEL CELLS WITH A CATHODE CATALYST LOADING OF 0.2 mg_{PT}/cm^2

5.1 Introduction

A constraint which inhibits the wide-spread commercialization of passenger FCEVs is the costly platinum catalyst which is used at both the anode and cathode. Due to the scarcity and cost, the US Department of Energy (DOE) has set a target of 0.125 mg_{Pt}/cm^2 per membrane-electrode assembly (MEA).[1] As it stands, Toyota's commercially available passenger FCEV, the Mirai, has a platinum content of 0.38 mg_{Pt}/cm^2 per MEA.[2] Heavy-duty vehicles (HDVs), however, are not under the same price constraints as passenger vehicles and these larger vehicles also need to be substantially more durable,[3] meaning higher platinum loadings may be permissible (~ 0.3 mg_{Pt}/cm^2) for HDV applications.[4]

There have been several studies which examined the effects of cathode catalyst loading on MEA performance. Typically, these studies have taken one of two approaches. The first approach is to increase catalyst loading while maintaining a constant catalyst layer thickness. This is achieved by increasing the thickness of low Pt loading electrodes (via dilution of the catalyst with carbon nanoparticles or by using catalysts with a lower metal content) while decreasing the thickness of high Pt-loaded electrodes (by using catalyst particles with a higher Pt content).[5–7] For example, Gasteiger and co-workers prepared a 0.1 mg_{Pt}/cm^2 electrode with a 20 wt.% Pt/C and a 0.4 mg_{Pt}/cm^2 electrode with a 50 wt.% Pt/C, where both electrodes were ~10 μm thick.[5] The results revealed that the higher loading MEA had a lower electrochemically active surface area (ECSA). However, this was due to the difference in metal-to-carbon ratio rather than the

difference in cathode platinum loading. The average Pt particle diameters on 20% Pt/C and 50% Pt/C catalysts were 2.8 µm and 3.2 µm, respectively. Polarization analysis in air at differential flow rates showed that at 0.65 V, the 0.4 mg_{Pt}/cm^2 cathode MEA produced 60% higher power than the 0.1 mg_{Pt}/cm^2 cathode MEA. After square wave voltage cycling accelerated stress testing (ATST), similar to the protocol for electrocatalyst durability described by the US DOE,[1] the higher loading cathode MEA retained more of its initial power, ECSA, and oxygen reduction reaction (ORR) activity, as compared to the low loading MEA. It was unclear in this study if the less severe performance decay was due to the higher catalyst loading, the larger platinum particles, or a combination of the two factors.

The second approach to examining catalyst loading was to increase both the catalyst loading and electrode thickness.[8–14] The work published by Chaparro et al. used a 20 wt.% Pt/C catalyst powder and showed that increasing cathode catalyst loading steadily increased power up to 0.17 mg_{Pt}/cm^2. At a higher loading of 0.34 mg_{Pt}/cm^2, the performance suffered due to inaccessible catalyst sites and increased electronic resistance, i.e., the electrode was too thick.[8] Similar results were reported in a study by Qi and Kaufman[9] with a 20 wt.% Pt/C catalyst, where the measured power density at 0.6 V increased from 216 mW/cm^2 at 0.022 mg_{Pt}/cm^2 to ~400 mW/cm^2 at ~0.08 mg_{Pt}/cm^2. Increases in Pt loading, up to 0.253 mg_{Pt}/cm^2 did not produce an increase in power and a further increase in loading to 0.332 mg_{Pt}/cm^2 actually caused the power density to decrease. Interestingly, a different trend was observed in electrodes prepared from a 40 wt.% Pt/C, where power increased with increasing loading, from 222 mW/cm^2 at 0.074 mg_{Pt}/cm^2 to 474 mW/cm^2 at 0.387 mg_{Pt}/cm^2. Although there were diminishing returns at the higher platinum loadings, there was no plateau or downturn in power at high loadings.

The above studies all utilized sprayed electrodes. In 2011, Pintauro and co-workers published a paper looking at the effects of cathode catalyst loading in an electrospun fiber electrode MEA. Using a 40 wt.% Pt/C and a binder of acid-form Nafion + poly(acrylic acid) (PAA), fiber cathodes with loadings of 0.1, 0.2, and 0.4 mg_{Pt}/cm^2 were prepared and the resulting MEAs produced 520, 610, and 660 mW/cm^2 at 0.6 V, respectively.[15]

In this chapter, the effects of cathode catalyst loading and thickness on the performance and durability of fiber electrode MEAs is further explored. Rather than using an acid-form Nafion/PAA binder as was done previously,[15] a Na^+-Nafion/poly(ethylene oxide) (PEO) binder was used. As discussed in Chapter 4, the use of sodium-form Nafion allows for the PEO carrier polymer to be removed in a post-electrospinning water wash. Successful removal of the carrier polymer was shown to improve beginning-of-life (BoL) performance at both 100% and 40% relative humidity.

5.2 Experimental Methods

5.2.1 Materials

50 wt.% Pt/C (TEC10F50E) catalyst was purchased from the Tanaka Kikinzoku Kogyo Group (TKK). Nafion ionomer dispersion (Liquion LQ-1115), Nafion NR211 membranes, and Sigracet 29 BC gas diffusion layers (GDLs) were purchased from Ion Power. PEO at 600 kDa, methanol, and NaCl were acquired from Sigma Aldrich. Nafion was exchanged into the sodium form by drying the purchased ionomer dispersion and soaking the powder in 2 molar NaCl solution for 3 days with mild agitation. After ion exchange, the powder was thoroughly washed with water to remove any excess salt.

5.2.2 Fiber electrode preparation

Electrospinning inks were prepared by combining Pt/C catalyst and Nafion (in the sodium form) in a 57:13:30 (wt. fraction) water:n-propanol:methanol mixture. The ink was mechanically stirred overnight. PEO solution (5 wt.% in 1:1 water:n-propanol) was added to the ink and allowed to mix for 20 minutes prior to electrospinning, where the total solids content in the ink was 12 wt.%. After sufficient mixing, the ink was loaded into a 3 ml syringe and fit with a 22-gauge stainless steel needle. Electrospinning was carried out in an in-house humidity-controlled plexiglass chamber. Using a syringe pump, ink was forced through a 22-gauge stainless-steel needle spinneret. A voltage bias was applied to the needle tip and the resulting fibers were collected on a grounded rotating drum. The electrospinning conditions were: 0.75 ml/h, 20% relative humidity (RH), 9 kV, and a 21 cm tip-to-collector distance. Dried fiber mats were 52:37:11 catalyst:Nafion:PEO by mass. In order to achieve a 0.2 mg_{Pt}/cm^2 loading, two inks were consecutively spun onto a single fiber mat.

5.2.3 MEA fabrication and imaging

Fiber mat cathodes were hot-pressed onto a Nafion 211 membrane at 140 °C for 5 minutes at pressures varying from 3-125 MPa. Higher pressures were used in an effort to reduce the thickness of high loading electrodes. The fiber anode (with a loading of 0.1 mg_{Pt}/cm^2) was then hot-pressed onto the opposing side of the membrane at 140 °C and 3 MPa for another 5 minutes. The resulting MEA was fitted with incompressible gaskets and GDLs were placed on the anode and cathode. Finally, the MEA was loaded into a Fuel Cell Technologies test block with a 5 cm^2 active area and single serpentine flow fields at both the anode and cathode. Cross-sectional scanning electron micrographs (SEMs) for freeze fractured MEA cross-sections were collected

using a Zeiss Merlin scanning electron microscope. To improve the imaging quality, the cross-sections were gold coated using a Cressington gold coater under an argon atmosphere.

5.2.4 Electrochemical analysis

Electrochemical fuel cell tests were carried out with a Scribner Inc. 850e test station. MEAs underwent a break-in procedure at 80 °C, 100% RH, and ambient pressure under H_2/air. Voltage was cycled between 0.2 V and 0.6 V (1 minute each) until the corresponding current densities stabilized (typically after 2 hours). Polarization curves were collected at 80 °C, 200 kPa_{abs}, and 40-100% RH with H_2/air or H_2/O_2 at flowrates of 125/500 sccm. Voltage was swept from 0.2 V to open circuit voltage at a step size of 0.05 V, with a 1-minute hold at each voltage. Oxygen reduction mass activity measurements were carried out at 80 °C, 150 kPa_{abs}, and 100% RH with H_2/O_2 flowrates of 100/100 sccm. ORR mass activity was corrected for fuel cross-over (measured by linear sweep voltammetry, LSV, using a Gamry Reference 3000 potentiostat) and ohmic overpotential, as determined by electrochemical impedance spectroscopy (EIS).[16] ECSA was calculated based on hydrogen adsorption cyclic voltammograms collected using a Gamry Reference 3000 at 30 °C, 100 kPa_{abs}, and 100% RH as is described by Cooper.[17]

Two different accelerated stress tests (ASTs) were carried out. The first was an electrocatalyst durability load cycling test, where voltage was cycled from 0.6 V to 0.95 V using a square wave at 3 s per voltage (6 s per cycle). The second was a carbon support durability test, where voltage was cycled between 1.0 V and 1.5 V using a triangular wave at a rate of 500 mV/s. These ASTs were carried out at 80 °C, 100 kPa_{abs}, and 100% RH with H_2(anode)/N_2(cathode)

flowrates of 125/500 sccm. During the carbon corrosion AST, the CO_2 concentration in the cathode air exhaust was measured using a sensor from CO_2 Meter (model CM-152).

5.3 Results and Discussion

5.3.1 The effect of cathode loading and hot-pressing pressure on electrode thickness

The cathode thickness after hot-pressing was determined via SEM cross-sectional analysis. Typical results are shown in Figure 5.1. The average thickness of each cathode is summarized in Table 5.1. Average thickness and the standard deviation were calculated used 9 different measurements collected along the cross section of the MEA. Comparing a 0.1 and a 0.2 mg_{Pt}/cm^2 cathode (both pressed at 3 MPa), it was determined that doubling the Pt loading also doubled the electrode thickness. Unsurprisingly, as compaction pressure increased, the cathode thickness decreased, although the relationship between pressure and thickness was non-linear (progressively higher pressures began providing smaller increases to compaction). When a 0.21 mg_{Pt}/cm^2 cathode was compacted at 125 MPa, the electrode thickness was reduced to 4.5 µm, the same thickness as a 0.1 mg_{Pt}/cm^2 cathode compacted at 3 MPa.

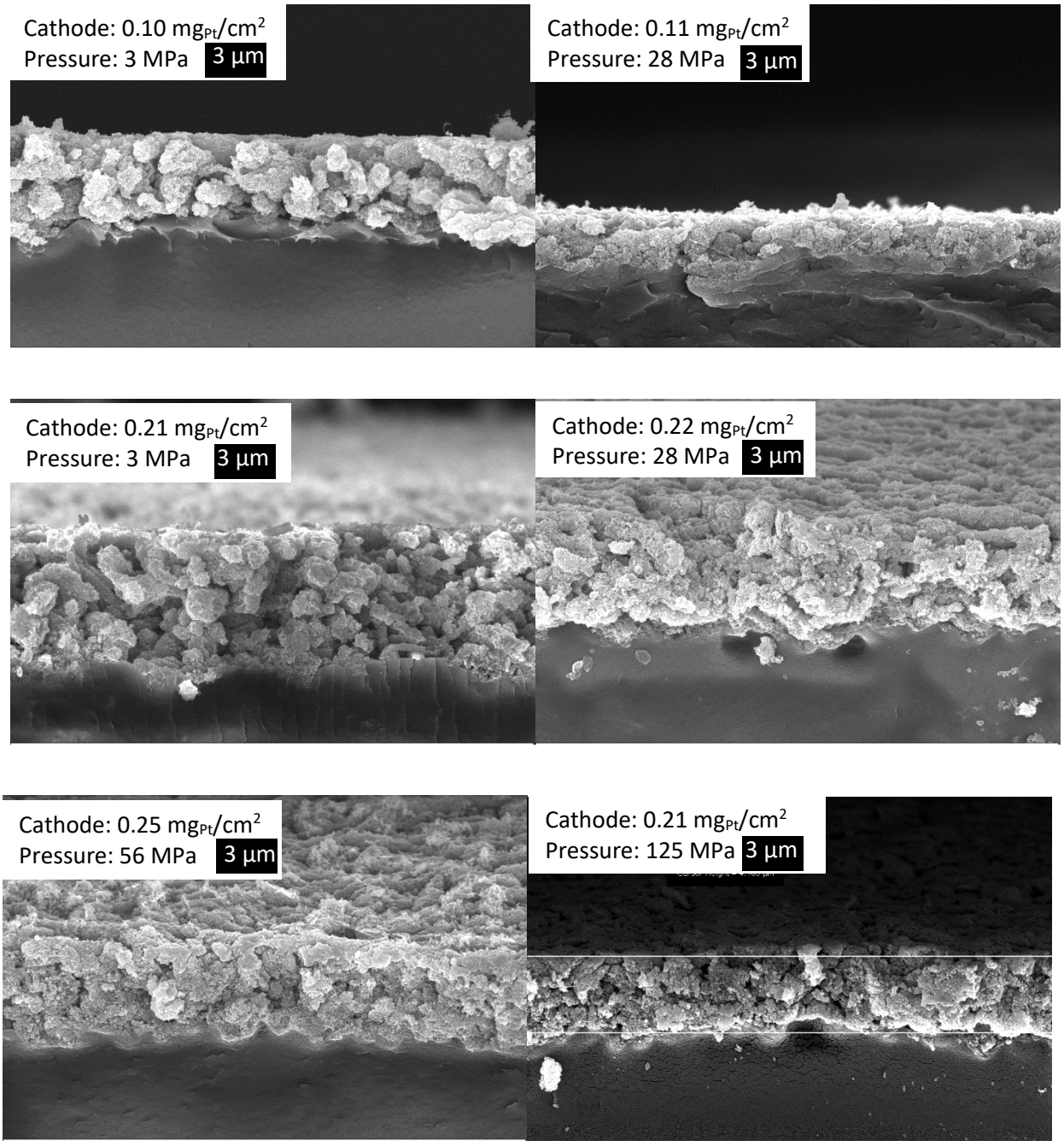

Figure 5.1: MEA cross-sectional SEMs at 10,000 times magnification for ~0.10 mg$_{Pt}$/cm^2 and ~0.22 mg$_{Pt}$/cm^2 cathode loadings after hot-pressing at 140 °C for 10 minutes at a pressure of 3-125 MPa.

Table 5.1: Cathode loading and thicknesses for MEAs hot-pressed at different pressures (10 minutes hot-pressing at 140 °C for all electrodes).

Cathode Loading (mg_{Pt}/cm^2)	Cathode Hot-Pressing Pressure at 140 °C (MPa)	Cathode Layer Thickness (μm)	Standard Deviation (± μm)
0.10	3	4.3	0.6
0.11	28	2.9	0.5
0.21	3	8.4	0.7
0.22	28	6.0	1.3
0.25	56	5.2	1.2
0.21	125	4.5	0.9

5.3.2 Effect of cathode loading and hot-pressing pressure on MEA performance

Polarization data for 0.10 mg_{Pt}/cm^2 and 0.22 mg_{Pt}/cm^2 fiber cathode MEAs, which were hot-pressed at the same pressure of 3 MPa, are plotted in Figure 5.2. The low current polarization data in Figure 5.2a show a clear improvement in power with increasing the loading. The overpotential in this region of the polarization curve is dominated by oxygen reduction kinetics which are improved at higher catalyst loading due to an increased number of available reaction sites. The Pt mass normalized ORR activity, listed in Table 5.2, is effectively the same for 0.10 mg_{Pt}/cm^2 and 0.22 mg_{Pt}/cm^2 cathode loading MEA (150 and 190 mA/mg_{Pt}, respectively).

The benefit of a higher loading cathode, seen at high voltages, diminished as the voltage decreased (current density increased). As evidenced in Figure 5.2b, at voltages below 0.75 V, the performance of the two MEAs was nearly identical. Both MEAs had a similar high frequency resistance (~50 $m\Omega \cdot cm^2$), so it can be concluded that the two MEAs performed in an identical

manner at the lower voltages, i.e., about half of the thicker electrode was inaccessible to oxygen reduction due to the high mass transport, ionic, and/or electronic resistances.[13,14,18,19]

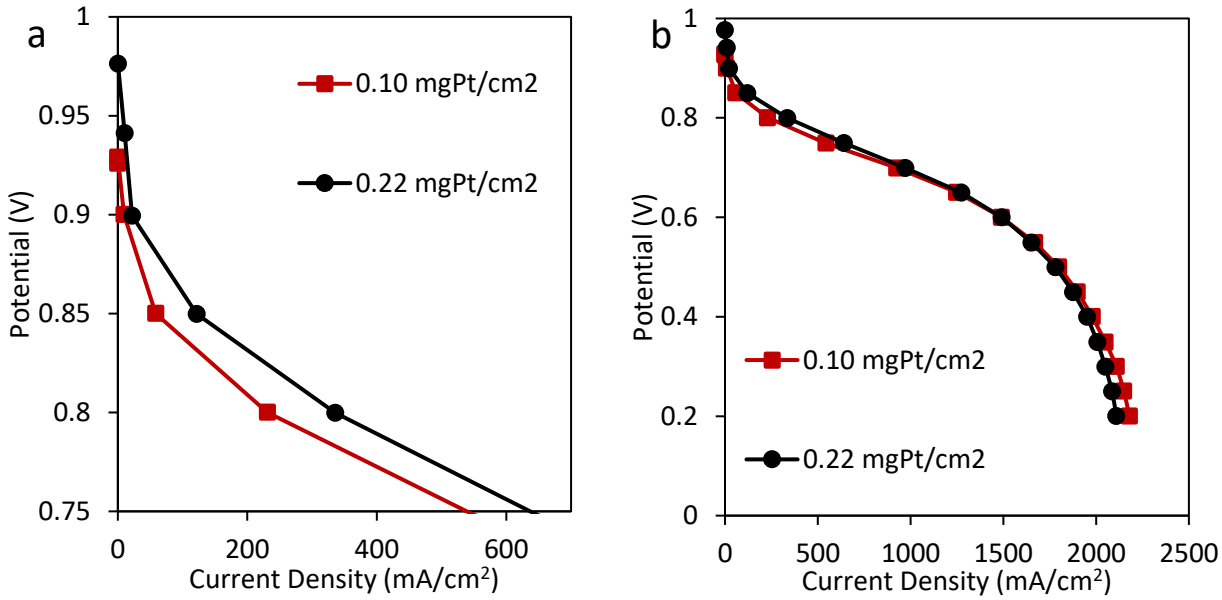

Figure 5.2: Polarization data (a) at low current and (b) from low to high current for fiber MEAs with a cathode loading of (red squares) 0.10 mg_{Pt}/cm^2 and (black circles) 0.22 mg_{Pt}/cm^2. Cathodes were hot-pressed at 3 MPa and polarization data were collected at 80 °C, 100% RH, and 200 kPa_{abs} with H_2/air flowrates of 125/500 sccm.

To verify that the anode was not limiting performance, an MEA was prepared with a 0.22 mg_{Pt}/cm^2 cathode and a 0.20 mg_{Pt}/cm^2 anode. The polarization curve for this high anode/cathode pair is contrasted with a high cathode/low anode loading MEA in Figure 5.3. The two curves are nearly identical, and it can be concluded that anode loading is not limiting. Similar results have also been reported by Gasteiger and co-workers.[12]

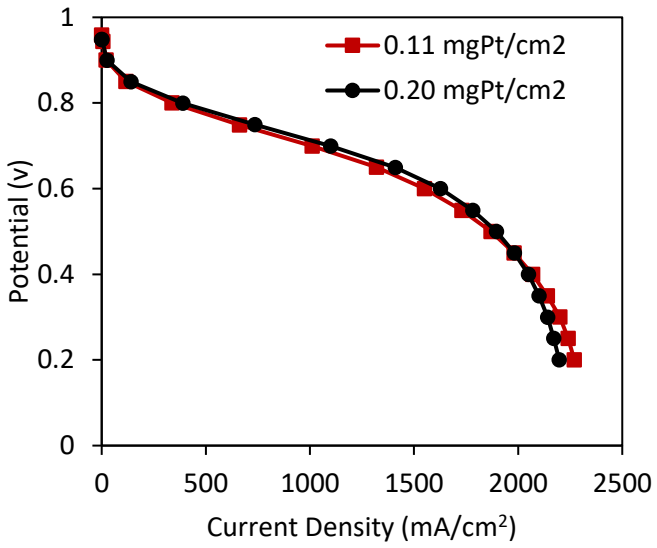

Figure 5.3: Polarization data for fiber MEAs with a cathode loading of 0.22 mg_{Pt}/cm^2 and an anode loading of (red squares) 0.11 mg_{Pt}/cm^2 and (black circles) 0.20 mg_{Pt}/cm^2. Electrodes were hot-pressed at 3 MPa and polarization data were collected at 80 °C, 100% RH, and 200 kPa_{abs} with H_2/air flowrates of 125/500 sccm.

In an effort to reduce the thickness of high loading cathodes, fiber mat electrodes were subjected to high compaction pressures during hot-pressing. As can be seen in the SEMs of Figure 5.1 and the data in Table 5.1, increasing the hot-pressing pressures significantly decreased electrode thickness. The benefit of increased compaction pressure was made obvious during fuel cells testing, as can be seen in Figure 5.4a. Pressing a 0.22 mg_{Pt}/cm^2 cathode MEA at 56 MPa led to a 20% increase in maximum power and a 15% increase in power at 0.65 V compared to a 0.22 mg_{Pt}/cm^2 cathode MEA pressed at 3 MPa. No appreciable performance difference was observed between cathodes compacted at 56 MPa and 125 MPa, despite a 15% reduction in electrode thickness. This finding is tentatively attributed to an undesirable and significant decrease in

interfiber porosity at the higher compaction pressures, which negates the benefits of a thinner electrode. Although a compaction pressure of 28 MPa improved the power generated in a 0.22 mg_{Pt}/cm^2 fiber mat cathode MEA at low voltages, such compaction had no effect on a 0.1 mg_{Pt}/cm^2 fiber cathode, as shown by the pol curves in Figure 5.4b.

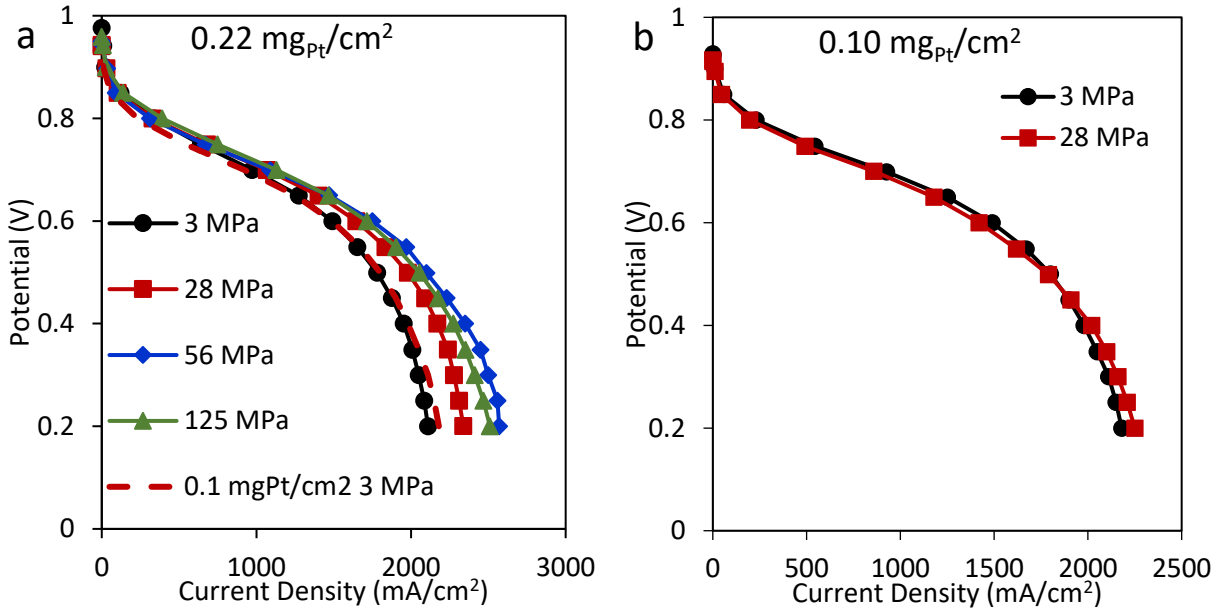

Figure 5.4: Polarization curves for fiber cathode MEAs with a cathode catalyst loading of (a) ~0.22 mg_{Pt}/cm^2 and (b) ~ 0.10 mg_{Pt}/cm^2 where the cathode was hot-pressed onto the membrane at a pressure of (black circles) 3 MPa, (red squares) 28 MPa, (blue diamonds) 56 MPa, and (green triangles) 125 MPa. The dashed red line in Figure 5.4a represents a 0.10 mg_{Pt}/cm^2 cathode MEA (pressed at 3 MPa). Data were collected at 80 °C, 100% RH, and 200 kPa_{abs} with H_2/air flowrates of 125/500 sccm.

Table 5.2: Performance summary for ~0.10 and ~0.22 mg_{Pt}/cm^2 fiber cathode MEAs

Cathode Loading mg_{Pt}/cm^2	Cathode Hot-Pressing* Pressure MPa	Power at 0.65 V mW/cm^2	Maximum Power mW/cm^2	Mass Activity mA/mg_{Pt}	ECSA m^2/g_{Pt}
0.10	3	813	917	150	88
0.11	28	767	893	151	90
0.22	3	828	908	188	72
0.22	28	911	1008	126	72
0.25	56	956	1082	165	62
0.21	125	953	1046	142	N/A

*Hot-pressing at 140 °C for 5 minutes

Although cathode compaction at high pressure substantially improved performance, it was unclear why the 50% higher power at 0.8 V was not also observed at 0.65 V. Considering that the cathode pressed at 56 MPa was 40% thinner than the cathode pressed at 3 MPa, the interfiber electrode porosity should decrease by the same amount, meaning there would be an increased risk of electrode flooding as current increased and more water was produced, and a consequential increase in mass transport overpotential. To improve understanding of the performance of high loading compacted cathode MEAs, polarization data were collected using oxygen as the cathode feed gas. More oxygen is consumed when operating at low voltages, and mass transport limitations could be due to either too low of a concentration of oxygen in the feed gas to accommodate a higher rate of consumption or oxygen being blocked from catalyst sites due to water. Operating under pure oxygen reduces the likelihood of the latter limitation, and transport limitations would instead be a consequence of flooding. Polarization data under oxygen and air were studied, and the results are plotted in Figure 5.5 where the y-axis is the ratio of power produced by a 0.23 mg_{Pt}/cm^2 cathode MEA (pressed at 56 MPa) and a 0.10 mg_{Pt}/cm^2 cathode MEA (pressed at 3 MPa). Under either air or oxygen, the effect of high cathode loading

is most prevalent at high voltage and the improved power becomes less appreciable at low potentials. When operating under oxygen, the power density ratio was 1 at 0.4 V whereas the ratio was 1.2 under air. The current at 0.4 V is much higher in oxygen (~3,500 mA/cm^2) than in air (~2,000 mA/cm^2), meaning more water is being produced and transport limitations due to flooding are exacerbated. It is under these conditions of high water production and high feed gas oxygen concentration that the highly compacted 0.23 mg_{Pt}/cm^2 cathode MEA generated less power than the 0.10 mg_{Pt}/cm^2 cathode MEA, indicating that the loss in power was due to more severe flooding in the high loading cathode MEA, most likely due to the low porosity. These trends are in good agreement with the literature, where less porous electrodes are more susceptible to flooding and mass transport limitations.[13,14,18]

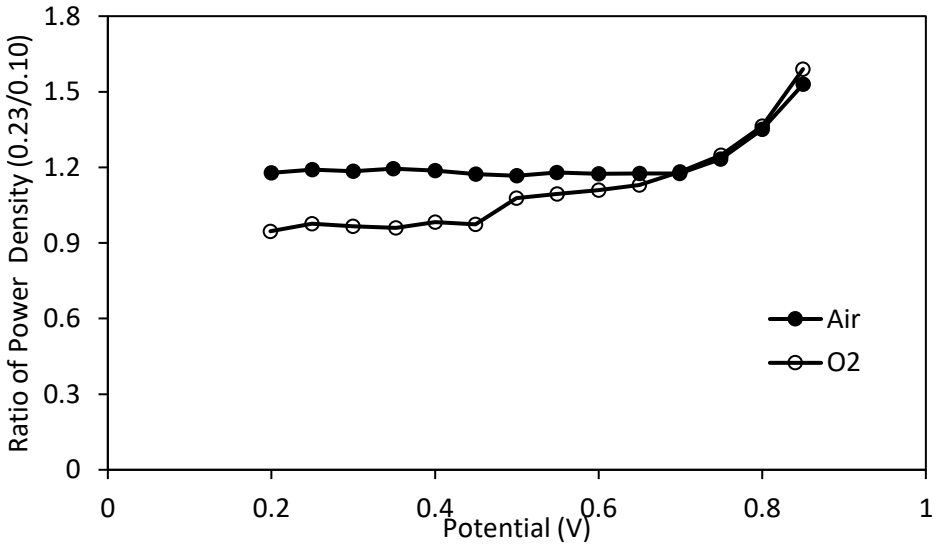

Figure 5.5: Ratio of power between a 0.23 mg_{Pt}/cm^2 cathode MEA (pressed at 56 MPa) and a 0.10 mg_{Pt}/cm^2 cathode MEA (pressed at 3 MPa) versus operating potentials under (filled) air and (open) O_2 cathode feed gas. Data were collected at 80 °C, 100% RH, and 200 kPa_{abs} with anode/cathode flowrates of 125/500 sccm.

5.3.3 Effect of cathode loading on MEA durability: Carbon corrosion

Polarization curves were collected before and after 1,000 carbon corrosion voltage cycles (1.0-1.5 V at a scan rate of 500 mV/s) and the results are given in Figure 5.6a. Figure 5.6b shows the concentration of CO_2 in the cathode effluent during two corrosion experiments. As can be seen in Figure 5.6a and summarized in Table 5.3, high and low cathode loading MEAs lost about 27% of BoL peak power after corrosion. Both MEAs experienced significant cathode thinning as can be seen in Figure 5.7. Notably, the fiber structure is partially lost in the higher cathode loading MEA, which may worsen the already poor removal of water in the highly compacted cathode. The percentage of carbon loss and the percent cathode thickness loss were also similar between the two loadings. Interestingly, the high loading cathode MEA lost no ORR catalytic activity during the AST. It is possible that after the corrosion test, catalyst which was previously unavailable for reaction became accessible to the reactants. Although relative power losses were independent of cathode catalyst loading, the EoT (end-of-test) performance was still much higher for the 0.21 mg_{Pt}/cm^2 cathode MEAs compared to the MEA with a 0.10 mg_{Pt}/cm^2 cathode. The present results are in contradiction to those published by Gazdzicki et al, who found that the ECSA loss of a 0.4 mg_{Pt}/cm^2 sprayed cathode MEA was less severe than that of a 0.15 mg_{Pt}/cm^2 cathode MEA after a similar (but not identical) triangle wave high voltage cycling AST.[10] However, the high loading cathode in that study was not compacted which may lead to different rates of corrosion. Clearly, additional experimental work with fiber mat cathode MEAs is warranted here, such as the examination of carbon corrosion durability of MEAs with a non-compacted high loading fiber cathode.

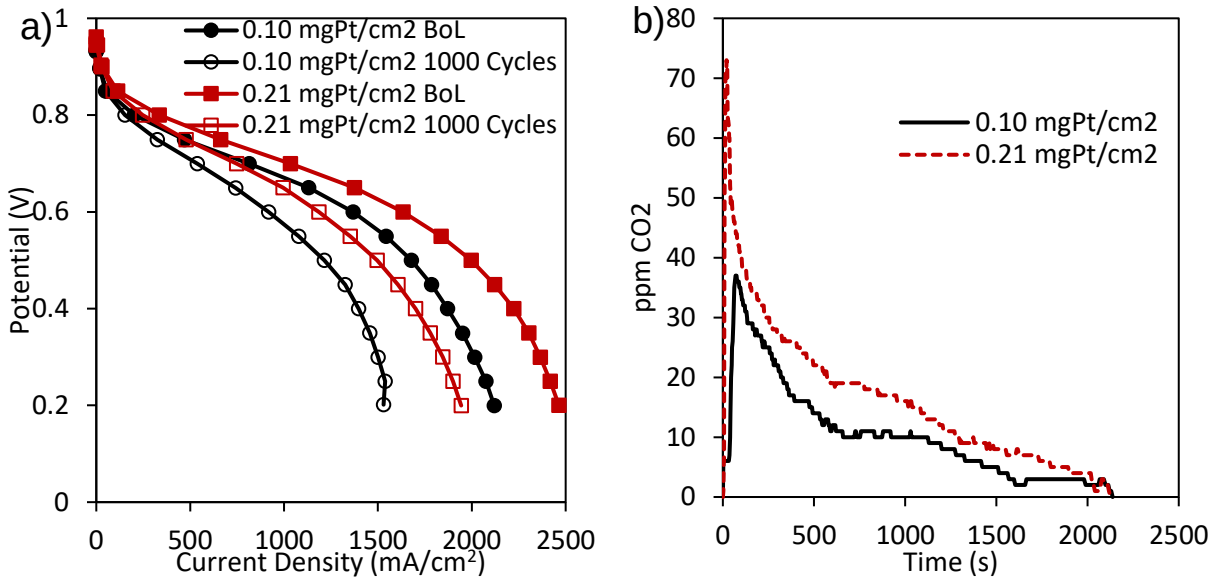

Figure 5.6: (a) Polarization curves at (filled) BoL and (open) after 1,000 carbon corrosion cycles for MEAs with a cathode catalyst loading of (black circles) 0.10 mg_{Pt}/cm^2 pressed at 3 MPa and (red squares) 0.21 mg_{Pt}/cm^2 pressed at 56 MPa. (b) Concentration of CO_2 in the cathode effluent during the carbon corrosion AST for MEAs with a cathode catalyst loading of (solid black) 0.10 mg_{Pt}/cm^2 pressed at 3 MPa and (dashed red) 0.21 mg_{Pt}/cm^2 pressed at 56 MPa. Polarization data were collected at 80 °C, 100% RH, 200 kPa_{abs}, with H_2/air flowrates of 125/500 sccm.

Table 5.3: Performance summary of 0.10 and 0.21 mg_{Pt}/cm^2 cathode loading MEAs at BoL and after 1,000 carbon corrosion cycles.

Cathode Catalyst Loading	0.10 mg_{Pt}/cm^2	0.21 mg_{Pt}/cm^2
Mass Activity (mA/cm^2) BoL/1,000 Cycles	190/109	146/146
ECSA (m^2/g_{Pt}) BoL/1,000 Cycles	60/42	70/45
Power at 0.65 V (mW/cm^2) BoL/1,000 Cycles	735/482	894/646
Maximum Power (mW/cm^2) BoL/1,000 Cycles	848/607	1009/747
Carbon Loss (wt. %)	9.3	8.5
Cathode Thickness Loss (%)	34	31

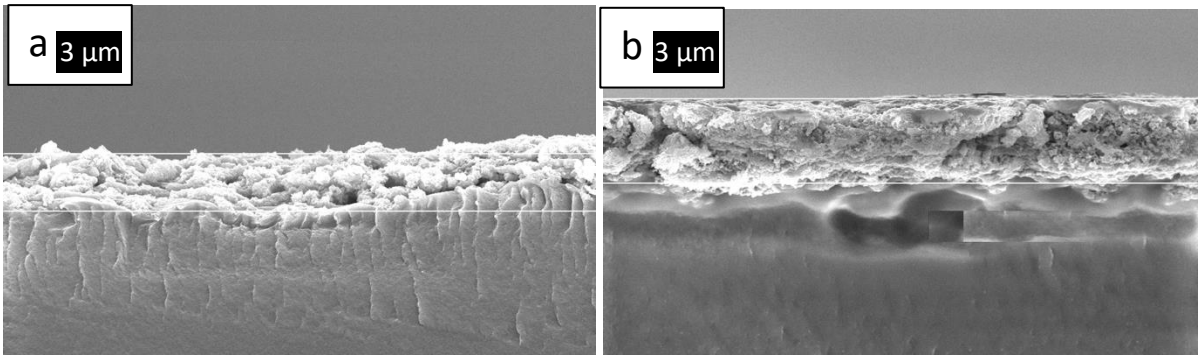

Figure 5.7: Cross-sectional SEMs at 10,000 times magnification of fiber cathodes after 1000 carbon corrosion cycles where the cathode catalyst loading was (a) 0.10 mg_{Pt}/cm^2 and (b) 0.21 mg_{Pt}/cm^2.

5.3.4 Effect of cathode loading on MEA durability: Metal dissolution

High and low cathode loading MEAs were also subjected to a metal dissolution voltage cycling AST (square wave cycling between 0.60 V and 095 V with a 3 second hold at each voltage). A 0.11 mg_{Pt}/cm^2 fiber cathode (pressed at 3 MPa) MEA was subjected to 15,000 metal dissolution cycles, and a 0.21 mg_{Pt}/cm^2 fiber cathode (pressed at 56 MPa) MEA underwent 30,000 voltage cycles. The BoL and EoT polarization curves for these tests are plotted in Figure 5.8. The results reveal that the high cathode loading MEA was much more stable, with a 26% loss in power at 0.65 V after 30,000 voltage cycles while the low cathode loading MEA lost approximately the same power after only 15,000 voltage cycles. These results of the metal dissolution AST experiments are summarized in Table 5.4. Arisetty et al. reported similar findings when comparing a 0.15 mg_{Pt}/cm^2 sprayed cathode MEA and a 0.40 mg_{Pt}/cm^2 sprayed cathode MEA , where after 30k AST voltage cycles, the lower loading cathode MEA suffered a greater loss of BoL power than the 0.40 mg_{Pt}/cm^2 MEA.[11]

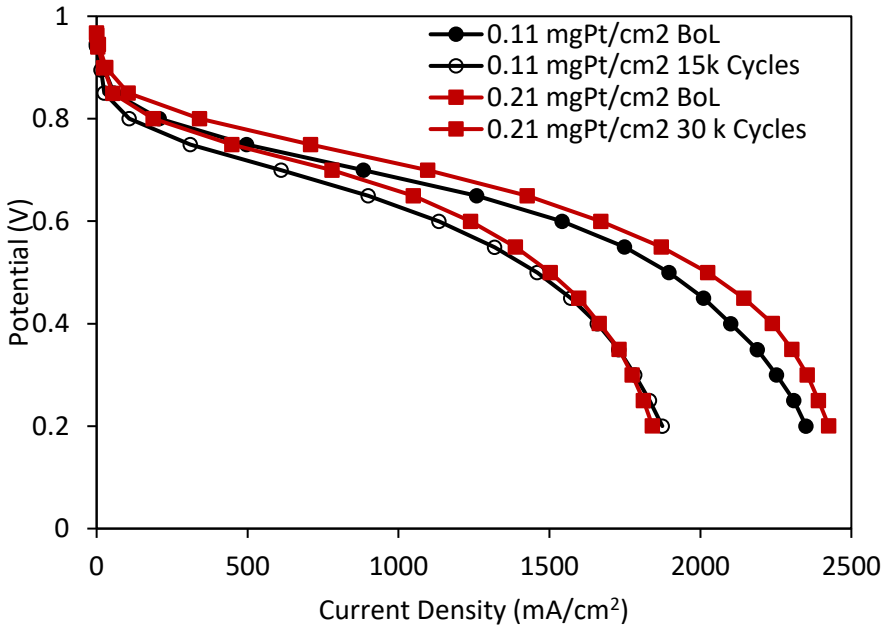

Figure 5.8: Polarization curves at BoL (filled) and after metal-dissolution AST (open) for fiber electrode MEAs with cathode loadings of (black circles) 0.11 mg_{Pt}/cm^2 and (red squares) 0.21 mg_{Pt}/cm^2.

Table 5.4: Performance summary of a 0.11 mg_{Pt}/cm^2 and 0.21 mg_{Pt}/cm^2 cathode loading MEAs at BoL and after metal dissolution cycling.

	0.11 mg_{Pt}/cm^2 15,000 Cycles	0.21 mg_{Pt}/cm^2 30,000 Cycles
Mass Activity BoL/EoT (mA/mg_{Pt})	138/129	126/111
ECSA BoL/EoT (m^2/g_{Pt})	86/35	60/34
EoT/BoL Power at 0.65 V (%)	76	74
EoT/BoL Maximum Power (%)	71	73

5.4 Conclusions

The effects of cathode loading and thickness were studied in electrospun fiber electrode MEAs with a Pt/C catalyst cathode and a binder of Na^+-form Nafion and PEO. It was found that at BoL, the performance of a ~0.2 mg_{Pt}/cm^2 cathode MEA produced double the power at high voltages as compared to a 0.1 mg_{Pt}/cm^2 cathode MEA, thus the ORR mass activity (mass normalized activity) was the same for the two electrodes. As voltage decreased and current density increased, however, the benefits of high loading became dependent upon cathode thickness (higher power at smaller thickness), where the highest power density of 1082 mW/cm^2 was achieved in a ~5 μm thick cathode with a loading of 0.25 mg_{Pt}/cm^2. The power density was 20% higher than that in a 0.1 mg_{Pt}/cm^2 cathode MEA with a cathode that was 4.3 μm thick. Compaction of a 0.1 mg_{Pt}/cm^2 cathode to 3 μm did not affect power output. Comparison of air and oxygen polarization data revealed that a ~5 μm thick 0.23 mg_{Pt}/cm^2 cathode MEA suffered greater mass transport overpotentials than a 0.1 mg_{Pt}/cm^2 cathode MEA due to lower porosity and greater susceptibility to flooding. Other factors, such as oxygen transport gas transfer resistance, may also limit the performance of the highly compacted high loading cathode MEA, and investigation of these properties is warranted. After a carbon corrosion AST, the percentage loss of carbon and the relative drop in power were comparable between a 0.21 mg_{Pt}/cm^2 cathode MEA (which was compacted to 5 μm) and a 0.10 mg_{Pt}/cm^2 cathode MEA. With regards to metal dissolution durability, the high catalyst loading cathode MEA was more robust. A 0.21 mg_{Pt}/cm^2 cathode MEA (compacted to 5 μm) lost ~25% of initial power at 0.65 V after 30,000 metal dissolution cycles, while a 0.11 mg_{Pt}/cm^2 cathode MEA lost ~25% of its initial power after only 15,000 cycles.

5.5 References

1. *Off. Energy Effic. Renew. Energy* https://www.energy.gov/eere/fuelcells/doe-technical-targets-polymer-electrolyte-membrane-fuel-cell-components.

2. R. Borup, in *Presentation to USCAR*, (2019).

3. B. Pivovar, *Nat. Catal.*, **2**, 562–565 (2019).

4. D. A. Cullen et al., *Nat. Energy*, **6**, 462–474 (2021).

5. G. S. Harzer, J. N. Schwammlein, A. M. Damjanovic, S. Ghosh, and H. A. Gasteiger, *J. Electrochem. Soc.*, **165**, F3118–F3131 (2018).

6. J. P. Owejan, J. E. Owejan, and W. Gu, *J. Electrochem. Soc.*, **160**, F824–F833 (2013).

7. T. A. Greszler, D. Caulk, and P. Sinha, *J. Electrochem. Soc.*, **159**, F831–F840 (2012).

8. A. M. Chaparro, B. Gallardo, M. A. Folgado, A. J. Martin, and L. Daza, *Catal. Today*, **143**, 237–241 (2009).

9. Z. Qi and A. Kaufman, *J. Power Sources*, **113**, 37–43 (2003).

10. P. Gazdzicki, J. Mitzel, A. M. Dreizler, M. Schulze, and K. A. Friedrich, *Fuel Cells*, **18**, 270–278 (2018).

11. S. Arisetty et al., *J. Electrochem. Soc.*, **159**, B455–B462 (2012).

12. H. A. Gasteiger, J. E. Panels, and S. G. Yan, *J. Power Sources*, **127**, 162–171 (2004).

13. M. B. Sassin, Y. Garsany, R. W. Atkinson, R. M. E. Hjelm, and K. E. Swider-Lyons, *Int. J. Hydrogen Energy*, **44**, 16944–16955 (2019).

14. J. W. Lim et al., *J. Electrochem. Soc.*, **159**, B378–B384 (2012).

15. W. Zhang and P. N. Pintauro, *ChemSusChem*, **4**, 1753–1757 (2011).

16. H. A. Gasteiger, S. S. Kocha, B. Sompalli, and F. T. Wagner, *Appl. Catal. B Environ.*, **56**, 9–35 (2005).

17. K. Cooper, *Fuel Cell Mag.*, 1–3 (2009).

18. M. Secanell, K. Karan, A. Suleman, and N. Djilali, *Electrochim. Acta*, **52**, 6318–6337 (2007).

19. G. Sasikumar, J. W. Ihm, and H. Ryu, *J. Power Sources*, **132**, 11–17 (2004).

CHAPTER 6 IMPROVED WATER MANAGEMENT OF ELECTROSPUN NANOFIBER MEMBRANE-ELECTRODE-ASSEMBLIES AT HIGH CURRENT DENSITIES MEASURED IN *OPERANDO* USING NEUTRON RADIOGRAPHY

Adapted from K. Chintam, K. Waldrop, A. M. Baker, M. J. Workman, R. Mukundan, J. M. LaManna, D. S. Hussey, D. L. Jacobson, C. Gumeci, N. Dale, J. J. Slack, R. L. Borup, and P. N. Pintauro *ECS Trans.* **2019,** 8, 125-134 with permissions from ECS.

6.1 Introduction

Hydrogen/air fuel cells have gained much attention as a replacement for the standard automotive combustion engine. Low operating temperature and zero emissions make them an attractive alternative. Presently, there are multiple fuel cell electric vehicles (FCEVs) available on the market, such as the Toyota Mirai, the Honda Clarity Fuel Cell, and the Hyundai Nexo. Water management remains a persistent challenge. A fuel cell membrane-electrode-assembly (MEA) must maintain a well-hydrated membrane and catalyst layers to promote proton conduction, but water must also be expelled rapidly from the electrode catalyst layers to allow reactant gasses to reach the catalyst, particularly at the cathode where water is generated. In order to minimize flooding in the cathode catalyst layer research has focused on the addition of hydrophobic additives, such as PTFE,[1] polydimethysiloxane,[2] and fluorinated ethylene propylene nanoparticles.[3] To manage membrane hydration/conductivity, research has focused on use of short-side-chain/low equivalent weight perfluorosulfonic acids (PFSAs)[4,5] and the incorporation of the hydrophilic silica network in the ionomer membrane matrix.[6]

Pintauro and coworkers have shown that electrospun nanofiber electrodes improve water management at high humidity, where interfiber voids allow for facile removal of product

water from the catalyst layer.[7–11] Catalyst/PFSA inks require the addition of a carrier polymer in order to form fibers. These electrodes, referred to as Generation 1, were prepared with a PFSA + poly(acrylic acid) (PAA) binder. The PAA carrier could not be removed from the final electrode. Recent advancements in fiber electrode fabrication allows for removal of the carrier polymer. These electrodes, denoted as Generation 2, exhibit excellent performance at both high and low humidity. In this work, neutron radiography is used to compare water generation in Generation 2 electrospun nanofiber-based cells prepared with either a PAA or PEO carrier. Comparisons involving a Generation 1 PAA carrier and a GDE baseline cell were also completed. Additional performance testing, such as impedance and polarization curves, is performed to connect water content observations to performance results. Water content at 100% and 40% RH at open circuit voltage (OCV) and 0.2 V is measured and compared for all cells. Comparing these results aids in better understanding the PAA and PEO methods in their similarities in differences. Joining these results with performance testing allows for further analysis and comprehension of the behavior of these high-performance electrode morphologies.

6.2 Experimental

6.2.1 Electrospun Nanofiber Electrode Preparation

Three different particle/polymer electrospinning inks were prepared in a water and alcohol mixture, Ink #1: platinum catalyst, acid-form PFSA, and poly(acrylic acid) (PAA), Ink #2: platinum catalyst, sodium form PFSA, and PAA, and Ink #3: platinum catalyst, sodium-form PFSA, and poly(ethylene oxide) (PEO). A 50 wt% platinum catalyst supported on carbon (TEC10F50E) was purchased from the Tanaka Kikinzoku Kogyo group (TKK). PFSA was purchased from Ion Power

Inc. (LIQUION™ Nafion™ LQ-1115), and PAA (450 kDa) and PEO (600 kDa) were purchased from Sigma Aldrich. After mixing, the inks were electrospun using a single needle spinneret. The electrospinning conditions and dry fiber mat compositions for each ink are listed in Table 6.1. Sufficient material was spun onto the collector to achieve a catalyst loading of 0.1 mg_{Pt}/cm^2. [Certain trade names and company products are mentioned in the text or identified in an illustration in order to adequately specify the experimental procedure and equipment used. In no case does such identification imply recommendation or endorsement by the National Institute of Standards and Technology, nor does it imply that the products are necessarily the best available for the purpose.]

Table 6.1: Electrospinning conditions and fiber mat electrode compositions

Sample	G1 PAA	G2 PAA	G2 PEO
Composition	Pt/C: H^+ Nafion: PAA	Pt/C: Na^+ Nafion: PAA	Pt/C: Na^+ Nafion: PEO
Weight Ratio	65:23:12	52:37:11	52:37:11
Tip-to-Collector Distance	8 cm	20 cm	20 cm
Relative Humidity	40%	20%	20%
Ink Flowrate	1.00 ml/h	0.75 ml/h	0.75 ml/h
Potential	10 kV	9 kV	8 kV

6.2.2 CCM Preparation

After electrospinning, fiber mat electrodes were hot-pressed onto either side of a Nafion™ NR-211 PFSA membrane (Ion Power, Inc.) to form catalyst coated membranes (CCMs). CCMs containing PEO in the electrodes were soaked in 80 °C water for 1 hour in order to remove the carrier polymer. Anodes and cathodes were symmetric for all CCMs, meaning the catalyst loading and binder composition were the same for both electrodes in a given CCM. The G1 PAA MEA was created once the GDE was added and was compared to baseline spray coated GDEs (denoted GDE), which were synthesized using identical materials and loadings, but without the PAA binder.

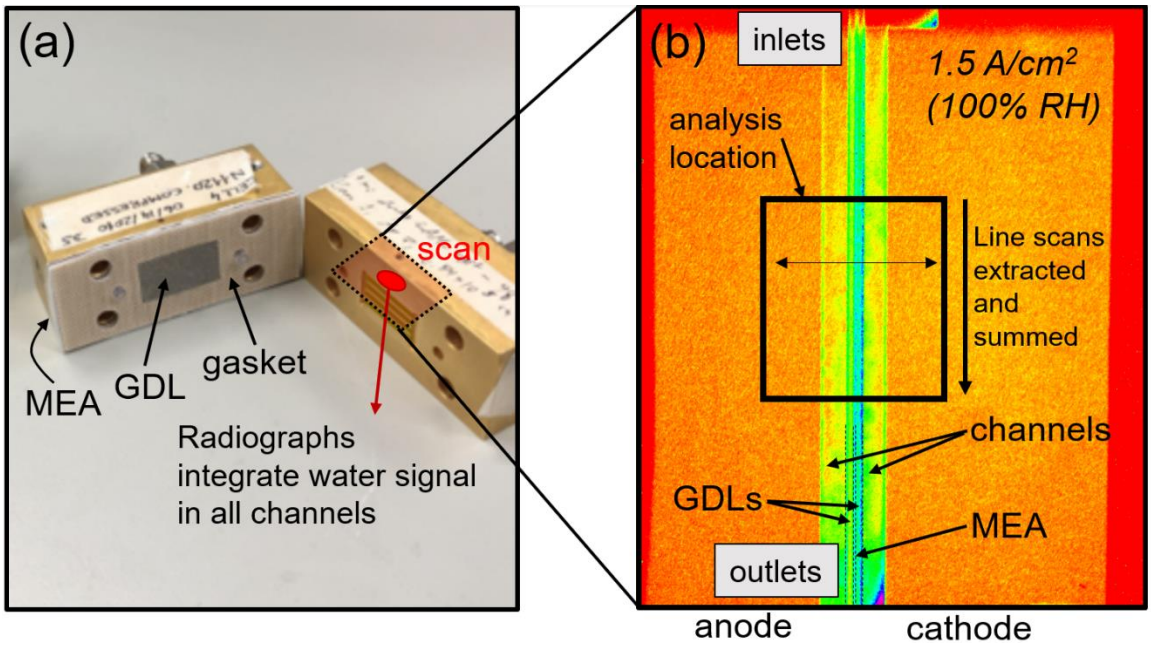

Figure 6.1: (a) Fuel cell hardware used for operando imaging and (b) representative neutron image showing locations of features and analysis area.

6.2.3 Cell Assembly and Testing

MEAs were installed into custom-built neutron imaging hardware with an active area of 2.5 cm^2 as shown Figure 6.1a. The endplates consisted of Au-coated Al blocks which served as both the reactant flow fields and current collectors. The flow fields were a 5-channel differential design (1 mm channel width, channel depth and land width). Electrospun nanofiber MEAs were assembled in the cell hardware with carbon paper gas diffusion layers (GDLs) and polytetrafluorethylene (PTFE) gaskets on the anode/cathode sides and compressed in the hardware using 4 bolts at 40 in-lb. torque. Spray-coated GDEs were directly installed in the cell, without hot pressing. The GDEs used were Sigracet 29 BC with a thickness of 235 µm. For the G1 and GDE cells, two 178 µm PTFE gaskets were used, while for the G2 cells, a 178 µm gaskets were used on the anode

and 203 µm gaskets were used on the cathode. Compression was 17% on the anode, and 24% on the cathode.

Generation 2 PAA (denoted G2 PAA) and Generation 2 PEO (denoted G2 PEO) cells will be compared throughout the text, while Generation 1 PAA (denoted G1 PAA) and the GDE baseline cells will be compared. These comparisons will be made separately due to the differences in cell construction. The G1 PAA cells were made with higher compression, due to the thinner cathode-side gasket, leading to electrical shorts. To combat this problem, the G2 cells were made with less compression, solving the shorting issue, but resulting in lower performance, likely due to contract resistance. Because of this, these two methods will not be cross compared since cell construction conditions are different.

Before testing, cells were conditioned by cycling between 0.6 V and 0.2 V for one minute each for a total of two hours, or until an OCV above 0.9 V was observed. Initial polarization performance was measured at 80ºC in 100% and 40% RH H2/air using a fuel cell test stand (Fuel Cell Technologies). Impedance measurements were conducted immediately before neutron imaging with a Gamry Model 3000 potentiostat in H2 and air at 80ºC at 100% and 40% RH at 0.5 and 0.2 V, respectively.

6.2.4 Operando Neutron Imaging

6.2.4.1 Data Collection

In order to measure water concentrations at varying conditions, neutron imaging was performed in Beam Tube 2 (BT2) at the National Institute of Standards and Technology (NIST) Neutron Imaging Facility. Cells were installed in a custom-built sample holder in co-flow configuration with

cathodes on top. Cells were operated and imaged at OCV and 0.2 V. RH was either 100 or 40% RH and outlet pressures were 101 kPa_{abs}. Temperature was 80 °C for all experiments. Cells were held for 2 hours at each condition and images were collected during the last 1.5 hours.

For all experiments, images were collected every five seconds, for a total of seven seconds per image due to a two second period to write to the data file. Voltage was also observed to ensure minimal fluctuations. High resolution mode imaged the whole cell through-plane using a 15 mm diameter aperture with a fluence rate of 1.38×107 cm^{-2} s^{-1} and a Nikon 85mm f/1.8 photo lens with a PK11 extension ring that produced a spatial resolution of about 60 µm.

6.2.4.2 Data Analysis

The images were processed using a custom Microsoft Excel tool (NIFProgs) by subtracting a "dark" image, followed by dividing the wet images by the dry images and using the log transform of the transmission to calculate the water thickness (mm) in the through-thickness direction of the MEA.[12] The water thickness profiles were averaged down the direction of the channel in the center of the cell, as indicated by the "analysis location" shown in Figure 6.1b.

6.3 Results and Discussion

Figure 6.2 displays the polarization curves for the four samples. Figure 6.2a shows that the GDE baseline data exhibits a higher OCV and better performance than the G1 PAA cell at lower current densities. This is likely due to shorting that occurred because of over-compression of the cell due to use of a thinner gasket on the cathode side. At higher currents, however, the G1 PAA MEA showed higher performance than the GDE baseline, even with the apparent shorting issue. For the G2 cells, this problem was resolved by using a thicker gasket on the cathode. As shown in

Figure 6.2b, G2 PEO cells are seen to perform better than G2 PAA cells. This is consistent across both relative humidity levels and is again seen when comparing impedance curves shown in Figure 6.3.

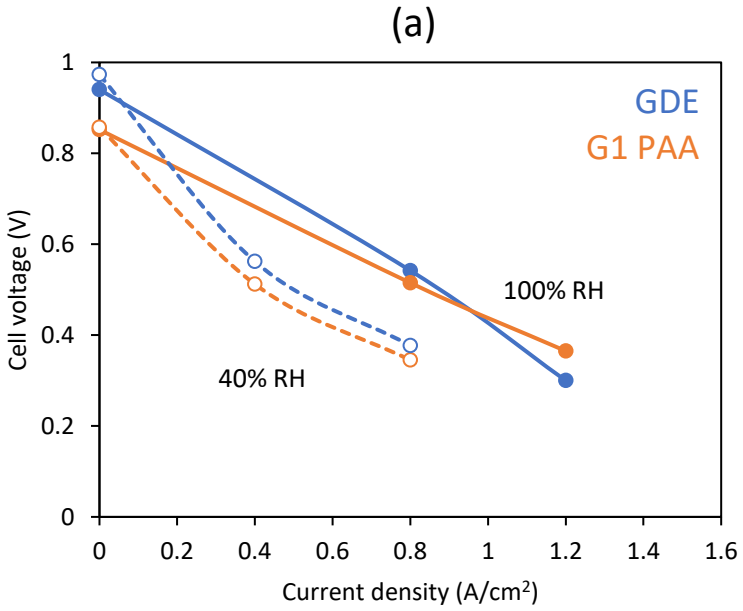

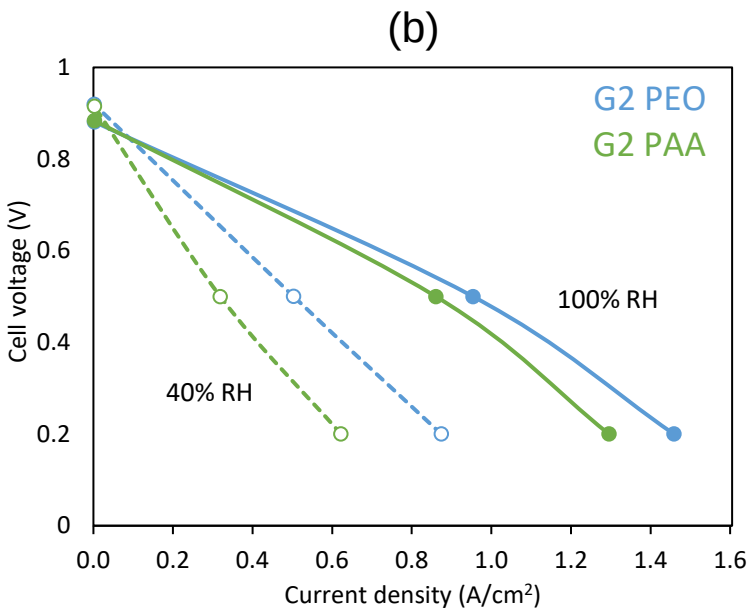

Figure 6.2: Polarization curves for (a) G1 PAA and baseline GDEs and (b) G2 PEO and PAA. Test conditions: 2.5 cm^2 operando cell hardware, 80°C, H_2/air with ambient outlet pressures. Anode/cathode flow rates in (a) were 200/200 sccm and in (b) were 500/500 sccm.

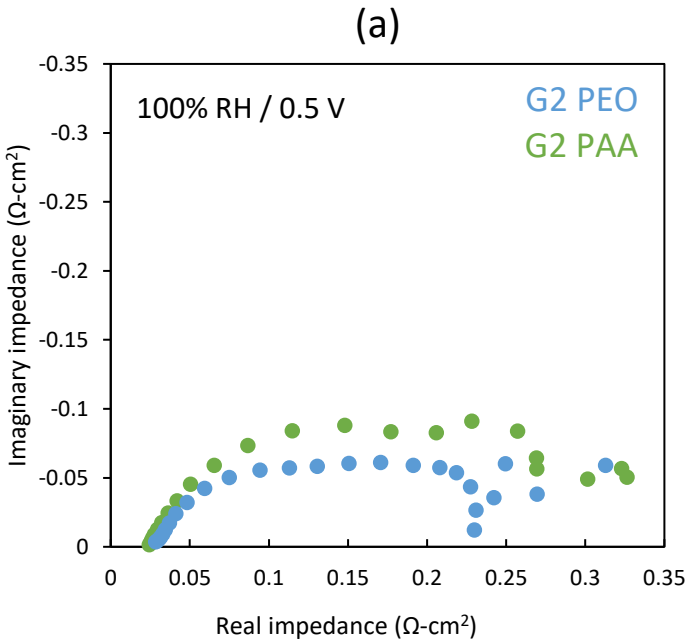

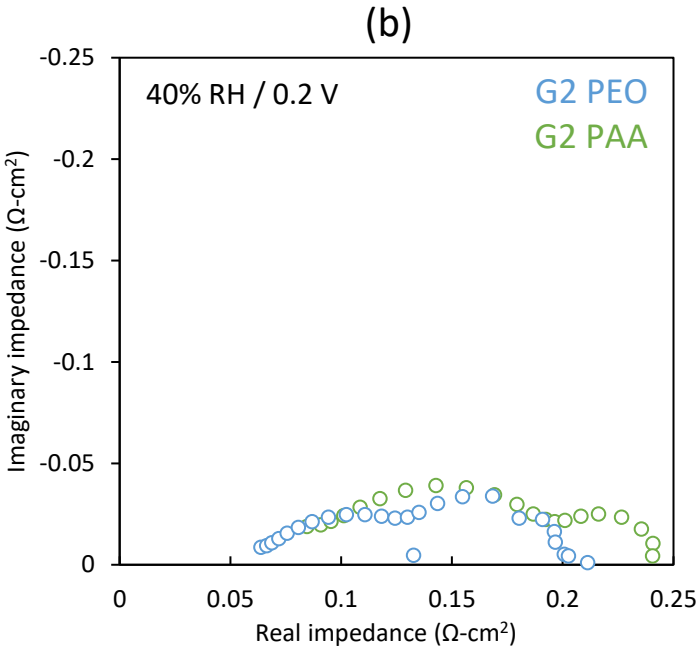

Figure 6.3: Nyquist plot for G2 PAA and G2 PEO at (a) 100% and (b) 40% RH. Note that the 40% RH data is at 0.2 V, and the 100% RH data is at 0.5 V. Test conditions: 2.5 cm^2 *operando* cell hardware, 80°C, H_2/air with flow rates of 500/500 sccm and ambient outlet pressures.

Figure 6.3 shows that the arc for the impedance of the G2 PEO cell is consistently lower than that of the G2 PEO at both 100% and 40% RH. This indicates that there are greater transport losses in the G2 PAA than the G2 PEO. This result, along with the polarization data from Figure 2, implies that the G2 PEO performs better than the G2 PAA.

Through-thickness neutron imaging water profiles for the GDE baseline and G1 PAA cells are shown in Figure 6.4. Figure 6.4a shows nearly similar water content values at OCV for both the G1 PAA and GDE cells in the MEA at 100% and 40% RH. As depicted in Figure 6.4b, however, the G1 PAA cell shows more water in the GDL compared to the baseline at 0.2 V. Here, the water concentration is around 2 times lower within the MEA and GDLs in the electrospun nanofiber-

containing MEA compared to the baseline GDE. The lower water contents suggest improved performance in the mass transport region, commensurate with the observed polarization curves in Figure 6.2a.

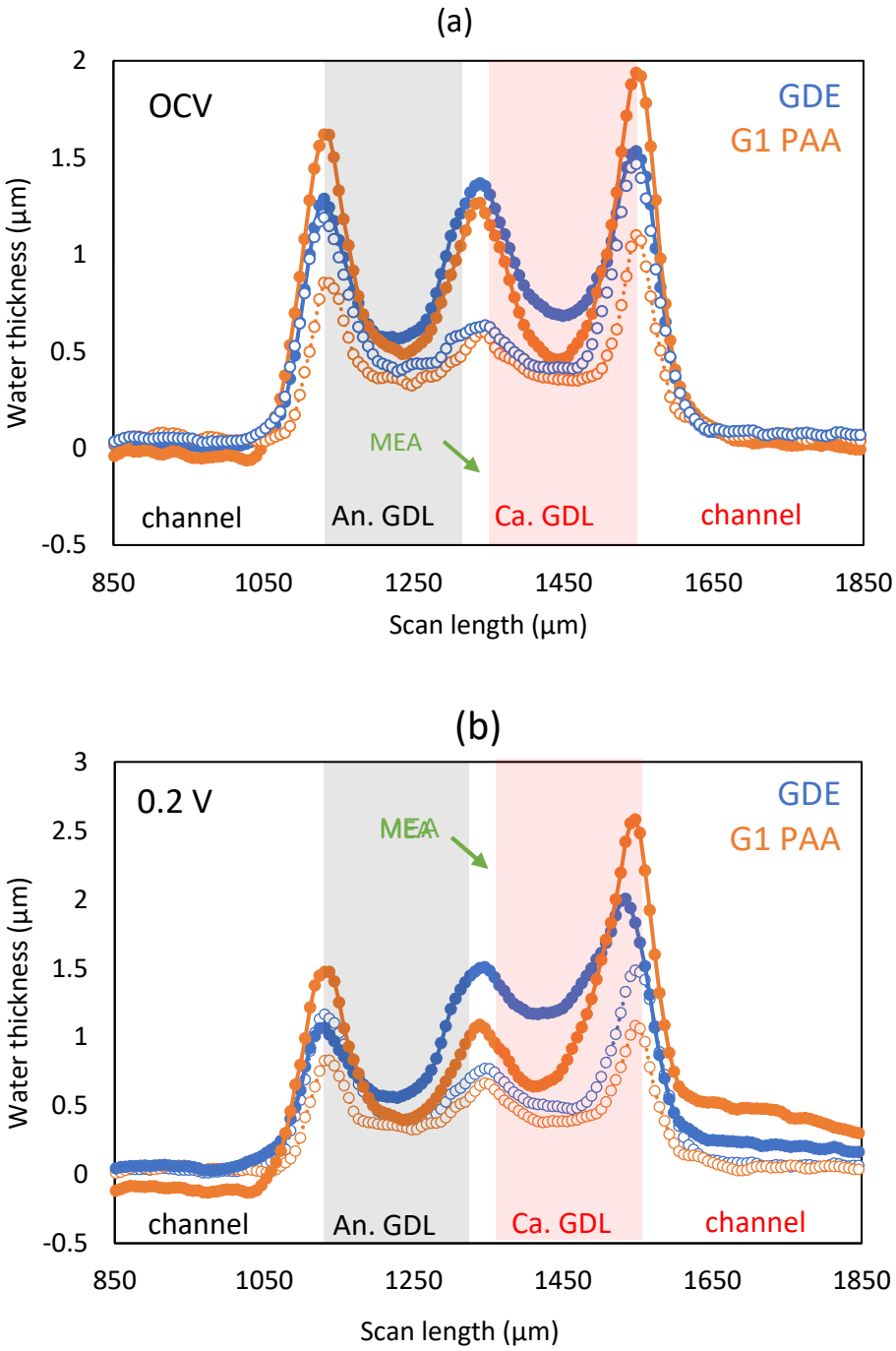

Figure 6.4: Water profiles for the G1 PAA and GDE baseline cells at 100% (closed symbols) and 40% RH (open symbols) at (a) OCV and (b) 0.2 V. Test conditions: 80°C, H_2/air at flow rates of 200/200 sccm with ambient outlet pressures.

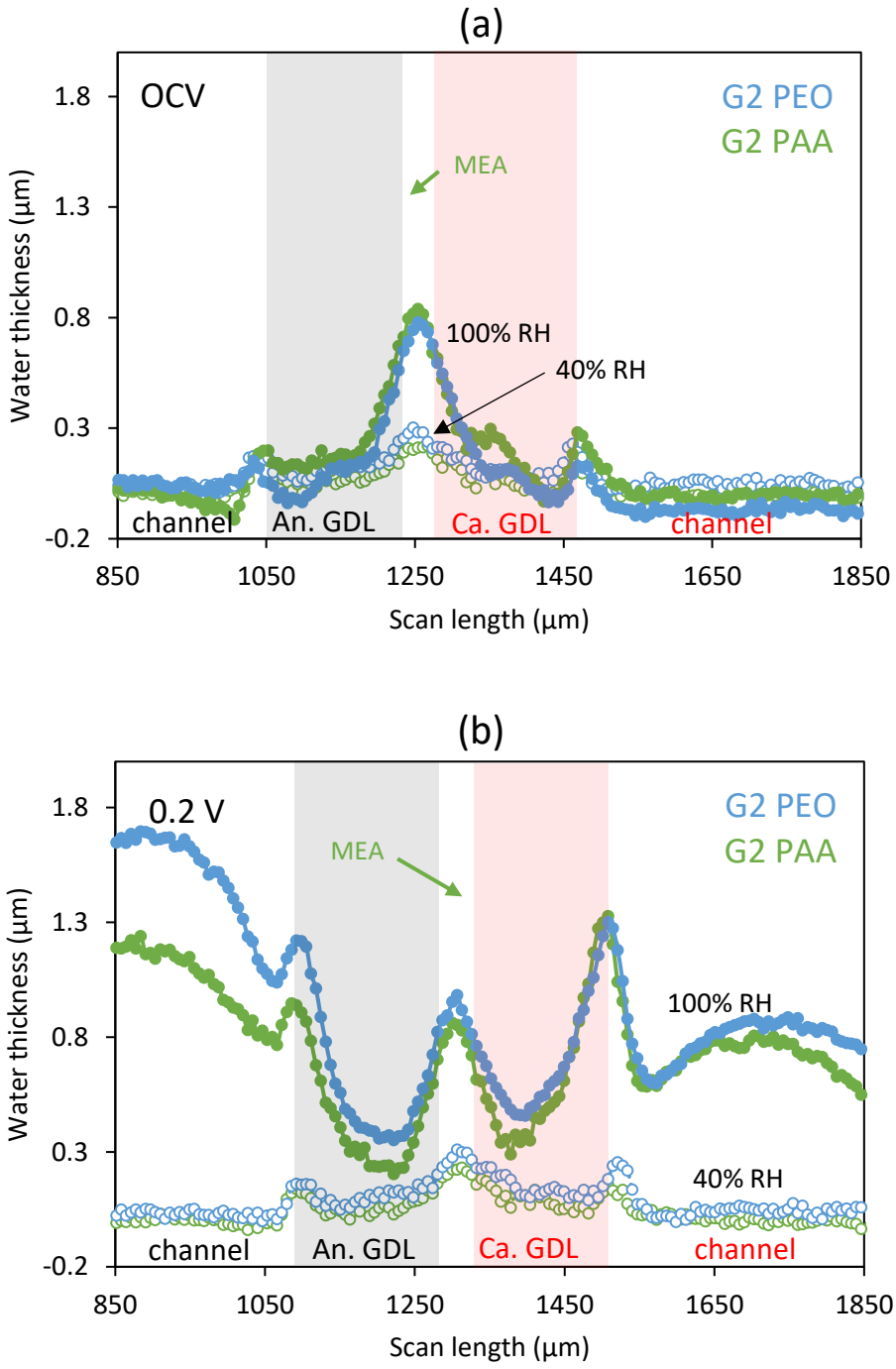

Figure 6.5: Water content profiles of G2 PAA and PEO at 100% (closed symbols) and 40% RH (open symbols) at (a) OCV and (b) 0.2 V. Test conditions: 80°C, H_2/air at flow rates of 500/500 sccm with ambient outlet pressures.

Neutron imaging data for the G2 PAA and G2 PEO is shown in Figure 6.5. These are best compared at the 100 kPa conditions at OCV and 0.2 V, at 100% and 40% RH. Figure 6.5 shows how the G2 PEO and G2 PAA compare in terms of water content. Figure 5a shows how the G2 PEO holds water more steadily at each feed gas humidity than the G2 PAA in the MEA. Essentially, the G2 PEO MEA shows a smaller water concentration variation between 40% and 100% RH, whereas the G2 PAA is higher at 100% RH and lower at 40% RH, thus exhibiting wider variation. Therefore, these observations suggest that the G2 PAA will vary in performance more with RH than the G2 PEO. Figure 6.5b illustrates how water content was similar in the MEA at 0.2 V for both the G2 PEO and G2 PAA. However, the current densities for the G2 PEO at 100% RH and 40% RH were 1.5 A/cm^2 and 0.9 A/cm^2, respectively, with those for the G2 PAA being 1.3 A/cm^2 and 0.6 A/cm^2, respectively. As shown by these numbers, the G2 PEO consistently performs better at both conditions, even with a similar amount of water in Figure 6.5b. This insinuates that the G2 PEO overall exhibits better performance and water management.

6.5 Conclusions and Future Work

Neutron radiography was used to measure the water formation through the cross sections of sprayed GDEs and electrospun nanofiber electrodes during operation. MEAs made with PAA and PEO fibers were imaged in order to determine differences in how these materials manage water. G2 PEO cells performed better in terms of polarization curves, impedance, and current density values during testing. G2 PEO and PAA cells also exhibited a similar dependence on humidity. The G1 PAA cell showed less flooding and less humidity dependence than the baseline GDE. Studying these materials under different operating conditions and future

iterations of flow-field builds will aid in better understanding this technology and, therefore, improving it.

6.6 References

1. B. Chi et al., *Electrochem. Acta*, **277**, 110–115 (2018).

2. M. Choun, D. Nauryzbayev, D. Shin, and J. Lee, *Catal. Today*, **262**, 155–160 (2016).

3. G. S. Avcioglu, B. Ficicilar, and I. Eroglu, *Int. J. Hydrogen Energy*, **42**, 496–506 (2017).

4. Y. Garsany et al., *J. Electrochem. Soc.*, **165**, F381–F391 (2018).

5. J. B. Ballengee, G. M. Haugens, S. J. Hamrock, and P. N. Pintauro, *J. Electrochem. Soc.*, **160**, F429–F435 (2013).

6. L. Dos Santos et al., *J. Memb. Sci.*, **513**, 12–19 (2016).

7. W. Zhang and P. N. Pintauro, *ChemSusChem*, **4**, 1753–1757 (2011).

8. M. Brodt, R. Wycisk, and P. N. Pintauro, *J. Electrochem. Soc.*, **160**, F744–F749 (2013).

9. M. Brodt et al., *J. Electrochem. Soc.*, **162**, F84–F91 (2015).

10. M. Brodt, R. Wycisk, N. Dale, and P. Pintauro, *J. Electrochem. Soc.*, **163**, F401–F410 (2016).

11. J. J. Slack et al., *J. Electrochem. Soc.*, **166**, F3202–F3209 (2019).

12. D. S. Hussey et al., *J. Appl. Phys.*, **112**, 104906 (2012).

CHAPTER 7 SUMMARY AND CONCLUSIONS

(1) Fiber electrode membrane-electrode-assemblies (MEAs) were prepared with a cathode composed of commercial PtNi/C and a binder of H^+-Nafion + polyacrylic acid (PAA) and an anode consisting of commercial Pt/C and a binder of H^+-Nafion + PAA. The cathode fiber diameter ranged from 400-800 nm, with a uniformly roughened surface.

(2) Fuel cell performance at beginning-of-life (BoL) and after a metal dissolution accelerated stress test (AST) for spray and electrospun fiber PtNi/C cathode membrane-electrode-assemblies (MEAs) was investigated. The fiber electrodes were prepared with H^+-Nafion + PAA binder, while the sprayed electrode binder consisted of only Nafion.

   a. At BoL, the fiber electrode MEA performed very well compared to the sprayed electrode MEA. For example, at 80 °C and 100% humidity under air/H_2, the fiber electrode MEA generated 840 mW/cm^2 at 0.65 V and achieved a maximum power of 990 mW/cm^2 while a sprayed electrode produced only 600 mW/cm^2 at 0.65 V and 810 mW/cm^2 at maximum. The difference in BOL power between the two electrode types is attributed to the high surface area and low oxygen transport resistance of the fiber electrode relative to the sprayed electrode.

   b. The fiber electrode MEA was less affected by metal dissolution accelerated stress testing than the sprayed electrode MEA. After 30,000 square-wave cycles between 0.60 V and 0.95 V, the fiber electrode MEA lost only 20% of power at 0.65 V, whereas the spray electrode MEA lost 30% of power.

c. The metal particles in both sprayed and fiber electrodes had a Ni content lower than the theoretical value of 28 atomic% (as defined by the manufacturer). At BoL the fiber electrode metal particles were only 13 atomic% Ni, and the sprayed electrode metal particles were 19 atomic% Ni. The Ni content of metal particles in both electrode types was practically unchanged after metal dissolution. It was assumed that the Ni loss occurred when the water/alcohol ink was prepared, where catalyst particles were in contact with Nafion ionomer (a known superacid, with a pK_a of ~ `6.[1]

(3) The effect of catalyst type on the microstructure and BoL fuel cell performance of fiber mat electrode MEAs was evaluated where the cathode catalyst was Pt/C, PtNi/C, or PtCo/C and the binder for all three cathode types was H^+-Nafion + PAA.

a. The intrafiber porosity of PtNi/C fibers was twice that of Pt/C fibers (12% vs. 6%). The frequency of small diameter pores (<0.75 nm) was significantly higher for PtNi/C fibers as compared to Pt/C fibers. The PtNi/C cathode MEA had higher mass activity (266 mA/mg_{Pt}) and power at 0.65 V (790 mW/cm^2) than the Pt/C cathode MEA (160 mA/mg_{Pt} and 530 mW/cm^2).

b. PtNi/C and PtCo/C exhibited a similar BoL polarization behavior at 100% humidity but differed significantly at lower humidity. For example, at 40% humidity, a PtNi/C fiber cathode MEA generated a maximum power of 760 mW/cm^2 (compared to a maximum power of 880 mW/cm^2 at 100% humidity) while a PtCo/C fiber cathode MEA as the same conditions produced only 510 mW/cm^2 (compared to a maximum power of 720 mW/cm^2 at 100% humidity). Additionally,

while the PtCo/C fiber MEA worked best at 80% humidity (a maximum power density of 790 mW/cm^2), no such reduced humidity condition was observed with the PtNi/C fiber MEA (i.e., the best MEA performance was at 100% RH). The trend of power density vs. humidity for the PtNi/C fiber MEA more closely resembles that of a fiber electrode prepared with a Na^+-Nafion + polyethylene oxide (PEO) binder.

c. Based on the above results, it is concluded that during ink preparation, Ni dissolves from the PtNi/C catalyst and the resulting Ni^{2+} cation exchange with H+, creating an ink with PAA and salt-form Nafion. Thus, the performance of fibers with this ink closely resembles that with an ink composed of Na^+-form Nafion and PEO.

(4) Fiber electrodes were successful electrospun with a polyethylene oxide (PEO) carrier polymer using Nafion in the sodium counterion form.

(5) The effect of preparing electrodes using sodium form Nafion was evaluated by electrospinning fiber mat electrodes with binders of PAA + H^+-Nafion, PAA + Na^+-Nafion, and PEO + Na^+-Nafion.

a. Electrodes prepared with sodium-form Nafion had a higher intrafiber porosity, ~16%, compared to the electrode prepared with acid-form Nafion (~6%). This was attributed to removal of carrier polymer in the sodium-form Nafion electrodes. Removal of PEO was confirmed via NMR analysis.

b. MEAs containing Na^+-Nafion-based fiber cathodes produced higher power than the H^+-Nafion-based fiber cathode MEA when operating at 100% RH. For example, an MEA where both the anode and cathode were spun from a Pt/C: Na^+-Nafion:

PEO ink produced a maximum power of ~910 mW/cm^2 at 100% RH and 200 kPa$_{abs}$, whereas an MEA with fiber anode and cathode spun from a Pt/C:H$^+$-Nafion: PAA ink produced a peak power of ~790 mW/cm^2 at the same operating conditions.

c. Electrodes prepared from Na$^+$-form Nafion-based inks were less susceptible to dehydration at low humidity feed gas conditions, as compared to fiber mat electrodes prepared with H$^+$-Nafion-based inks. At 40% RH and 200 kPa$_{abs}$, the MEA prepared with electrodes spun from Na$^+$-Nafion + PEO produced a maximum power of 830 mW/cm^2, whereas the MEA prepared with electrodes spun from H$^+$-Nafion + PAA only generated a peak power density of 530 mW/cm^2. The improved performance at low humidity is attributed to a higher number of small intrafiber pores which may facilitate capillary condensation and prevent ionomer drying.

d. A simple capillary condensation model was used to verify that the pores in Na$^+$-Nafion + PEO fibers (post water soak) are sufficiently small for the condensation of water at 40% relative humidity and 200 kPa$_{abs}$ while those in an acid-form Nafion + PAA binder are not small enough for condensation at low feed gas humidity.

(6) The effect of binder type and Nafion counter-ion was investigated in painted slurry electrode MEAs where the binders were neat acid-form Nafion, of PAA + H$^+$-Nafion, PAA + Na$^+$-Nafion, and PEO + Na$^+$-Nafion.

a. MEAs with electrodes prepared from neat H$^+$-Nafion, PAA + Na$^+$-Nafion, and PEO + Na$^+$-Nafion inks all gave similar performance at 80 °C, 100% RH and 200 kPa$_{abs}$. The H$^+$-Nafion + PAA electrode MEA produced 20% less power at 0.65 V than the

other slurry electrode MEAs, due to the presence of PAA, which is strongly bound to Nafion (it cannot be remove from fibers by water soaking) and dilutes the proton conducting Nafion.

b. All tested slurry electrode MEAs produced significantly lower power when operating at 40% RH, indicating that the high power at low humidity observed in fiber electrode MEAs prepared with Na^+-Nafion is dependent on fiber morphology.

(7) Fiber electrode MEAs with a cathode loading of ~ 0.2 mg_{Pt}/cm^2 were prepared and the BoL performance of these high catalyst loading MEAs was compared to that of MEAs with 0.1 mg_{Pt}/cm^2 cathode loading. These MEAs were fabricated using identical hot-pressing conditions.

a. Doubling the cathode catalyst content doubled power in the activation region of the polarization curve (at 100% RH and 200 kPa_{abs}), where the recorded power densities at 0.85 V were 100 mW/cm^2 vs. 50 mW/cm^2 for the 0.22 mg_{Pt}/cm^2 and 0.10 mg_{Pt}/cm^2 cathodes, respectively. From this data, the oxygen reduction mass activities (mass normalized activities) were nearly identical, ~190 mA/mg_{Pt} at 0.2 mg_{Pt}/cm^2 and 150 mA/mg_{Pt} at 0.1 mg_{Pt}/cm^2.

b. Polarization curves in the ohmic and mass transport regions were nearly identical for 0.22 mg_{Pt}/cm^2 and 0.10 mg_{Pt}/cm^2 cathode loadings and the maximum power was the same at 920 mW/cm^2. This result indicates that there was poor catalyst utilization for the higher loading cathode at low voltage (high rates of oxygen consumption). The high loading electrode had a thickness twice that of the 0.1

mg_{Pt}/cm^2 fiber mat. The added thickness created unwanted resistances to oxygen gas penetration into the electrode, water removal from the electrode, and/or an increased electrical resistance between catalyst particles in the electrode thickness direction.

(8) The effect of cathode thickness on BoL performance was investigated by different hot-pressing pressures (at a given hot-pressing temperature and time) using electrodes with a loading of either ~0.20 mg_{Pt}/cm^2 or 0.10 mg_{Pt}/cm^2.

   a. Increasing the hot-pressing pressure from 3 to 28 MPa decreased the thickness of a 0.10 mg_{Pt}/cm^2 from 4.3 µm to 2.9 µm, but there was no observable effect of cathode thickness on the resulting V-i fuel cell polarization curves.

   b. The thickness of a 0.21 mg_{Pt}/cm^2 cathode was reduced from 8.4 µm to 4.5 µm by increasing the hot-pressing pressure from 3 MPa to 125 MPa. Compaction improved the fuel cell power density, where a 0.22 mg_{Pt}/cm^2 cathode pressed at 3 MPa only produced 910 mW/cm^2 at maximum power, but a 0.25 mg_{Pt}/cm^2 cathode pressed at 56 MPa produced a peak power of 1082 mW/cm^2 (the variation in loading which is experimentally insignificant cannot alone explain the increase in power). For pressures > 56 MPa, there was no further change in the fuel cell polarization curve and no further decrease in cathode thickness.

(9) Fuel cell performance after metal dissolution and carbon corrosion ASTs was evaluated in fiber electrode MEAs prepared with either high or low cathode catalyst loading.

   a. After 1,000 carbon corrosion cycles, the relative losses for power, carbon, and cathode thickness were comparable for a 0.10 mg_{Pt}/cm^2 cathode MEA and a 0.21

mg_{Pt}/cm^2 cathode MEA (which was pressed at 56 MPa). Both MEAs lost ~30% of BoL power. Notably, cross-sectional MEA SEM images revealed that the fiber structure of the cathode was mostly lost during the corrosion of the high loading, highly compacted cathode MEA whereas the fiber morphology was retained in the 0.10 mg_{Pt}/cm^2 cathode MEA.

b. High cathode catalyst loading fiber mat MEAs exhibited less power loss after a metal dissolution voltage cycling AST. Thus, after 30,000 metal dissolution cycles, the MEA with a 0.21 mg_{Pt}/cm^2 fiber mat cathode MEA (pressed at 56 MPa) retained ~70% of its BoL power. A similar power loss was observed in a 0.11 mg_{Pt}/cm^2 cathode MEA, but after only 15,000 metal dissolution cycles (half as many as the 0.21 mg_{Pt}/cm^2 cathode).

(10) Neutron imaging of a fuel cell during operation at 0.2 V and 100% RH revealed that a fiber electrode MEA with an acid-form Nafion + PAA binder had an appreciably lower water content throughout the MEA cross-section than an MEA with sprayed gas diffusion electrodes and a neat H^+-Nafion binder. The improved performance of fiber electrode MEAs as compared to spray electrode MEAs is, in part, attributed to the ability of the fiber electrode MEA to rapidly expel water and minimize mass transport overpotentials.

(11) The water content in fiber electrode MEAs with Na^+-Nafion and either PEO or PAA binders was compared via neutron imaging of a fuel cell during operation. Within experimental error, both MEAs had very similar water profiles. This aligns well with the

work discussed in chapter 4, where both binder types gave comparable fuel cell performance.

Reference:

1. K. D. Kreuer, M. Ise, A. Fuchs, and J. Maier, *J. Pysique IV Fr.*, **10**, 279–281 (2000).

CHAPTER 8 PROPOSED FUTURE WORK

1. PtNi/C fiber electrodes were prepared with an acid-form Nafion + PAA binder. The same catalyst should be used to prepare fiber cathodes from a Na^+-Nafion + PEO binder to determine if changing binder affects initial fuel cell power output, cathode durability, and power density at low relative humidity feed gas operating conditions.
2. It was hypothesized in Chapter 3 that nickel was leaching from the catalyst during ink preparation and undergoing an ion exchange at the acid sites of Nafion. This should be replicated by partially exchanging Nafion with Ni^{2+} ions prior to ink preparation. The partially converted Ni-form Nafion should then be spun with PtNi/C catalyst and PAA and the resulting performance and Ni content in the metal catalyst particles should be evaluated.
3. The data indicate that fiber electrodes prepared from Na^+-form Nafion + PEO binder are less durable than those prepared from H^+-Nafion + PAA binder. Different combinations of anode and cathode binder type should be investigated. A Na^+-Nafion + PEO anode should prevent drying (drying is more severe at the anode than the cathode), and an H^+-Nafion + PAA cathode should provide greater durability (as carbon corrosion and metal dissolution stress tests degrade the cathode more severely than the anode). This type of system warrants study.
4. STEM and EDX studies are needed to examine the growth and migration of Pt material during a metal dissolution voltage cycling experiment. It is known that

there is growth in Pt particles and a reduction in electrochemical surface area during an AST. The extent of particle growth, as a function of catalyst and binder type in fiber electrodes is needed.

5. Chapter 4 only evaluated the performance of Na^+-Nafion + PEO binder electrode MEAs at 80 °C. However, there is a push in the fuel cell community to operate at higher temperatures, where the vapor pressure of water is higher. This is to say, more moles of water would be needed to reach 40% RH at 90 °C than at 80°C and therefore MEAs would be more susceptible to drying. The effect of higher operating temperature on high and low humidity performance for Na^+-Nafion + PEO binder fiber electrode MEAs should be studied for Pt/C and Pt-alloy/C cathode catalysts.
6. All of the MEAs in Chapter 4 were prepared with Nafion binder (1100 equivalent weight) and a 25 µm thick Nafion membrane. Using a lower equivalent weight ionomer and a thinner membrane are both common strategies to minimize MEA drying. Employing these strategies in addition to the use of the ionomer in the sodium-form with a PEO binder may allow for high power at even lower humidity, and certainly warrants investigation. Also, different ionomer/catalyst ratios in fiber mat cathodes should be examine, to determine whether a higher or lower ionomer/carbon ratio at the anode and cathode will improve the power and/or durability of fiber mat electrode MEAs.
7. In Chapter 5, accelerated stress tests were only conducted on compacted high loading cathode MEAs. These same tests should be repeated on high loading

cathode MEAs which were not compacted to evaluate what trade-off between power and durability may be present when considering compacted and uncompacted cathodes. Also, the metal dissolution AST should be extended to 75,000 voltage cycles, which is the appropriate number to assess fiber mat electrode MEA for heavy duty vehicle applications.

8. Cathode loadings of 0.3 or 0.4 mg_{Pt}/cm^2 warrant investigation. Power output and durability should be studied for these higher cathode loading MEAs as well as the effects of cathode compaction. Specifically, it is valuable to know at what cathode catalyst loading performance plateaus and at what loading performance start to decline.

9. The effect of cathode loading should also be investigated using catalysts with different metal contents. It would be valuable to see if catalysts with different metal contents are better suited for different cathode loadings. For example, a 20 wt.% Pt/C cathode MEA may perform better than 60 wt.% Pt/C cathode MEA at a loading of 0.1 mg_{Pt}/cm^2, but the opposite may be true at 0.4 mg_{Pt}/cm^2.

10. A direct comparison between the water content during operation of fiber electrode MEAs with binders of acid-form Nafion + PAA binder and Na^+-Nafion + PEO binder must be made. Neutron scattering images should be collected for both MEAs operating at exactly the same operating conditions, especially at low operating humidity where the performance differs significantly. If the Na^+-Nafion-based MEA has a higher water content at low humidity than the H^+-

Nafion-based MEA this will provide credence to the capillary condensation theory proposed in Chapter 4 and help explain why the Na^+-Nafion electrode MEAs perform so well.

11. It is critical to gain a better understanding of the high performance observed at 40% RH for Na^+-Nafion-based fiber electrode MEAs. Particularly, the relative amount of water in the MEA at 40% RH and 100% RH must be studied at operating pressures greater than the ambient. Is the same amount of water present in the MEA at these different humidities?